



Durham E-Theses

Measurement Uncertainties in Fibre-coupled Spectrographs

LEMKE, ULRIKE

How to cite:

LEMKE, ULRIKE (2012) *Measurement Uncertainties in Fibre-coupled Spectrographs* , Durham theses, Durham University. Available at Durham E-Theses Online: <http://etheses.dur.ac.uk/3412/>

Use policy

The full-text may be used and/or reproduced, and given to third parties in any format or medium, without prior permission or charge, for personal research or study, educational, or not-for-profit purposes provided that:

- a full bibliographic reference is made to the original source
- a [link](#) is made to the metadata record in Durham E-Theses
- the full-text is not changed in any way

The full-text must not be sold in any format or medium without the formal permission of the copyright holders.

Please consult the [full Durham E-Theses policy](#) for further details.



MEASUREMENT UNCERTAINTIES IN
FIBRE-COUPLED SPECTROGRAPHS

Ulrike Lemke

A Thesis presented for the degree of

Doctor of Philosophy

Centre for Advanced Instrumentation
Department of Physics
University of Durham
England

February 27, 2012

Abstract

The signal quality of fibre-coupled spectrographs can be limited by the inherent properties of the optical fibre. This is especially the case for applications that require high signal-to-noise performance and high spectral resolution. Examples include metallicity and age of star clusters, as well as investigations of Lyman-alpha absorbers. Extra-solar planet research in particular encounters its limitations due to the non-repeatability of the fibre response.

Initially, a limited signal quality due to fibres seems counter-intuitive, since one of the most remarkable advantages of fibres is their signal stabilizing property, called *image scrambling*, which refers to the effect that the fibre output signal is largely insensitive to variations at the input side. However, the fibre photometric and barycentre response is subject to external parameters like stress, seeing and guiding variations. State-of-the-art instrumentation has attained a level of sensitivity where these effects will impact upon instrument performance, especially when advancing to a regime of spectral resolving powers where the quantized character of the standard optical fibre can be resolved, which manifests itself in *modal noise*.

Unprecedented effort will be required in order to accomplish high resolving powers in the spectral and spatial domains with 40 m class telescopes. It is therefore essential to predict these fibre-related measurement uncertainties so that the performance of current and future instruments can be optimized.

This thesis starts out with a phenomenological description of the different effects that give rise to fibre-related noise and its influence on the observables relevant to astrophysics, such as barycentre and photometric stability. Special emphasis is given to the photometric uncertainties related to modal noise, where first a theoretical model is outlined which in later chapters will be subject to experimental investigations. Subsequently, the barycentre repeatability due to incomplete scrambling is the subject of detailed investigation. The remaining sources of noise are estimated using experimental data as well as simulations and put in contrast with the other effects. Alongside the quantitative prediction of instrument instabilities, mitigation strategies will be presented and discussed. I conclude with a brief discussion of the impact of incomplete scrambling and modal noise on current instrumentation, the implications for future instrument projects as well as future work that will help to further understand and obviate the underlying mechanisms.

Declaration

The work in this thesis is based on research carried out at the Centre for Advanced Instrumentation, the Department of Physics, England. No part of this thesis has been submitted elsewhere for any other degree or qualification and it is all my own work unless referenced to the contrary in the text.

Section 7.2 discusses a scrambling prediction based on ray-tracing simulations. This investigation was conducted and the resulting figures contributed by J. Allington-Smith, and appear in this thesis in order to present a more complete picture of the incomplete scrambling phenomenon. Furthermore, section 8.3.2 presents the current state of research on a new mitigation strategy, the reversion prism. Main investigator was Graham Murray although vital contribution of the thesis author are contained as well. The results of the on-going experimental tests will presumably be subject to a forthcoming paper.

Chapter 6 has been published in Monthly Notices of the Royal Astronomical Society. This paper was produced under collaboration with Jason Corbett, Jeremy-Allington Smith and Graham Murray, however, I was lead author and primary researcher.

‘Modal noise prediction in fibre spectroscopy - I. Visibility and the coherent model’, Lemke, U. and Corbett, J. and Allington-Smith, J. and Murray, G., Monthly Notices of the Royal Astronomical Society, **417**, 689-697, (2011)

Copyright © 2011 by Ulrike Lemke.

“The copyright of this thesis rests with the author. No quotations from it should be published without the author’s prior written consent and information derived from it should be acknowledged”.

Acknowledgements

This work was undertaken with financial support of the Science and Technology Facilities Council. This thesis would not have been possible without the support of many people. I would like to express my sincere gratitude to my supervisors, Jeremy Allington-Smith and Ray Sharples, who were extremely helpful and offered invaluable advice, assistance and support throughout my studies in Durham. Special thanks also to Graham Murray whose experienced advice, supportive nature and precious friendship have been a major contributing factor.

I am much obliged to my family, who supported me during some difficult times irrespective my sometimes quirky moods and neglectful nature. Notwithstanding, they provided a base from which I could confidently move to a foreign country and undertake more than three years of study. My mother's calming influence and her tireless belief in the worthwhileness in everything I am doing were a source of constant energy. I also would like to thank my brother and his wife for being available and supportive despite the additional engagement with tending my nephews, and my nephews I would like to thank for some entertaining days during Christmas with hopefully more occasions for fooling around in future.

Last but not least, I would like to say a big 'Thank you' to all my colleagues; for all the tea-breaks, afternoon-pints, Burns-nights and mulled wines. This social environment made my stay in Durham very enjoyable and amounts it to an experience of truly English culture – at least to my now acquired understanding of English culture. In particular I would like to thank Kim Buttenschön and Mari Kolehmainen, for taking me out for lunches, trips to the countryside, pints and parties – but in particular for their friendship and support beyond academic work.

Thanks also to my friends in Germany who remained with me despite the distance and made every trip back to feel like returning to a second home.

List of Figures

1.1	Multiplexing strategies	12
2.1	The redshifted universe	17
2.2	Earth-like planet orbiting around a host star similar to our Sun	18
2.3	A relative displacement of object and slit causes the detected barycentre to shift	20
2.4	The scrambling gain is defined as the ratio between shift of the input illumination and the shift of the barycentre of the input illumination	21
2.5	Debris disk and its host star	22
2.6	Galaxies merging	23
2.7	Sunspots are zones of extreme magnetic fields that disturb the heat conduction to the surface	25
2.8	Sketch of a simple spectro-polarimeter setup (William-Wehlau Spectro-polarimeter)	25
2.9	Estimated limiting noise (due to modal noise) for different grating sizes of the FASOT spectrograph	28
3.1	Total internal reflection and numerical aperture derivation	30
3.2	Two sets of modes distinct by their path of propagation	31
3.3	Nomenclature of fibre parameters	32
3.4	Solutions for the characteristic equation	37
3.5	Typical speckle pattern of the fibre far-field	44
4.1	Modal noise originates from truncating the beam of an inhomogeneous, time-varying intensity distribution	51
4.2	Signal to noise ratio as a function of fractional detector area	53
4.3	Modal noise measurements of a 70 m fibre and exponential fit	55
4.4	Measured and predicted noise	58
4.5	The excited modes for Airy coupling	59

4.6	Comparison of experimental and theoretical data	61
4.7	Aperture clipping of fibre end-face carrying two modes	62
4.8	Normalized propagation constant versus normalized wavelength . . .	63
4.9	Oscillation periods and optical spectra	65
5.1	Irradiance pattern of two modes	67
5.2	Simulations reproducing the Chen et al. result	67
5.3	Fourier analysis of the data shown in fig. 5.2.	68
5.4	Modal noise originates from truncating the beam of an inhomogeneous, time-varying intensity distribution	71
5.5	Simulated modal pattern upon which fig. 5.6 is based.	71
5.6	Throughput variation for the few mode case.	71
5.7	The <i>SNR</i> for different slit-widths.	73
5.8	Depending on the number of wavelengths sampled, the <i>SNR</i> can take on different values.	73
5.9	Occurrence of throughput intensity	75
5.10	Same as fig. 5.9, but 200 data points and 80um slit, 60 modes. . . .	76
6.1	Fibre input and Fibre agitation scheme	82
6.2	Schematic depiction of the Echelle spectrograph used for experimental investigations	83
6.3	Fibre input and slit-unit	83
6.4	The spectrograph test-bench used for experimental investigations . .	84
6.5	Fibre far-field re-imaged at the CCD and fibre truncation	84
6.6	Intensity pattern of raw data	85
6.7	Count rates for HeNe-laser illumination and corresponding Gaussian fit	90
6.8	Sodium doublet detection to derive spectral dispersion	90
6.9	Focal ratio degradation	91
6.10	Increased focal ratio degradation due to misalignment of the fibre towards the optical axis	92
6.11	Unagitated fibre image and agitated fibre image	93
6.12	Optimum number of rows to be included for analysis.	95
6.13	The <i>SNR</i> has been derived as described in section 6.2.1 where an increasing number of rows are integrated before calculating the <i>SNR</i> according to eq. (6.13)	95
6.14	Normalized intensity distribution along dispersion direction	96
6.15	A 'flatfielded flatfield'	97

6.16 Exposure time was increased and for each dataset the modal noise calculated in order to find the point where the limiting signal-to-noise is reached	98
6.17 Absolute noise contributions for $s = 200 \mu\text{m}$, $f_1=300 \text{ mm}$, $F = 3.9$, first measurement.	99
6.18 Absolute noise contributions for $s = 200 \mu\text{m}$, $f_1=300 \text{ mm}$, $F = 3.9$, second measurement.	99
6.19 Simulation of unagitated fibre noise.	100
6.20 Input vectors that lead to the graphs in figs. 6.17 and 6.19 after applying the standard deviation.	101
6.21 Unagitated fibre images are flat-fielded yielding a modal pattern . .	102
6.22 Signal to noise and visibility vs slit sizes s	102
6.23 Signal to noise and visibility vs input focal ratio θ_{in}	103
6.24 Signal-to-noise times visibility vs. ρ^2	104
6.25 Number of guided modes vs. θ_{in}	105
6.26 Visibility values for different input focal ratios	107
6.27 Visibility values for different slit widths, compared for two different resolving powers	108
7.1 The scrambling gain is defined as the ratio between shift of the input illumination and the shift of the barycentre of the resulting intensity pattern at the fibre output	112
7.2 Fibre core image at the fibre input	114
7.3 Spectrum obtained for scrambling investigations	114
7.4 Change in cross-section for central illumination, and for horizontal- and vertical- shift.	115
7.5 Ray tracing for different input angles	117
7.6 Exposure for scrambling tests, central illumination	119
7.7 Repeated measurement for central illumination; Cross sections for different input illumination when shifting the input spot vertically; and Cross sections for shifting the input illumination horizontally. .	120
7.8 Cross-section of fig. 7.6	121
7.9 The inhomogeneous intensity distribution at the fibre exit causes the barycentre to be different from the geometrical centre	122
7.10 Barycentre shift vs. wavelength for different number of modes coupling into the fibre.	124
7.11 Schematic representation to calculate an estimate for the barycentre shift	126
7.12 Distribution of intensities	126

7.13	Honeycomb field division	127
8.1	Fibre image after slicing	130
8.2	Image slicing device for the PEPSI-VLT instrument	130
8.3	Fibre agitation device using a commercial loud-speaker and the resulting speckle pattern	131
8.4	Improving signal-to-noise agitation with fibre agitation	132
8.5	Light entering the prism at the left experiences reflection three times. The angular and spatial information is thus reverted	134
8.6	Experimental setup for reversion prism tests.	135
8.7	Optical scrambler by Avila & Singh	136
8.8	Fibre cross-section for square and octagonal fibre	136
8.9	Modal noise for circular and square fibre	137
9.1	Modal noise and signal improvement through agitation.	140

List of Tables

2.1	Design parameters for the FASOT spectrograph	27
3.1	Mode fields and indices	37
3.2	Electric fields and intensities for the first binding modes of a step index fibre	39
5.1	Input parameters for two-mode simulation.	69
5.2	Input parameters for few-mode simulation.	70
6.1	Grating specifications and setup dimensions	86
6.2	Slit width, Resolving power and pixel per resolution element for the two different spectrograph setups.	89
7.1	Barycentre shift at the fibre exit far-field in pixel and fibre core width	114

Contents

Declaration	3
List of Figures	4
List of Tables	5
I Introduction and Background	10
1 Fibre spectroscopy	11
2 The astrophysical context	14
2.1 What can we learn from astrophysical spectra?	15
2.2 Barycentre repeatability and radial velocity measurements	16
2.3 Spectrophotometric uncertainties	22
2.4 Modal noise in polarimetric measurements	24
3 Fibre properties	29
3.1 Ray optical model	29
3.2 Mode model	32
3.2.1 The coherent electromagnetic field	32
3.2.2 The scalar wave equation	33
3.2.3 Solving the scalar wave equation	34
3.2.4 The characteristic equation	36
3.2.5 Propagation constants	38
3.2.6 Propagation constant in multimode fibres	41

3.3	The Coupling Integral	42
3.4	Speckle formation	44
3.4.1	Open and closed speckle regime, microbending	45
3.5	Focal ratio degradation	45
3.6	Summary	46
II Investigations on measurement uncertainties		47
4	A critical assessment of the current state of research on modal noise	48
4.1	Overview	49
4.2	Modal statistic approaches	50
4.2.1	Daino et al.: Square root law	51
4.2.2	Goodman and Rawson: Constrained Speckle	52
4.2.3	Baudrand and Walker: Modal noise as a function of wavelength	54
4.3	Coherence investigations	56
4.3.1	Rawson et al.: Bandwidth	56
4.3.2	Kanada and Aoyama: Modal noise for partially incoherent light	56
4.3.3	Grupp: Vignetting due to overfilled grating	57
4.3.4	Corbett: Mode excitation in optical fibres	58
4.3.5	Chen et al.: The two-mode simulation	60
4.4	Conclusions	65
5	Modal noise theory revised	66
5.1	Verification of the the two-mode case	66
5.2	Expansion to the few-mode case	70
5.3	Visibility estimation	77
5.4	Conclusions	80
6	Experimental investigations on modal noise	81
6.1	Details of the experimental setup	81
6.1.1	Spectral resolving power	87
6.1.2	Focal Ratio Degradation	91
6.1.3	Influence of polarizing optical components	92
6.2	Data analysis	93
6.2.1	Modal noise determination	94

6.2.2	Exposure time	97
6.2.3	Integration range in dispersion direction	98
6.2.4	Visibility determination	101
6.3	Experimental results	102
6.3.1	Verifying the coherent model	103
6.3.2	Determining visibility dependence	106
6.4	Conclusions	108
7	Incomplete scrambling	110
7.1	Barycentre instability and scrambling gain	111
7.1.1	Scrambling gain investigations by Avila et al	111
7.1.2	Experimental Investigation	112
7.1.3	Conclusions	116
7.2	Ray-tracing simulation	117
7.3	Estimation of Photometric uncertainties	118
7.3.1	Experimental investigation	118
7.3.2	Discussion	122
7.4	Barycentre repeatability due to modal noise	122
7.4.1	Simulation of the barycentre shift	123
7.4.2	Barycentre shift prediction	125
7.4.3	Conclusions	127
8	Devices inducing measurement uncertainties and mitigation strategies	128
8.1	Spatial and mode filtering processes	128
8.2	Fibre image slicing	129
8.3	Mitigation strategies	131
8.3.1	Fibre agitation	131
8.3.2	Reversion prism	133
8.3.3	Optical scrambling	135
8.3.4	Square and octagonal fibres	135
8.4	Conclusions	137
9	Concluding remarks	139
9.1	Introduction	139
9.2	Summary	139
9.3	Original Contributions	141

9.4	Outlook and future work	143
9.4.1	On-going instrument projects	143
9.4.2	Study on photometric uncertainties	144
9.4.3	Study on incomplete scrambling	145
9.4.4	Mitigation strategies and further considerations	146

Part I

Introduction and Background

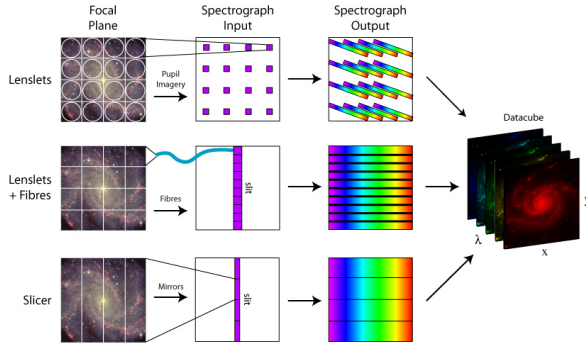
Chapter 1

Fibre spectroscopy

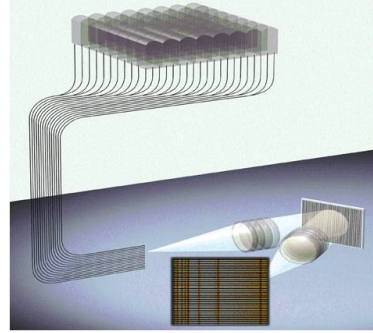
In Astrophysical observations, fibre technology mostly comes into play when either multiplex strategies are pursued or if extraordinarily stable conditions for the analyzing spectrograph are needed. Fibres have first been used in 1979 at Steward observatory Hill et al. (1980).

Multiplex instruments divide the field of view (FOV) into multiple spatial elements, allowing for simultaneous recording of several sources on the sky. There are two instrumental methods: A distributed set of objects or regions can be point-sampled using so called Multi-Object Spectroscopy (MOS). Alternatively, an extended, two dimensional region can be contiguously addressed with a technique called Integral Field Spectroscopy (IFS). In comparison to traditional scanning techniques, IFS usually delivers more reliable data, especially for extended objects. Both methods, IFS and MOS, make use of the whole photon collecting power of the telescope for several points on the sky rather than applying spectroscopy on single points consecutively, thus increasing the efficiency of telescope and detector. Additionally, highly efficient use of the detector is made. Re-positioning the sources to form a pseudo-slit at the spectrograph (as depicted in fig. 1.1) allows the spectra to be arranged in a regular pattern independent on the spatial distribution of the original on the sky. Thus, the use of the detector area can be maximised, giving highly efficient data acquisition rates.

The freedom of placing the instrument off the telescope focal plane allows for a very stable environment of the spectrograph. The camera can be held in cryogenic conditions without disturbing the air in the telescope dome and variable shear forces are avoided as the spectrograph can be set up in a separate gravity-invariant enclosure



(a) Schematic overview of three different multiplexing strategies (from top to bottom): Lenslets direct imaging, Lenslets and fibres, Image slicing.



(b) Principle of a multiplex spectrograph using the integral field technique.

Figure 1.1: Multiplexing strategies and an example for a particular instrument design (PMAS) realizing the IFU technique.

on e.g. an optical bench. Greater illumination stability is also provided due to the scrambling effect of the fibre, isolating the instrument from seeing and guiding variations (Allington-Smith, 2006). Unlike conventional slit-spectroscopy where these effects can cause severe shifts in line centre determination and photometric uncertainties, the fibre scrambles the input signal and maintains only little information of an inhomogeneous intensity distribution at the fibre input face. The remaining ‘memory’ of the fibre input that is retained will be henceforth referred to as *incomplete scrambling*.

When entering the medium-to-high resolving power range ($R \sim 20\,000 - 300\,000$) another effect comes into play: Modal noise. Modal noise can be understood as a consequence of coherence effects in waveguides. Generally speaking, it results from time-variant statistical phase relations between different fractions (*modes*) of the electromagnetic field. A thorough theoretical and experimental investigation is presented in chapters 4-6. Modal noise predominantly results in photometric uncertainties, and its effect could be measured to the orders of $SNR \sim 1 \times 10^2 - 2 \times 10^3$, depending on the spectrograph setup. The interference pattern resulting from the different fibre modes varies between subsequent exposures due to changes in the fibre stress caused by telescope guiding, and also drifts in temperature. As a result, spatially filtering processes like restricting apertures will cause the throughput to vary over time and wavelength, in particular between science and calibration exposures. A similar degrading effect on the photometric accuracy is also expected with regard to incomplete scrambling, but unlike modal noise this is assumed to be largely independent on wavelength (section 7.1.2). This is tolerable for most astrophysical applications, where line-shapes and ratios are investigated, but recording absolute

photon-flux over time would be problematic.

It should also be noted that the varying intensity distribution will lead to a displacement of the barycentre of the spectral line: Its consequence is expected to be of low significance for modal noise, because the effect is at least an order of magnitude lower than the barycentre shift due to incomplete scrambling. An estimation will be provided later in this thesis.

All the effects mentioned are of crucial importance to contemporary instrumentation design; Enhancements in instrument sensitivity are now hitting the limits of fibre stability and respective mitigation strategies have to be implemented in order to achieve the ever higher spectral resolving powers, signal to noise ratios and barycentre-repeatability.

Many applications will benefit from understanding, controlling and mitigating modal noise and scrambling properties of fibres, and it is not foreseeable that fibres find an adequate replacement in the near future. Thus progress in certain research areas is highly dependent on progress in our knowledge of fibre properties – ranging from investigations concerning metallicity and age of star clusters, to projects testing our understanding of the foundation of physics, for instance galaxy dynamics or investigations of the Lyman-alpha forest. The detection of Earth-like planets requires unprecedented precisions and resolving powers, fibre related measurement uncertainties will play a key role in achieving this goal.

This thesis begins by establishing the astrophysical background in chapter 2 which has motivated the subsequent research. The description of basic fibre properties in chapter 3 serves as a basis for the detailed study of fibre modal noise and incomplete scrambling presented in part II. After a review of the existing literature from which some preliminary theoretical conclusions are drawn, the effects of these two phenomena are measured and characterized. The respective experimental specifics are discussed as necessary.

Finally, the results are summarized and then assessed in order to frame them in a broader context (chapter 9). I conclude with an outlook proposing future work.

Chapter 2

The astrophysical context

In the last decades, advances in fundamental optics and astronomical spectroscopy have enabled the deployment of optical fibres in terrestrial as well as spacebound telescopes.

Using fibres for spectroscopic applications is a quite recent development and offers several advantages over the classic instrument design. As a result, fibre-coupled spectrographs are one of the most widely used type of instruments for astronomical observations.

However, despite the enhanced photon-gathering power, the new-generation 40 m-class telescopes will experience a restriction due to the fundamental limitation in the performance of the optical fibre. It is therefore necessary to predict the impact of these fibre properties on the spectrograph's performance to then establish mitigation strategies and estimate the prospect of meeting the science requirements.

In this chapter, I will make a distinction between two main qualities of these spectrograph performance parameters; (i) its photometric stability, presented in section 2.3 and; (ii) its barycentre stability (detected position of the spectral line), presented in section 2.2. As will become clear throughout the discussion, the measurement accuracy of astronomical observables can be traced back to the accuracy of either one of these parameters or derivatives of it, e.g. line-width and line-shape. Each section starts with a valuation of the most recent advances in relevant science applications and the benefits of deploying fibres in these cases, with a focus on the central figure of merit. I will discuss and quantify the fundamental limitation due to fibres as far as possible. This discussion provides a scaffolding that outlines and motivates the more detailed investigations in the following chapters of this thesis.

2.1 What can we learn from astrophysical spectra?

Spectral line analysis can reveal important properties of an astronomical object. Whether the detected line is an emission or an absorption line, its position, shape and wavelength-shift are compelling features to determine which physical processes are taking place; these processes affect atoms in particular, particles in general as well as the electromagnetic field interacting with these particles. Ultimately, prerequisite parameters like temperature, pressure, surface gravity and magnetic fields become accessible. Moreover, dynamic processes like outflows, rotation and relative motion towards the observer can be derived from the spectrum. These play an important role in probing cosmological models and present one of the fundamental tools of the nascent field of exo-planetary research, which owes its fast progress not least to the latest advancements in fibre-spectroscopy.

Optical fibres play an important role in all these fields, achieving the required instrument stability and spectral resolving power (Heacock, 1988; Allington-Smith, 2006). On the one hand, fibres feature a greater barycentre stability than a comparable slit spectrograph or conventional slitless spectrograph (section 2.2) but also allow for simultaneous spectral analysis of multiple sources on the sky (section 2.3). Furthermore, fibres allow for an instrument placement away from the telescope focal plane which relieves the instrument from shear forces due to its own weight, as well as facilitating the possibility of a flexure-free, temperature stabilized environment for essential spectrograph components which does not disturb the air within the telescope dome.

Thus, fibres are an indispensable part of high-performance spectroscopy instrumentation. The most challenging research endeavors aim for highest spectral resolution and photometric accuracy, thus demanding unprecedented instrument stabilities. This is a regime where the spectrograph performance is dependent on a multitude of factors, e.g. stability of the calibration source, the detector but also on the optical fibre (Wilken et al., 2010).

2.2 Barycentre repeatability and radial velocity measurements

The emission line λ_{em} experiences a shift $\delta\lambda$ when the emitting object is moving relatively to the observer with v_{rel} ($\beta = v_{rel}/c$):

$$\frac{\delta\lambda}{\lambda_{em}} = 1 - \sqrt{\frac{1-\beta}{1+\beta}}. \quad (2.1)$$

Or in the classic limit ($v_{rel} \ll c$) the velocity is directly proportional to the shift $\delta\lambda$:

$$v_{rel} = c \frac{\delta\lambda}{\lambda_{em}}. \quad (2.2)$$

Where one can define the barycentre by taking the mean intensity I_i of all the resolution elements that contribute to the spectral line in question:

$$\lambda_{em} = \frac{\sum I_i \lambda_i}{\sum I_i}. \quad (2.3)$$

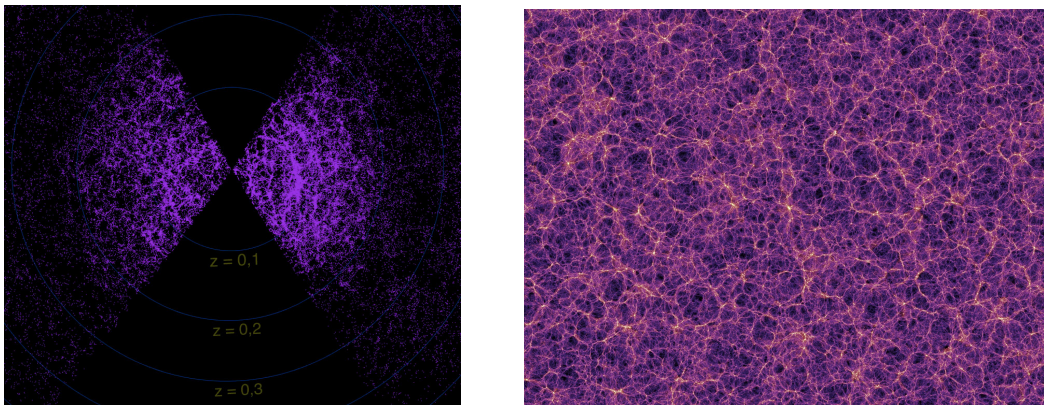
The line-centre and thus the objects relative motion towards the observer can be static. This is the case e.g. for galaxies or clusters in our local group, like the Andromeda galaxy that is moving towards us, or distant objects where the net movement relative to our local group is generally pointing away from us – An effect which has first been discovered by Hubble (1929), indicating that the universe originated in a single, cataclysmic event; the so-called ‘big bang’. The distance d to redshift $z := \Delta\lambda/\lambda$ correlation is in first order linear:

$$z = H_0 \cdot d, \quad (2.4)$$

where H_0 is the Hubble constant.

This simple relationship is a reliable distance measure in particular for very remote objects and allows for establishing a three dimensional mapping of galaxies (fig. 2.1(a)) which can then be compared with simulations of matter distributions based on cosmological models (fig. 2.1(b)).

Observations of distant supernovae by Perlmutter et al. (1998), Riess et al. (1998)



(a) Observed matter distribution (source: <http://newscenter.lbl.gov/>), SDSS.

(b) Galform simulated matter distribution, ‘Millennium simulation’ (source: <http://www.mpa-garching.mpg.de/galform/millennium/>).

Figure 2.1: The redshifted universe: The observed matter distribution is compared to simulations in order to test the validity cosmological models.

and Schmidt et al. (1998) show that the universe is expanding at an accelerated rate. This is indicative of a positive cosmological constant (Amendola & Tsujikawa, 2010) which is ascribed to a possible existence of dark energy.

The drift in redshift may be detected by studying the Ly α -forest of distant quasi-stellar objects ($z \lesssim 5$) as theoretical predictions assume a drift of $\approx 1 \text{ cm s}^{-1} \text{ yr}^{-1}$ (Liske et al., 2008) corresponding to a wavelength shift of $\delta\lambda/\lambda_{em} = 3 \times 10^{10}$. The direct measurement of this redshift drift is still pending, a value that soon might be ascertained with high-resolution spectrographs becoming available. The HARPS/ESPRESSO project is one of the candidate instruments that will be capable of meeting the requirement of measurement repeatability, guaranteeing stable enough results over time periods of $\sim 1 \text{ yr}$ – with the optical fibre being the key-enabling technology. However, the fibres pose a fundamental limit to the instrument performance due to their barycentre instability, and a set of carefully planned mitigation strategies is under study to eventually meet this ambitious science goal (Wilken et al., 2010). Other fibre missions to investigate the redshift of distant galaxies are OPTIMOS-EVE for the future E-ELT (Spanò et al., 2010) and BigBOSS at the Kitt Peak Mayall telescope (Schlegel et al., 2011). These instruments provide a static measurement of redshift distribution of nearby and distant galaxies and thus give only an indirect clue about the dynamical development of the redshift over time.

Galaxies can feature a spatially dependent line-shift as a result of matter orbiting

around the galaxy's centre of mass. According to the virial theorem, the velocity distribution is a function of the matter distribution. The predicted mass according to the virial theorem is, however, higher by a factor of five than the observed luminous matter (Dekel & Silk, 1986). These interesting findings have led to the hypothesis of dark matter and contending models such as MOND.

The perhaps most enabling technique in the study of this phenomenon are the integral field spectrographs, e.g. SINFONI at the VLT (Mengel et al., 2000), GMOS (Barbosa et al., 2006; Allington-Smith et al., 2002), the Near Infrared Spectrograph (NIRSpec) for the JWST (Clampin, 2011) and a future instrument; EAGLE for the E-ELT (Evans et al., 2010).

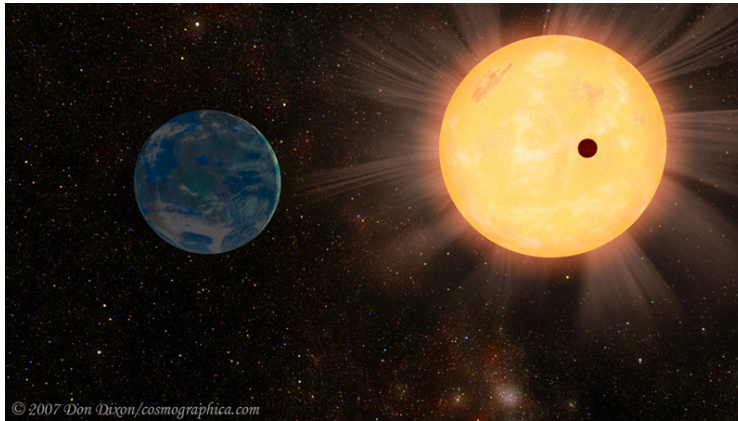


Figure 2.2: An artist impression of an Earth-like planet orbiting around a host star similar to our Sun (source: <http://newis.net/>, report on Gliese 581). Current instrumentation is on the verge of detecting these kind of systems within our galaxy using the radial velocity method, thus giving valuable insight as to how frequent Earth-like environments are.

Some astronomical objects feature periodical line-centre shifts, e.g. binary systems or planetary systems, where the periodicity of the shift allows the derivation of the mass-ratio between companions. From astrometry and transition events, the direct masses and the line of sight can be established in order to derive fundamental parameters such as the mass and size of the associated companions.

The recent achievements in sensitivity and resolving power have enabled detailed study of planetary systems. From the first discovery of an exo-planet orbiting a pulsar (Bailes et al., 1991), 20 years later state-of-the-art facilities feature the capability of detecting signals of distant Earth-sized planets orbiting host stars similar to our Sun (see fig. 2.2).

We are thus en route to solve one of the probably most fundamental questions, i.e. how unique the biological evolution is that has taken place on Earth, considering the immense scales of our host galaxy or even the entire universe. Ultimately trac-

ing development of complex life on an extra-solar planet would certainly cause a profound effect on our current relatively self-centred view of the world.

Due to the gravitational influence on the relatively bright and massive host object, planets and even complicated planetary systems can be studied. From the first exo-planet detection 20 years ago (Wolszczan & Frail, 1992), the instrumentation has evolved rapidly, and is now indicating that an arrangement similar to our solar-system is likely to exist in a large abundance (Horne, 2000). Besides instruments that employ the transiting method, e.g. COROT (Auvergne et al., 2009) and KEPLER (Basri et al., 2005); a major role is attributed to high resolution spectrographs using the radial velocity method with e.g. CODEX-ESPRESSO (Cristiani et al., 2007). With current instrumentation the line shift still needs to be relatively strong, so either the hosting star has a rather low-mass, e.g. a brown dwarf, which restricts observations to close by systems, or the planet has a mass that is at least Jupiter-like. However, ambitious estimations predict that the detection of Earth-twins orbiting around host stars similar to our Sun could become feasible in future and allow for detailed study of its atmosphere (Perryman et al., 2005; Gazzano et al., 2010). The requirements on the instrument stability remain nonetheless challenging, especially with regard to the employment of optical fibres.

In the following the relation between barycentre repeatability and the maximum precision will be presented. If the line centre measurement at λ_c has an accuracy $\Delta\lambda$, the corresponding precision Δv_{rad} in determining the radial velocity is

$$\Delta v_{rad} = c \frac{\Delta\lambda}{\lambda_c}. \quad (2.5)$$

In conventional slit spectroscopy $\Delta\lambda$ can either be seeing limited, that is when the slit is larger than the object's PSF; or $\Delta\lambda$ is limited by the width of the slit. In the first case the barycentre stability is often depending on the ability of the telescope to track the object, i.e. to keep the slit position stable relative to the object. When the object is bright enough, a narrow enough slit can be chosen in order to increase the spectral resolution, but at the expense of vignetting the beam.

Thus, usually the precision is limited by the width of one spectral resolution element $\Delta\lambda_{lim}$ which is the PSF of the instrument:

$$\Delta v_r = c \frac{\Delta\lambda_{lim}}{\lambda_c} = \frac{c}{R}. \quad (2.6)$$

Where $R = \lambda_c/\Delta\lambda_{lim}$ is the theoretical resolving power of the instrument. If, how-

ever, the instrument is limited by its pointing stability (compare fig. 2.3), $\Delta\lambda_{lim}$ in eq. (2.6) must be replaced by $\Delta\lambda_{rep}$, the indeterminacy of the repeatedly measured line-centre with the instrument at λ_c .

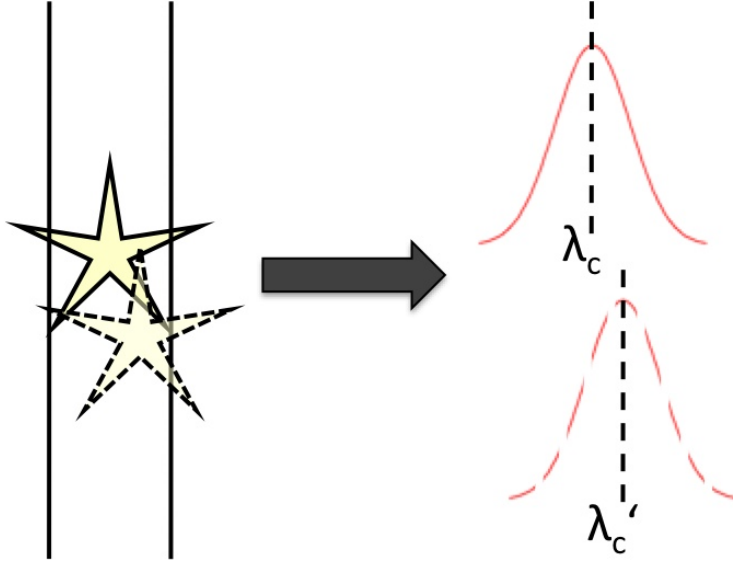


Figure 2.3: A relative displacement of object and slit between measurements (esp. due to imperfect telescope tracking) causes the detected barycentre to shift, impeding the comparability of subsequent measurements.

Where in conventional slit-spectroscopy telescope guiding errors pose a limiting factor to the instrument precision, fibres only partially retain spatial and angular information of the light at the spectrograph entrance (fig. 7.1). Thus, for different input illumination (science exposures as well as calibration) the fibre largely produces the same response, and therefore it stabilizes guiding induced signal variation. This property is referred to as *scrambling* in the literature (Avila & Singh, 2008). The advantage of fibre scrambling is that it permits the choice of a seeing-limited configuration, thus advocating the collection of a large fraction of the total flux, while angular as well as spatial distribution of the light intensity is maintained comparatively stable at the fibre output. The enhancement of the measurement stability can be quantified using the scrambling gain factor G (see fig. 7.1 and section 7.1.1):

$$G = \frac{d/D}{f/F}. \quad (2.7)$$

G defines the response f/F of beam displacement at the output (in units of the PSF's full-width of half-maximum F) to a certain input beam displacement d/D (in

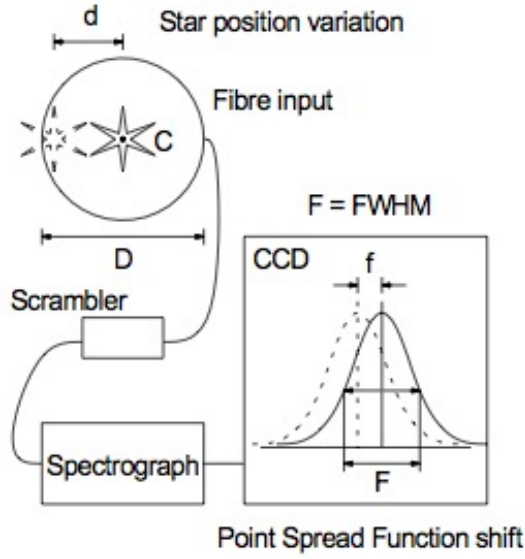


Figure 2.4: The scrambling gain G is defined as the ratio between shift d of the input illumination in units of the fibre core diameter D and the shift f of the barycentre of the resulting intensity pattern at the fibre output in units of the size of the FWHM F (see eq. 2.7).

units of the fibre core width D).

Eq. 2.6 thus becomes:

$$\Delta v_r = c \frac{\Delta \lambda_{lim}}{\lambda_0} = \frac{1}{G} \frac{c}{R} \quad (2.8)$$

This equation clearly illustrates a main advantage of fibre-spectrographs over conventional slit-spectrographs. Gain factors are typically of the order of 100 for the bare fibre (cf. section 7.1.2), improving the repeatability in measuring v_{rad} by the very same factor. However, fibre scramblers (Avila & Singh, 2008) can obtain G -values up to 1 000, where for the higher G -values serious throughput decrease is to be expected. For a spectrograph featuring high-resolving powers, e.g. HARPS with $R = 220\,000$, the bary-centre repeatability can achieve values of 30 cm s^{-1} . HARPS is first of all limited by the properties of the fibre and only when employing mitigation strategies (chapter 8) achieves photon noise limited values of 2 cm s^{-1} in radial velocity measurement. For this level of accuracy, also guiding errors, shifts in the calibration source, etc. need to be excluded.

2.3 Spectrophotometric uncertainties

The term *photometry* refers to the absolute flux measurement of the electromagnetic field, usually within a wavelength band. *Spectrophotometry*, however, measures the spectrally resolved absolute flux. The chemical composition and also the physical state of the material become available due to atoms interacting with the electromagnetic field. The energy $E = hc/\lambda$ of the wavelength observed, marks the transition between the atomic states involved and thus acts as a tracer for the element itself as well as its excitation state. Usually, several of these excitation states coexist and from the relative intensity of the lines, the temperature of the observed medium can be determined via Einstein-coefficients. A further influence of the temperature on the spectrum is Doppler-broadening, which widens the profile of the spectral line. A similar effect is pressure-broadening, which is discernible from Doppler-broadening due to its different nature and imprint on the line profile. Besides chemical abundances, pressure, temperature and density, spectral lines also allow for detection of magnetic fields as the Zeeman effect causes a splitting of the lines, the separation of the lines being an indicator for the strength of the magnetic field.

Temperature, pressure and magnetic field investigations complete our picture of stellar parameters. Amongst others, solar twins are studied, which can also reveal valuable clues about stellar evolution and the likelihood of finding planets in the habitable zone (Schuler et al., 2011; von Paris et al., 2011). These state-variables are likewise important for probing models of the interstellar medium (Flagey et al., 2011) and intracluster material (Weżgowiec et al., 2011) as well as gas and gaseous outflows (Giannini et al., 2011).

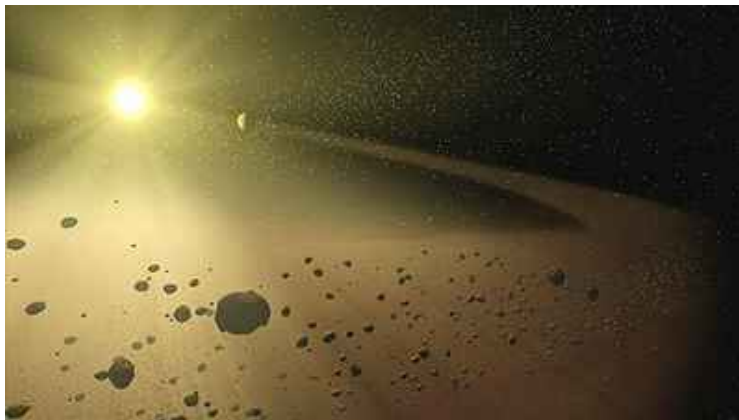


Figure 2.5: Artist concept of a debris disk and its host star (NASA JPL website, <http://www.jpl.nasa.gov/>). Debris disks are the progenitors of planetary systems and can help to reveal aspects of general planet forming mechanisms.

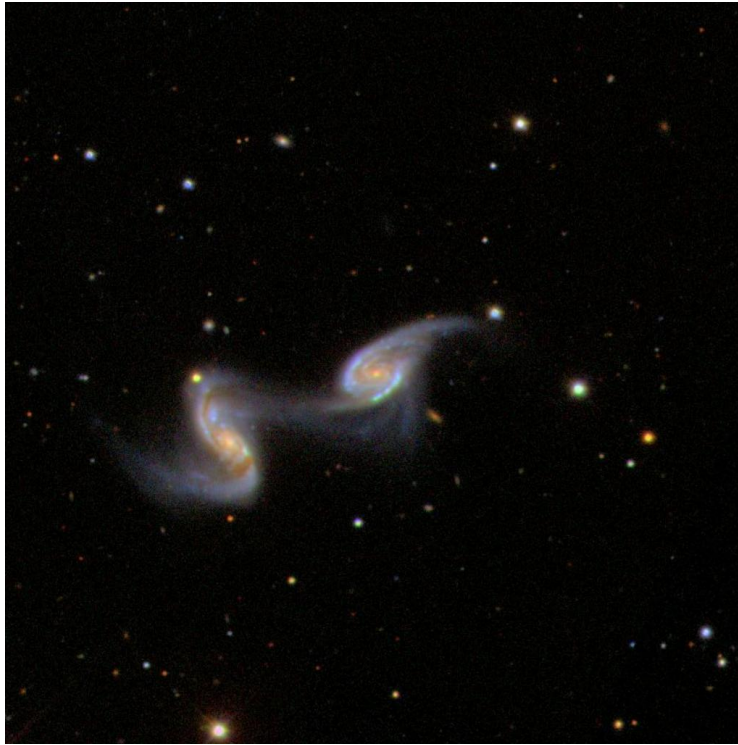


Figure 2.6: Galaxies merging, SDSS data (Galaxy Zoo <http://www.galaxyzoo.org/>). Observational studies of these objects can give valuable clues about galaxy formation.

The most prominent features of spectra are the hydrogen lines; the lightest and simplest element which forms the largest fraction of atomic matter in the universe. All other, heavier elements are generated in fusion processes and thus are an indicator for star formation and star formation rates. These are quantified by *metallicity*, where usually the ratio between a heavier atomic species and hydrogen is given (e.g. He/ H, Fe/H). Metallicity is an important tool for the investigation of a variety of objects and processes; from the study of stellar evolution (Bozkurt, 2011), star forming regions (Christie et al., 2011) and stellar clusters (Piatti, 2011; Faifer et al., 2011) to galaxy formation history and even systems of galaxies, where metallicity can reveal the different formation history of companions and merging galaxies as shown in fig. 2.6 (Bekki & Tsujimoto, 2011; Krabbe et al., 2011). Other highly topical fields of investigation include supernova remnants (Anderson et al., 2011), intergalactic material (Simcoe, 2011), the study of stellar debris disks as depicted in fig. 2.5 and the composition and genesis of planets following from the debris (Gonzalez, 2011; Rafikov, 2011).

The central figure of merit for all these applications is the signal-to-noise ratio (SNR) of the photometric accuracy, which, in night-observations is traditionally limited by

Poisson noise, i.e. the statistical limitation due to the low number of photons that arrive at the spectrograph. However, although faint objects such as distant galaxies or the intergalactic medium are certainly less affected by additional sources of noise, the limiting factor for the photometric accuracy above $\sim SNR = 200$ (depending on the spectrograph type) is the non-repeatability of throughput efficiency due to the employment of the optical fibre. The next generation of telescopes with their larger photon collecting power will therefore encounter an increasing number of objects that are limited by modal noise rather than Poisson noise.

For observations of our closest star, the Sun, these figures are even more of a concern. The photometric accuracy is often limited by the instrument performance, with $SNR > 10^5$ no longer uncommon. As will become clear in the next section, these precision levels are highly desirable in polarimetry in order to probe the Sun's magnetic field as well as its dynamics. The utilization of optical fibres as planned for the FASOT integral field spectrograph (Qu, 2011) requires careful assessment and mitigation strategies to make full use of the instrument's potential.

2.4 Modal noise in polarimetric measurements

Polarizing mechanisms can usually be traced back to asymmetric processes in the involved material or light-interacting fields, like scattering events and magnetic fields. Thus, polarimetry is a powerful tool that helps to reveal structures of an object that would otherwise be unavailable to the observer. As illustrated in the previous section, fibre related noise can severely limit the photometric accuracy. This can be especially crucial when performing comparative measurements, as is the case for polarimetry.

A polarimetric state can be described using the Stokes formalism (see e.g. Keller & Snik, 2009):

$$\mathbf{S} = \begin{pmatrix} S_0 \\ S_1 \\ S_2 \\ S_3 \end{pmatrix} = \begin{pmatrix} I \\ U \\ V \\ Q \end{pmatrix}, \quad (2.9)$$

where Q , U and V denote horizontal, vertical and circular polarization, and I the total intensity of the detected light.

The resulting polarimetric inaccuracy for known photometric inaccuracy in each measurement (e.g. due to modal noise) can be calculated from the relative inaccuracy $1/\sqrt{2}\sigma_I$ of each of the two channels. In these channels the intensities I_o and I_e

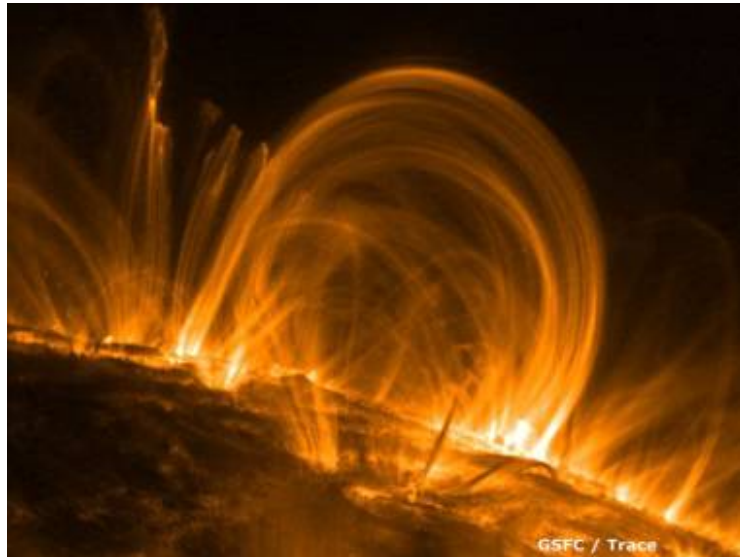


Figure 2.7: Sunspots are zones of extreme magnetic fields that disturb the heat conduction to the surface. As the sunspots grow larger and reach their maximum, protuberances and charged particles can be observed (source: <http://www.eso.org/>). A comprehensive study of the Sun's magnetic field requires a high precision in polarimetric measurement.

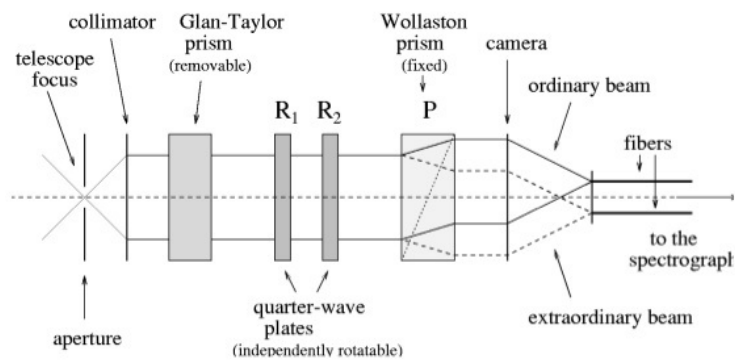


Figure 2.8: Sketch of a simple spectro-polarimeter setup (William-Wehlau Spectro-polarimeter Eversberg et al., 1998).

may be detected, referring to the ordinary and the extra-ordinary beam (cf. fig 2.8). For the following considerations, it is initially not important whether I_o and I_e are detected in physically separated channels or whether these two measurements are taken temporally independent of each other, although for practical reasons simultaneous measurements in general deliver more precise results. The measurement of S_0 and the other three Stokes parameters S_j ($j = 1, 2, 3$) involves the following calculations:

$$S_0 = I_e + I_o, \quad S_j = \frac{I_e - I_o}{I_e + I_o}. \quad (2.10)$$

Note that the light is for both channels polarized, which means that the number of excited modes is halved.

Using the error propagation law from eq. (2.10), the relative uncertainty σ_{S_j} and σ_{S_3} of the Stokes parameters can be derived. σ_I is the relative uncertainty of a single measurement due to modal noise:

$$\sigma_{S_0} = \sqrt{I_e^2 + I_o^2} \sigma_I, \quad \sigma_{S_j} = 2 \frac{2I_o I_e}{(I_o + I_e)^2} \sigma_I. \quad (2.11)$$

S_j becomes $\sqrt{2} \sigma_I$ for low polarization (i.e. $I_o \approx I_e$). This is only true for continuum polarization. In case the polarization of a spectral line is calculated, the non-repeatability of the barycentre will add to these uncertainties. For a measurement of e.g. the Zeeman shift of spectral lines at high resolving powers this might pose a severe limit, as the location of the barycentre in the required two measurements will be different. A closer inspection of this effect will be given in chapter 7.

A recent example, where the limited photometric accuracy of fibres can potentially set a severe imitation to the instrument performance is the Fibre Array Solar Optical Telescope (FASOT), which requires high polarimetric accuracy while at the same time employing high resolving power. This is the first instrument of its kind to use a fibre integral field technique in solar astronomy. Unlike many sources in night time observations, the Poisson limit due to the photon-flux of the Sun enables high polarimetric accuracy and high spectral resolution at the same time. The current instrument specifications are shown in table 2.1.

As follows from eq. (2.11), the polarimetric accuracy is directly proportional to the photometric accuracy. The results later presented in sections 5.3 and 6.3.2 imply that at high spectral resolving powers the modal-noise-limited photometric accuracy would not be high enough to achieve this science goal. This is especially true for de-

signs that feature a narrow slit in order to achieve the high spectral resolving powers. The FASOT instrument is a striking example where careful planning with regard to the initial design parameters will help to optimize the instrument performance. This becomes the more crucial as the traditional mitigation strategy of fibre agitation (chapter 8) may be impractical for an integral field unit that consists of 90×90 fibres.

Table 2.1: Design parameters for the FASOT spectrograph. Assumed fibre asymptotic focal ratio 4.0, Pixel size 15 μm . The central science requirements are marked in bold.

Parameter	value	unit
Telescope aperture diameter	0.80	m
Telescope focal ratio	10.00	
Focal Ratio at fibre input	7.0	
Spatial resolution	1.5	arcsec
Fibre core diameter	60	μm
Slit reduction factor	0.7	
Equivalent slitwidth	53.17	μm
Focal ratio at fibre output	4.95	
Spectral window	500- 1100	nm
Central wavelength	850	nm
Resolving power	120000	
Dispersion (Nyquist)	0.0035	nm/pixel
Blaze angle	71.6	deg
Collimator focal length	1063.5	mm
Beam diameter	214.9	mm
Minimum grating length	476	mm
Geometric throughput	0.74	
Signal to Noise due to modal noise	180	
Polarimetric accuracy	3.0×10^{-3}	
Temporal resolution	<10	s

Table 2.1 and fig. 2.9 show the heart of the modal noise problem: When aiming at higher spectral resolving powers, either the slit size needs to be reduced, resulting in higher modal noise, or the grating size exceeds feasible dimensions. Grating sizes above 0.5m are rare and usually too costive. The shown values are only initial estimates but serve as an illustration how the natural limitations within the design are potentially restricting the achievable polarimetric accuracy – the science specifications for the polarimetric accuracy are 1×10^{-3} , whereas the design limit at the largest feasible grating size might only allow for an accuracy of the order of 3×10^{-3} .

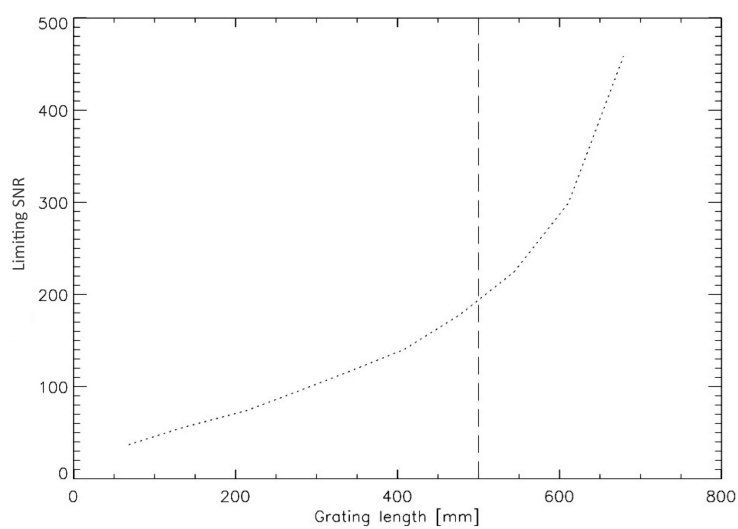


Figure 2.9: Estimated limiting noise for different grating sizes of the FASOT spectrograph, using specifications as shown in table 2.1 (modal noise only, does not account for background or poisson noise).

Chapter 3

Fibre properties

This chapter summarizes fibre properties and introduces the notations that will be used later throughout the thesis. The ray optical model (section 3.1) sufficiently describes most phenomena. However, in order to understand the mechanisms that cause modal noise, an electro-magnetic field analysis is necessary (section 3.2). The final sections briefly present modal noise and focal-ratio-degradation (FRD), phenomena that can be derived from the modal analysis.

3.1 Ray optical model

Light propagation in optical step index fibres is most basically described by total internal reflection at the junction between core and cladding of the fibre (see fig. 3.1(a)). Given the simplicity of the model, it is unable to describe coherence effects. Generally speaking, predictions using the ray optical model lose their validity when approaching fibre core diameters of the size of the applied wavelength ($\lambda \sim a$) as it is the case in single mode fibres (SMFs) or few mode fibres (FMFs). multi mode fibres (MMFs) are generally favoured, since they show lower coupling losses compared to FMFs or SMFs. Thus, for most astronomical applications, this model is broadly suitable for describing phenomena such as fibre losses, numerical aperture and the variation of propagation constants with changing coupling angle.

To each ray, a so called ray-invariant $\bar{\beta}$ can be assigned. This is a parameter that stays constant throughout the propagation process, the fraction of the propagation constant as projected on the optical axis:

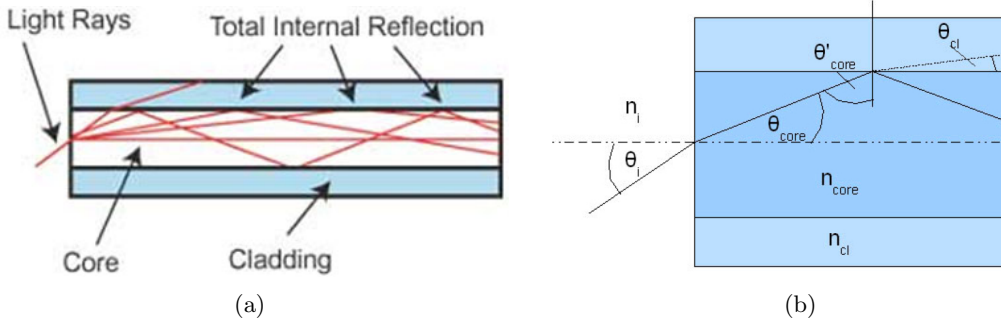


Figure 3.1: (a): Illustration of total internal reflections depicting the ray optical model, (b): Deduction of the numerical aperture.

$$\bar{\beta} = kn_i \sin \theta_i = kn_{core} \cos \theta_{core} = kn_{cl} \cos \theta_{cl}, \quad (3.1)$$

where k is the propagation constant in free space.

It can be shown (see Snyder & Love, 1983), that the conditions for coupling into the fibre and total internal reflection are solely dependent on the angle that the ray draws with the optical axis. Thus, for binding rays it holds

$$n_{core}k \geq \bar{\beta} > n_{cl}k \quad (3.2)$$

The first inequality ensures that the ray is coupled into the fibre, excluding total reflection at the air-core boundary. Furthermore, total internal reflection at the core cladding boundary has to take place, as indicated by the second inequality.

Eq. (3.1) is true for binding rays (rays that are supported by the fibre) as for non-binding rays (rays that pass through the core-cladding boundary and are thus lost, cf. fig. 3.1(b)):

Total reflection at the core-cladding junction occurs when (see fig. 3.1(b))

$$n_{core} \sin \theta'_{core} \geq n_{cl}. \quad (3.3)$$

From trigonometric relations, the condition is derived for the maximum angle θ_{core} :

$$\sin \theta_{core} = \sqrt{1 - \sin^2 \theta'_{core}} = \sqrt{1 - n_{cl}^2/n_{core}^2},$$

Where in the last step eq. (3.3) was used. Furthermore, using Snell's law, a maximum angle θ_a for coupling the light into the fibre can be derived:

$$n_i \sin \theta_i = n_{core} \sin \theta_{core} = \sqrt{n_{core}^2 - n_{cl}^2}, \quad (3.4)$$

The term on the left hand side of eq. (3.4) defines the numerical aperture of the fibre;

$$N.A. = n_i \sin \theta_i = \sqrt{n_{core}^2 - n_{cl}^2}. \quad (3.5)$$

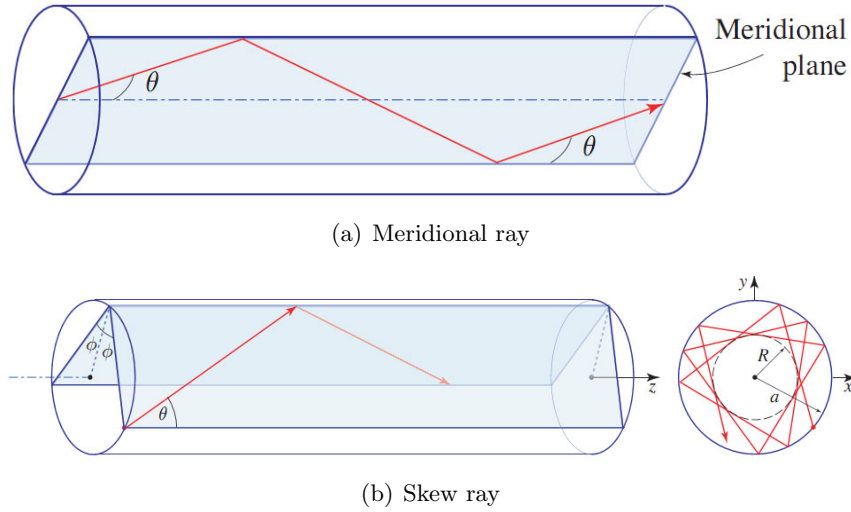


Figure 3.2: Two sets of modes distinct by their path of propagation: Meridional rays intersect the fibre axis, whereas skew rays propagate follow a helical path.

One distinguishes between two general groups of rays according to the way they are propagating through the fibre: Meridional rays (fig. 3.2(a)) intersect the fibre axis, whereas skew rays (fig. 3.2(b)) do not and therefore propagate along a helical path. The propagation velocity is only dependent on the rays propagation fraction $\bar{\beta}$ that is parallel to optical axis (z), independent of whether the ray is a skew ray or a meridional ray.

3.2 Mode model

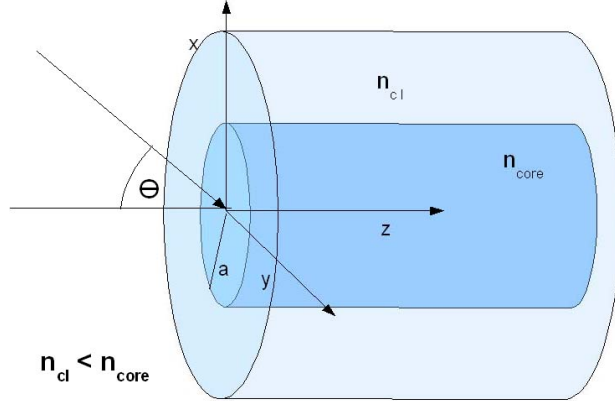


Figure 3.3: Nomenclature of fibre parameters: a - core radius, n_{cl} - cladding refractive index, n_{core} - core refractive index. The light is assumed to propagate in z -direction.

In the following, the modal properties of the circular step-index fibre are investigated as understanding of the phase information is crucial to understand the interference that emerges at the fibre exit (see section 3.4).

Although the solutions are well known (see Snyder & Love, 1983 or Buck, 1995), for clarity of nomenclature and for better understanding of the nature of modes this section will deal with the derivation of the waveguide solutions. A few examples of guided fields follow at the end of this section, as specific solutions will be used later in this thesis.

3.2.1 The coherent electromagnetic field

The electric field vector of a waveguide that is invariant in z , can be described as the superposition of mode fields \mathbf{E}_j :

$$\mathbf{E}_j(x, y, z) = \mathbf{e}_{tj}(x, y) \exp(i\beta_j z - i\omega t) \quad (3.6)$$

where j is the index that refers to a certain mode that is guided in the fibre. \mathbf{e}_{tj} is the time independent transverse electric field component (hence the subscript t) in the waveguide. The time component $-i\omega t$ in the exponential function can be omitted when considering monochromatic problems. However, when wave packets are propagating through the fibre, technically the time component in eq. (3.6) has to be included. The group velocity with which these wave packets are traveling is then given by $v_{g,j} = \partial\omega/\partial\beta$, whereas phase velocity is given in either case by $v_{ph,j} = \omega/\beta_j$.

Given the refractive indices of core and cladding of the fibre, propagation constants have to follow the same law as in eq. (3.2):

$$n_{cl}k < \beta_j \leq n_{core}k$$

3.2.2 The scalar wave equation

The electric field \mathbf{E} and the magnetic field \mathbf{H} are connected via source-free Maxwell equations. The dielectric constant ϵ is related to the dielectric constant in vacuum ϵ_0 by $\epsilon = n^2\epsilon_0$, while the magnetic permeability μ is very nearly the same as the permeability μ_0 in vacuum:

$$\begin{aligned} \nabla \times \mathbf{E} &= i(\mu_0/\epsilon_0)^{1/2}k\mathbf{H}, & \nabla \cdot \mathbf{E} &= 0, \\ \nabla \times \mathbf{H} &= -i(\epsilon_0/\mu_0)^{1/2}kn^2\mathbf{E}, & \nabla \cdot \mathbf{H} &= 0. \end{aligned} \quad (3.7)$$

\mathbf{E} and \mathbf{H} can be decomposed into longitudinal and transverse components, parallel and orthogonal to the z -axis, respectively

$$\mathbf{E} = (\mathbf{e}_t + e_z\hat{\mathbf{z}}) \exp(i\beta z); \quad \mathbf{H} = (\mathbf{h}_t + h_z\hat{\mathbf{z}}) \exp(i\beta z). \quad (3.8)$$

By eliminating either the electric or the magnetic field in eq. (3.7), the inhomogeneous vector wave equations can be obtained:

$$(\nabla^2 + n^2\mathbf{k}^2)\mathbf{E} = -\nabla(\mathbf{E}_t \cdot \nabla_t \ln n^2), \quad (3.9)$$

$$(\nabla^2 + n^2\mathbf{k}^2)\mathbf{H} = (\nabla \times \mathbf{H}) \times \nabla_t \ln n^2, \quad (3.10)$$

where $n = n(x, y)$ is the spatially dependent refractive index, and the subscript t relates to *transverse field* components. Assuming that n in a step index fibre is a constant *within* the core and the cladding, the $\nabla_t \ln n^2(x, y)$ -term vanishes and eq. (3.9) and eq. (3.10) can be summarized to obtain the *scalar wave equation*:

$$[\nabla_t^2 + n(x, y)^2k^2 - \beta^2] \Psi = 0. \quad (3.11)$$

Here, Ψ can be any scalar field component (x, y, z) of the electric or magnetic field. Solutions \mathbf{e}_j must be continuous at the core-cladding boundary.

With eqs. (3.9) and (3.10) it can be show that the transverse fields can be expressed in terms of longitudinal fields (see Snyder & Love, 1983). Thus, solving for the transverse field components is sufficient as the longitudinal components directly result from the transverse field components.

Given these general considerations of the electromagnetic field, the mode solutions derive from the constraints given by the fibre geometry as discussed in the next section. Basically, these steps will be followed:

- Formulation of the wave equation in cylindrical coordinates,
- Separation of $[\phi, r]$ in the wave equation; leads to Bessel functions,
- Formulate boundary conditions to find the numerical solutions.

3.2.3 Solving the scalar wave equation

Using cylindrical-polar coordinates, the field can be factorized into an azimuthal (ϕ -dependent) component and a radial component $f_l(r)$, so that eq. (3.11) can be split into two separate homogeneous problems. With the boundary condition $\Psi(0) = \Psi(2\pi)$ two groups of orthogonal solutions are possible:

$$\begin{aligned}\Psi &= f_l(r) \sin l\phi \\ \Psi &= f_l(r) \cos l\phi\end{aligned}\tag{3.12}$$

with l being a positive integer.

For the radially dependent factor f_l of Ψ eq. (3.11) becomes:

$$\left(\frac{d^2}{dR^2} + \frac{1}{R} \frac{d}{dR} - \frac{l^2}{R^2} + U^2 - V^2 g(R) \right) f_l(R) = 0.\tag{3.13}$$

R is defined as r/a (with a the radius of the fibre core). $g(R)$ is the normalized

refractive index profile. The dimensionless parameters U_j , W_j and V are defined as:

$$U_j = a\sqrt{k^2 n_{core}^2 - \beta_j^2} \quad (3.14)$$

$$W_j = a\sqrt{\beta_j^2 - k^2 n_{cl}^2} \quad (3.15)$$

$$V = ka\sqrt{n_{core}^2 - n_{cl}^2} = U_j^2 + W_j^2 \quad (3.16)$$

V is often called ‘normalized frequency’ as it states the input frequency in quantities of the (reciprocal) fibre dimensions. U and W are modal parameters and can be associated with the angle with which light is coupled into the fibre (cf. section 3.2.5). Solving eq. (3.13) for the radial component yields Bessel functions of the first kind (J) for the core and second kind (K) for the field outside of the core:

$$f_{core,l} = \frac{J_l(UR)}{J_l(U)} \quad (3.17)$$

$$f_{cl,l} = \frac{K_l(WR)}{K_l(W)} \quad (3.18)$$

using Bessel identities, this equation can be restated as:

$$f_{core,l} = \frac{J_{l+1}(U)}{J_l(U)} \quad (3.19)$$

$$f_{cl,l} = \frac{K_{l+1}(W)}{K_l(W)}. \quad (3.20)$$

Since the z -component needs to be continuous at the junction between core and cladding;

$$e_z(0 \leq R < 1) = \frac{J_{l+1}(U)}{J_l(U)} p(\phi) q(V, n_{core}, n_{cl})$$

$$e_z(1 \leq R < \infty) = \frac{K_{l+1}(W)}{K_l(W)} p(\phi) q(V, n_{core}, n_{cl}),$$

this results in a *characteristic function* to solve in U , W is then determined by eq. (3.16):

$$\frac{J_{l+1}(U)}{J_l(U)} = \frac{K_{l+1}(W)}{K_l(W)} \quad (3.21)$$

This equation cannot be solved analytically, so the next section will deal with the numerical derivation of solutions.

The labels ‘TE, TM modes’¹ as used in planar or rectangular waveguides, are no longer appropriate, since the field also inhibits longitudinal fractions in both E and H field. Modes in the circular wave guide have rather to be seen as hybrid modes having e_{z_j} and h_{z_j} components, hence called ‘HE’ and ‘EH’ modes - depending on which component has a longitudinal fraction in z -direction, then either ‘H’ or ‘E’ is the first letter (note that there are no TEM modes).

3.2.4 The characteristic equation

Solving eq. (3.21) is a numerical problem. To find the electric fields as shown in tables 3.2 and 3.2.4 the following procedure was used: V and l were taken as fixed to find all points U where this function turns zero:

$$\frac{J_{l+1}(U)}{J_l(U)} - \frac{K_{l+1}(W)}{K_l(W)} \stackrel{!}{=} 0 \quad (3.22)$$

The solutions were numbered serially; 1,2,... which gives the m index of the respective mode LP_{qm} (for historical reason, $q = l + 1$ for HE modes and $q = l - 1$ for EH modes). Depending on the fibre core size, a certain number of mode groups need to be considered. As mentioned above the V parameter in eq (3.6) can also be seen as a frequency, but its reciprocal resembles also a normalized fibre core size in units of wavelength and refractive index differences. This has the advantage of generalization; the solutions can be applied to fibres of different refractive index, core sizes and different wavelengths.

Solving for the transverse electric field and expressing the solutions in Cartesian coordinates $\Psi = \mathbf{e}_t = e_x(x, y)\hat{\mathbf{x}} + e_y(x, y)\hat{\mathbf{y}}$, eq. (3.12) results in four different groups of solutions in the electric field:

$$\begin{aligned} \mathbf{e}_1 &= f_l(R)(\cos l\phi\hat{\mathbf{x}} - \sin l\phi\hat{\mathbf{y}}) \\ \mathbf{e}_2 &= f_l(R)(\cos l\phi\hat{\mathbf{x}} + \sin l\phi\hat{\mathbf{y}}) \\ \mathbf{e}_3 &= f_l(R)(\sin l\phi\hat{\mathbf{x}} - \cos l\phi\hat{\mathbf{y}}) \\ \mathbf{e}_4 &= f_l(R)(\sin l\phi\hat{\mathbf{x}} + \cos l\phi\hat{\mathbf{y}}) \end{aligned} \quad (3.23)$$

The first two can be assigned to the EH modes, whereas the last two constitute the

¹TE = transverse electric, TM = transverse magnetic

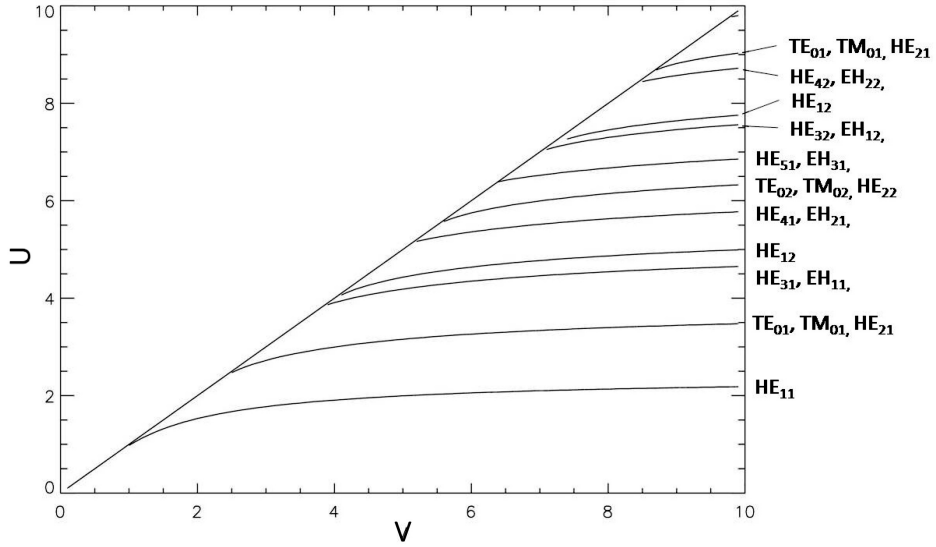


Figure 3.4: Solutions for the characteristic equation

members of the HE groups.

Table 3.1: Mode fields and indices, electric field definition as in eq. (3.23)

$l=0$	q	mode field
HE even	1	$e_1=e_2$
HE odd	1	$e_3=e_4$

$l=1$	q	mode field
HE even	2	e_1
HE odd	2	e_3
TM	0	e_2
TE	0	e_4

$l > 1$	q	mode field
HE even	$l + 1$	e_1
HE odd	$l + 1$	e_3
EH even	$l - 1$	e_2
EH odd	$l - 1$	e_4

For the $l=1$ case, for the EH fields either the electric field or the magnetic field become zero in the direction of propagation. The resulting field is then called either transverse magnetic (TM) or transverse electric (TE) mode.

3.2.5 Propagation constants

In the previous section it was shown how the electromagnetic field splits into field components that are guided by the circular optical fibre. The following considerations should enable a more descriptive view of the parameters that have been discussed so far; as well as a few simplifications that can be made in order to allow for a more efficient use of computing resources when simulating mode propagation in fibres (e.g. section 5.1).

For a known U_j -value (as calculated solving the characteristic equation), the propagation constant can be directly derived using eq. (3.14);

$$\beta_j = \sqrt{k^2 n_{core}^2 - U_j^2/a^2}.$$

From eq. (3.1) with $\beta_j = \bar{\beta} = kn_i \sin \theta_i$ we can thus assign a certain input angle θ_i to each value that is a solution U_j to the characteristic equation. Following the approach by Gloge (1971) it is useful to introduce the parameter b

$$b = 1 - \frac{U_j^2}{V^2},$$

which can be shown to be approximately the normalized propagation constant for the weakly guiding case (i.e. $(n_{core} - n_{cl})/n_{cl} \ll 1$):

$$b \approx [(\beta/k) - n_{core}] / (n_{cl} - n_{core}).$$

In terms of the relative difference of refractive index Δ :

$$\Delta = (n_{core} - n_{cl})/n_{cl} \ll 1,$$

the propagation constant becomes (Δ is assumed to be small):

$$\beta_j = n_{cl}k \left[1 + \Delta \left(1 - \frac{U_j^2}{V^2} \right) \right]. \quad (3.24)$$

Here it should be mentioned that astronomical applications favour rather high Δ in

Table 3.2: Electric fields and intensities for the first binding modes of a step index fibre, generated in IDL.

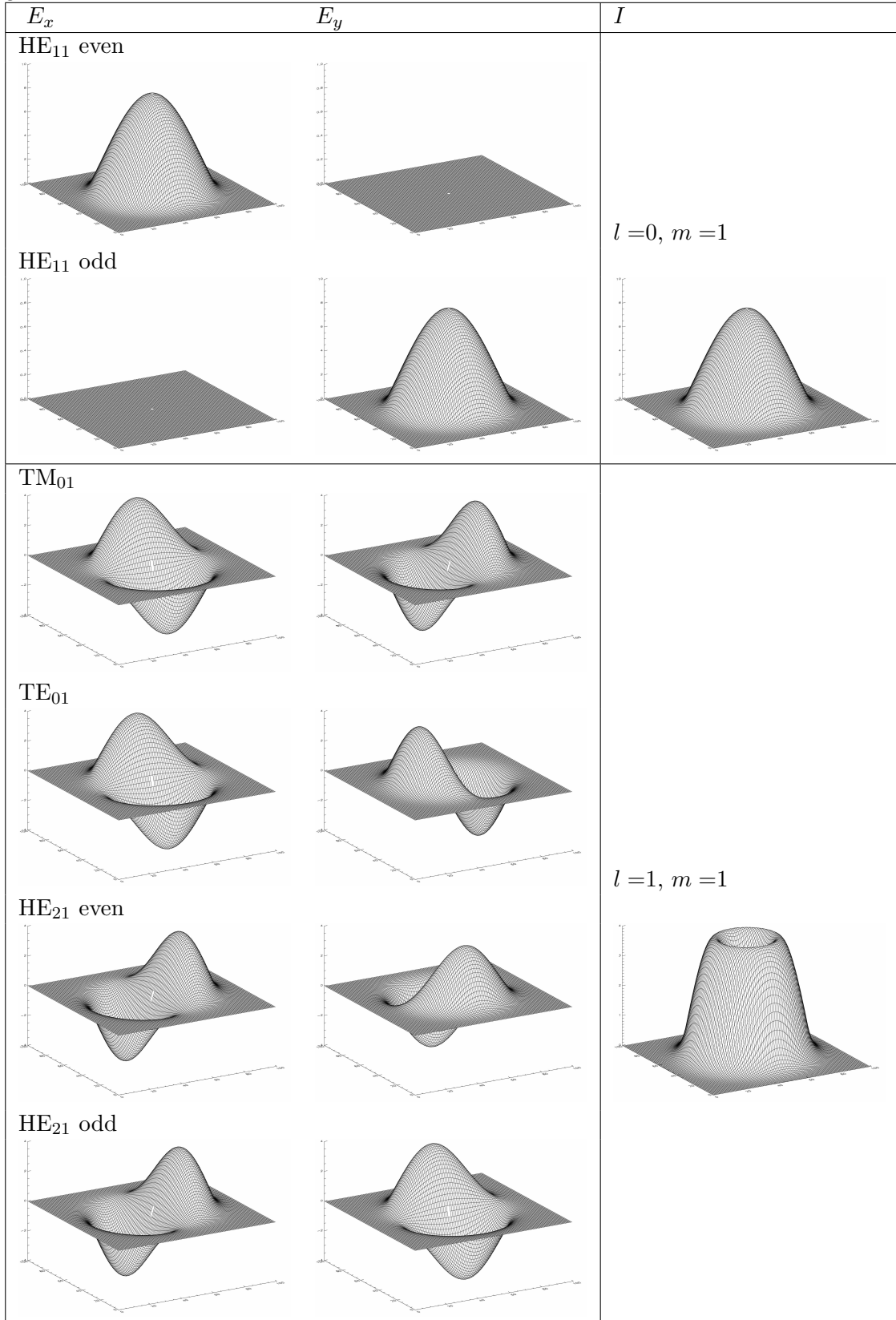
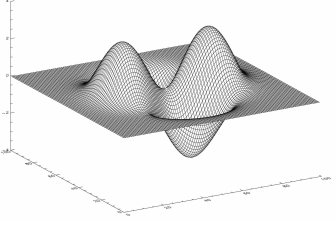
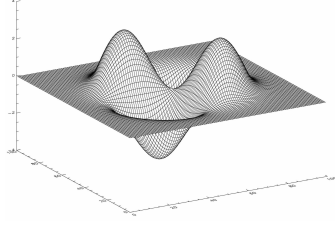
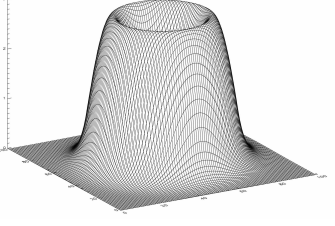
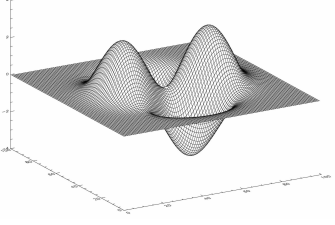
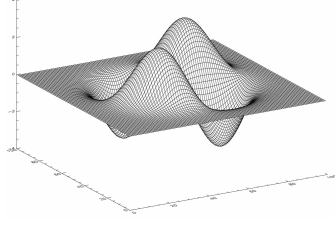
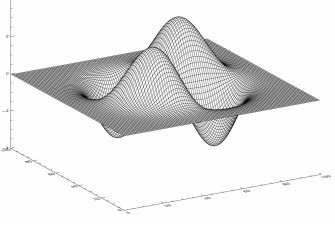
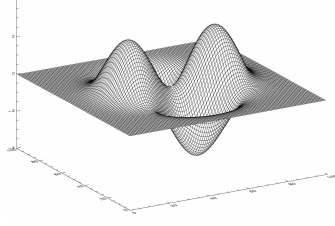
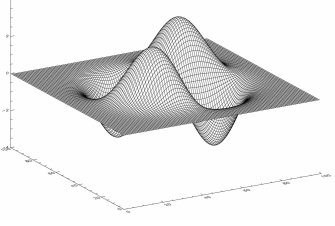
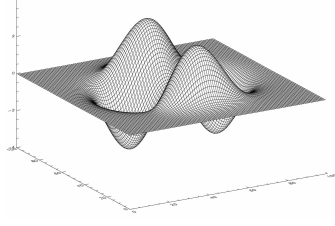
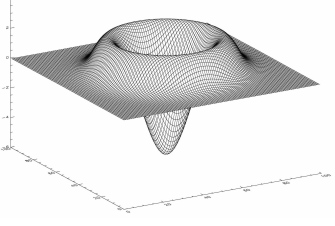
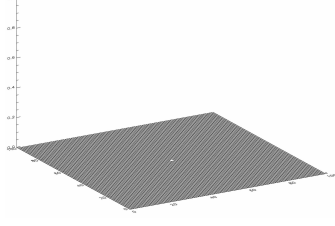
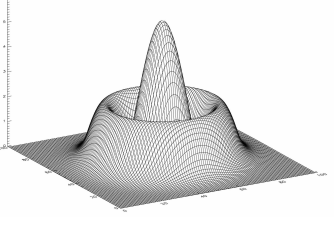
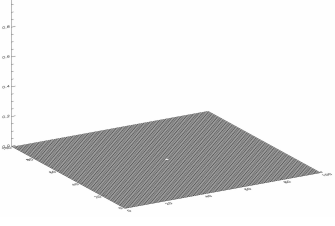
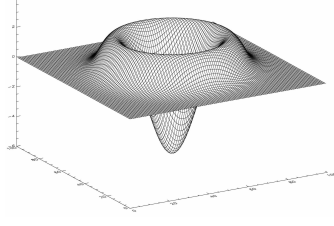


Table 3.2 continued

E_x	E_y	I
<p>HE₃₁ even</p> 		<p>$l=2, m=1$</p> 
<p>HE₃₁ odd</p> 		
<p>EH₁₁ even</p> 		
<p>EH₁₁ odd</p> 		
<p>HE₁₂ even</p> 		<p>$l=0, m=2$</p> 
<p>HE₁₂ odd</p> 		

order to realise high focal ratios and thus minimise focal ratio degradation (FRD) but the refractive index difference for potential materials is still only within the range of 1% - 2%, depending on which limiting focal ratio is desired. Thus, the weakly guiding approximation should be valid to a certain level of accuracy.

For weakly guiding fibres just the cutoff frequency has to be known, then U_j can be simplified to

$$U_j = U_{jc} \exp \left\{ \frac{1}{s} \left[\arcsin \frac{s}{U_{jc}} - \arcsin \frac{s}{V} \right] \right\}, \quad \text{with } s := (U_{jc}^2 - l^2 - 1)^{1/2}$$

with U_{jc} being the cut-off frequency (the frequency at the lowest V value at that the mode occurs, see fig. 3.4). This equation is not valid for the HE_{11} -mode, where the result is

$$U_j(V) = (1 + \sqrt{2})V / \left[1 + (4 + V^4)^{1/4} \right].$$

These U_j can be used to calculate the propagation constants via eq. (3.24). However, further simplification can be done for multimode fibres (MMF).

3.2.6 Propagation constant in multimode fibres

With large fibre core size, the conclusions that can be drawn from the ray optical model (section 3.1) are valid. The acceptance angle was given by eq. (3.5):

$$\theta \approx n_i \sin \theta = (n_{core}^2 - n_{cl}^2)^{1/2}.$$

Modes occur perpendicularly polarised in pairs, each pair occupying a solid angle of $\pi\delta^2$, where $\delta = \lambda/a\pi$. So that the number of modes can be estimated by

$$M \approx 2(\theta/\delta^2) = V^2/2, \tag{3.25}$$

in the last step the definition of V (eq. (3.16)) was used. Since $V \approx U_c$, the cutoff of the ν th mode is approximately at

$$U_c = (2\nu)^{1/2}.$$

Which is only valid for large values of ν .

Furthermore, U can be replaced by U_c because U never departs very much from its cutoff value. Thus, the normalized propagation parameter becomes

$$b = 1 - (U_c^2/V^2) = 1 - (\nu/N).$$

Thus, for the propagation constant it can be derived:

$$\beta = \left[\left(1 - \frac{\nu}{N}\right) (n_{core} - n_{cl}) + n_{cl} \right] k. \quad (3.26)$$

3.3 The Coupling Integral

For a given electromagnetic field at the fibre entrance the power that is coupled into each mode can be calculated. To do this, the field expansion can be examined:

$$\mathbf{E}(x, y) = \sum_j a_j \mathbf{E}_j(x, y) + \sum_j a_{-j} \mathbf{E}_{-j}(x, y) + \mathbf{E}_{rad}(x, y) \quad (3.27)$$

$$\mathbf{H}(x, y) = \sum_j a_j \mathbf{H}_j(x, y) + \sum_j a_{-j} \mathbf{H}_{-j}(x, y) + \mathbf{H}_{rad}(x, y). \quad (3.28)$$

Where the first part is the part of the field that travels forwards through the fibre. The power in the modes j are expressed in the amplitudes a_j . The subscript $-j$ denotes the backwards traveling modes and \mathbf{H}_{rad} , \mathbf{E}_{rad} are the radiation fields. As backwards traveling fields will not be considered here and the radiation fields do not couple into the fibre, the task is to determine the a_j . Note here that the a with subscript are referring to the amplitudes in the field expansion whereas in earlier section a (no subscript) referred to the fibre core radius.

The electromagnetic field expansion is comparable to the expansion in Fourier coefficients in functional analysis, from the properties of the modes described in section 3.2 it can be shown that they fulfill the orthogonality relation (* indicates complex conjugate):

$$\frac{1}{2} \int_{A_\infty} (\mathbf{e}_j \times \mathbf{h}_k^*) \cdot d\mathbf{A} = \frac{1}{2} \int_{A_\infty} (\mathbf{e}_j^* \times \mathbf{h}_k) \cdot d\mathbf{A} = \begin{cases} N_j & \text{for } j = k \\ 0 & \text{for } j \neq k \end{cases} \quad (3.29)$$

where N_j is the the power that is contained in the j 's mode. Furthermore, the fibre modes are orthogonal to the radiation modes, i.e.

$\int d\mathbf{A} \cdot \mathbf{E}_{rad} \times \mathbf{h}_j^* = 0$ (analogue for \mathbf{H}_{rad}). Thus, by multiplying eq. (3.27) with \mathbf{h}^* and eq. (3.28) with \mathbf{e}^* and utilizing (3.29), the a_j can be calculated:

$$a_j = \frac{1}{2N_j} \int_{A_\infty} (\mathbf{E}_t \times \mathbf{h}_{tj}^*) \cdot d\mathbf{A} = \frac{1}{2N_j} \int_{A_\infty} (\mathbf{e}_{tj}^* \times \mathbf{H}_t) \cdot d\mathbf{A}. \quad (3.30)$$

For a better understanding of the above statement the definition of the Poynting vector can be considered:

$$\mathbf{S} = \mathbf{E} \times \mathbf{H}, \quad (3.31)$$

a measure for the electromagnetic flux per unit area. The total power that passes through the infinite plane A_∞ is then

$$P_{tot} = \int_{A_\infty} \mathbf{S} \cdot d\mathbf{A}. \quad (3.32)$$

Comparing (3.32) with (3.30), the a_j 's essentially are a measure for the energy flux P_j that is contained in the j -th mode, normalized by the N_j 's defined by (3.29):

$$P_j = |a_j|^2 N_j. \quad (3.33)$$

The total power of the transmitted field is therefore $P = \sum_j P_j$.

Furthermore, due to Fresnel reflection at the fibre input the fraction of the transmitted field \mathbf{E} and \mathbf{H} is:

$$\mathbf{E}_t(\theta_t) \cong \frac{2n_i}{n_i + n_c} \quad (3.34)$$

$$\mathbf{H}_t(\theta_t) \cong \frac{2n_i}{n_i + n_c} \quad (3.35)$$

This must be considered when deriving the amplitudes a_j in eq. (3.27).

A further simplification for the computation of the a_j is possible for the weakly guiding case, where the longitudinal components are 0 ($e_z = h_z = 0$) and for the transversal components thus follows: $\mathbf{h}_t = n_c \sqrt{\epsilon_0/\mu_0} (\hat{\mathbf{z}} \times \mathbf{e}_t)$. If we further consider

only coupling under small angles, eq. (3.30) can be then simplified to:

$$a_j = \int_{A_\infty} \frac{\mathbf{E}_x \mathbf{e}_{xj}^*}{|\mathbf{e}_{tj}|^2} \cdot d\mathbf{A}. \quad (3.36)$$

Eq. (3.36) is a normalized scalar product of the input x -field with the x -component of the fibre mode (same considerations are applicable for the y -components), thereby displaying the close analogy of a_j to Fourier expansion coefficients.

The small angle restriction is of little practical concern for weakly guiding fibres as the acceptance angle $\theta_c = (1 - n_{cl}^2/n_c^2)^{1/2}$ already limits the possible range of incident angles to $\theta_i \ll 1$.

3.4 Speckle formation

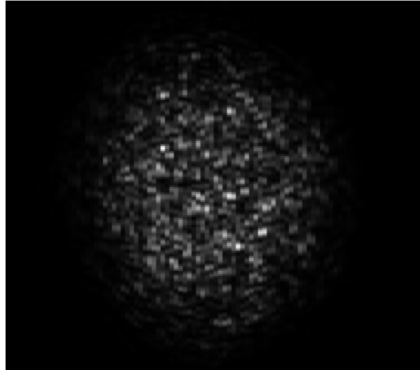


Figure 3.5: Typical speckle pattern of the fibre far-field, obtained by coupling coherent light into the fibre. HeNe laser (632.8 nm), core size 100 μm , collimated beam input.

Uniform illumination of a multi mode fibre with coherent light results in a speckle-like pattern at the fibre endface (and likewise in the farfield, see fig. 3.5). Its appearance is quite similar to the pattern that occurs when scattering coherent light on rough surfaces. The speckle pattern can be explained by considering that the different modes possess different traveling times, thus resulting in phase differences when reaching the fibre endface. Impurities of the non-ideal fibre lead to phase shifts and slightly different geometries of the modal fields as to those shown in table 3.2. Thus, the pattern is not symmetric and maxima of intensities look rather irregularly distributed (see section 4.2.2).

The coherence of the light source is a crucial factor here, since a time varying phase relation would result in a continuously changing intensity pattern. Averaged over

infinite time, the result would be a gaussian distribution of intensity throughout the fibre surface. Using partially coherent sources causes the measured noise to decrease (see Corbett, 2006). Therefore, experiments conducted in chapter 6 used a He-Ne line filter to ensure a narrow waveband $\delta\omega$ and thus coherence for the duration of the integration time.

3.4.1 Open and closed speckle regime, microbending

For an ideal fibre a mode, once excited, would maintain its initial power until exiting the fibre at the other end. This situation is called closed speckle pattern regime, where the speckles can be treated as being statistically dependent using Bayes law (see Hjelme & Mickelson, 1983). However, scattering (i.e. defects in the fibre) cause the modes to exchange power, also exciting higher order modes (manifesting in focal ratio degradation) and radiation modes, i.e. causing the fibre to lose light. Allowing the modes to exchange power at random causes independence between the speckles, this is called open regime. Accounting for microbending leads to a mixture between open and closed speckle statistics, including also radiation modes, i.e. losses due to spatial filtering.

3.5 Focal ratio degradation

In optical systems, étendue plays the analogous role of entropy in thermodynamics. It describes how spread out the light beam is. Scattering events increase the étendue, a mechanism that is irreversible. The ideal optical system is étendue conserving, lowering the étendue is impossible without losing information and power. Étendue is also known as the $A\Omega$ -product (the product of solid angle and surface area of the considered light cone) and a parameter of conservation for the ideal optical system. Particularly in spectroscopy the étendue determines the size of the collimated beam and thus the size of the grating. This leads to unfavorable scaling laws: The larger the telescope aperture, the larger the beam size and the grating, thus rising instrument costs.

In the works by Gloge (1971) and Carrasco & Parry (1994), the behavior of fibres under different focal ratio feed is described: Feeding the fibre close to the numerical aperture, the fibre encounters almost no FRD, behaving like an ideal fibre. However, the slower the beam, the more the output focal ratio gets degraded until it reaches a certain maximum (F_{max}). It is common to describe the output focal ratio F_{out} as

a function of the input focal ratio F_{in} in the following way:

$$F_{out} = [F_{max}^{-2} + F_{in}^{-2}]^{-1/2}. \quad (3.37)$$

There seems to be a link between the modal power distribution (MPD) and FRD: As can be seen from section 3.2.6, light that is coupled under a higher angle corresponds to a higher order mode, i.e. focal ratio degradation is identical to the coupling of higher order modes. However, it is not obvious, whether this increased mode number has a direct influence on modal noise (see discussion section 6.4).

3.6 Summary

In this chapter the basic ray optical model and mode model were presented. The modal field propagation results will be repeatedly used in part II and explains how the speckle pattern arises and its possible link to focal ration degradation.

Part II

Investigations on measurement uncertainties

Chapter 4

A critical assessment of the current state of research on modal noise

This chapter is intended to establish the investigation within the framework of current understanding of fibre modal noise. A literature review is presented, wherein the critical aspects necessary for modal noise prediction will be highlighted. The discussion is then further expounded to address the options for modal noise simulation. The chapter concludes with a simplified analytical picture that will be investigated in chapter 6, where the experimental investigations of modal noise will be dealt with.

As we learned from section 3.4, the inhomogeneous intensity distribution at the fibre exit can limit the accuracy in high-resolving spectroscopic applications. The two aspects of main concern are (i) the photometric accuracy; and (ii) the bary-centre position of spectral lines. This chapter will investigate the first aspect, concentrating on the status of the current research in order to outline a predictive model. It will become evident that two major properties of the speckle pattern are crucial: The number of speckles and the contrast of the pattern. Each section will be discussed separately and combined to form a consistent model. A further section deals with the simulation of the speckle pattern. In the course of the discussion it will become evident that the current models are encountering limitations, and thus has moti-

vated the experimental research which is described in chapter 6.

4.1 Overview

Epworth (1979) first noted that the modal properties of fibres will limit the accuracy of intensity measurements. Inherent fibre properties cause a speckle pattern at the fibre exit which is subject to changes in the fibre condition, e.g. stress or temperature shifts. In conjunction with a mode filtering process, the speckle pattern causes fluctuations in the intensity measurement, thus affecting the photometric accuracy, an effect that was first quantified by Hill et al. (1980), and soon followed by Goodman & Rawson (1981). As was pointed out by Grupp (2003) spatially filtering apertures are often deployed, e.g. fibre-slit at the spectrograph entrance or by overfilling the grating.

Rawson et al. (1980) studied the bandwidth-dependence of the speckle contrast: A lower coherence (e.g. in low-resolution spectrographs) results in diminished speckle contrast (low visibility). This theory predicts a length-dependence of the visibility which they experimentally verified for fibre lengths of several km. However, the fibre-length dependence was disproven for lengths $\leq 10^2$ m by Baudrand & Walker (2001) and Corbett (2006), a regime particularly interesting for astronomical applications. This indicates that there are other effects that dominate here and the picture of the fibre as an ideal wave-guide has to be treated with caution.

The first study to combine coherence effects and speckle statistics into a concise model is conducted by Kanada & Aoyama (1983). A prediction of the wavelength-dependent spectrograph response was achieved by Chen et al. (2006) for few-mode fibres. Their mode-propagation simulation is in excellent agreement with experimental findings, allowing for precise modal noise prediction. But the multi-mode case is more complex and already the absence of strong fibre-length dependence suggests that theoretical picture of light propagation in optical fibres is not yet sufficiently developed.

Modal noise will limit stellar observations that measure metallicities or make use of analytical tools like the Stark effect for temperature determination. Studies on interstellar material measuring ionization levels will ultimately also be limited. Furthermore, for solar observations working at high resolution, high signal-to-noise levels are affected (e.g. high-precision-polarimetry). See chapter 2 for further detail.

With the construction of ELT's, ever larger telescope apertures will become avail-

able, for the study of stellar atmospheres. As a result, unprecedented light gathering capacities will facilitate improved photon statistics. For the medium to high resolution instrument the signal to noise ratio is thus ultimately limited by the throughput stability of the employed optical fibre, affecting the measurement of important parameters such as effective temperature, gravity, metallicity and turbulences. Similarly affected are investigations that focus on the determination of line ratios, e.g. for ionization levels of interstellar material or in accretion disks of active galaxies. Little is known about the effects of using fibres for solar observations but as the high photon flux rates would provide potentially precise measurements, the impact of modal noise can become a dominant concern for instrument development (see discussion section 2.4).

These new requirements therefore need thorough investigations that explain the phenomenology and reasons for the occurrence of spectral modal noise and that ultimately demands a predictive model, which will be vital for future instruments. In the following a detailed description of the current state of research will be given regarding mode filtering (section 4.2) as well as the influence of coherence effects (section 4.3). Afterwards (section 4.3.5), Chen's approach for simulating electromagnetic field propagation will be presented and adapted to the few mode case. With this framework an analytical model is attempted (section 5.3) which will be tested by experiment in chapter 6.

4.2 Modal statistic approaches

With the advent of commercially available fibres, a first strong incentive for the thorough study of fibre modal noise was triggered by the rapid developments in telecommunications. As a result, fibre related noise is a well studied field, although predominantly concentrated on highly monochromatic light. Hence, it is not surprising that the first publications (Epworth, 1979; Daino et al., 1980) focus solely on mode statistics and mode-filtering processes, in fact the fundamentals of fibre modal noise can only be understood, when considering this basic aspect.

This section therefore deals with the statistical assumptions that allow the prediction of modal noise for the highly coherent case, before elucidating on the influence of low coherence that is often to be found in astronomical spectrographs (section 4.3). The occurrence of modal noise can be traced back to three main aspects (compare fig. 4.1):

- Speckle pattern (as in section 3.4)
- Its variance, e.g. due to change in fibre stress

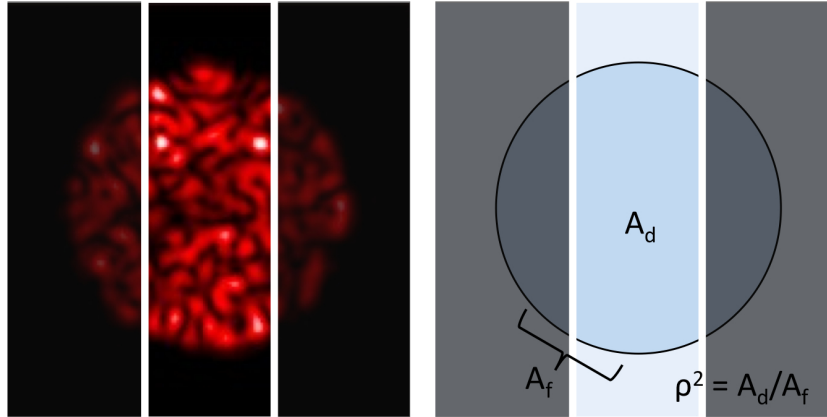


Figure 4.1: Modal noise originates from truncating the beam of an inhomogeneous, time-varying intensity distribution. The essential geometrical variable ρ^2 is defined by two parameters; A_f is the area of the fibre image, whereas A_d is the part of the illuminated area that is detected.

- A mode filtering process (for instance interaction with an aperture)

In confined waveguides as represented here by the standard optical fibre, the electromagnetic field has to fulfill certain boundary conditions. As a result, only the fraction of the light that matches the potential walls can propagate through the fibre and is quantized into fibre modes (see sections 3.2.4 and 3.4). The typical fibre differs from the ideal circular symmetric waveguide; along the length of the fibre a variation of parameters like core-diameter and refractive index occurs. These statistical properties cause a change in symmetry and phase relation of the supported modes, a phenomenon that manifests in a speckle pattern as in fig. 4.1, that becomes apparent when the fibre output is observed in coherent light.

4.2.1 Daino et al.: Square root law

In his paper, Daino et al. (1979) had not yet directly accounted for the filtering as being a process due to restricting apertures and made some general theoretical assumptions verified by experimental results:

Assuming the speckle occurrence is random, Γ -statistics should be applicable, yielding a simple square root law for the modal noise N_{mod} (Note: Later on, this approach proved to have limited validity only, cf. section 4.2.2):

$$N_{mod}/S = \sqrt{M}, \quad (4.1)$$

with signal strength S and M being

$$M = \frac{1}{2}V_{mode}^2, \quad (4.2)$$

the number of guided modes which is approximately equal to the number of speckles in the near field of the fibre; and $V_{mode} = ka\Theta$ (where k is the free space propagation constant and a the fiber radius, Θ the angle of the light cone with which it is coupled into the fibre). Thus, modal noise is a function of the supported modes - and more importantly; *linear* to the signal strength. The overall signal to noise in the fibre coupled spectrograph is then determined to:

$$S/N = \frac{S}{\sqrt{S + N_{bg}^2 + N_{ron}^2 + N_{mod}^2}}, \quad (4.3)$$

with N_{ron} - the detectors read-out noise, \sqrt{S} - the Poisson noise contribution and N_{bg} the background noise, e.g. sky and dark current. Hence, with increasing signal strength, the modal noise contribution becomes dominant over the other sources of noise.

4.2.2 Goodman and Rawson: Constrained Speckle

Goodman and Rawson's criticism of this simplified speckle analysis was that the simple square root law in eq. (4.1) does not explain measurements of modal noise for the limit of unrestricted beams. For the unobscured fibre, the intensity at the spectrograph output should be stable, thus, the modal noise should vanish. This is indeed the case, as can be seen from the experimental data in fig. 4.2. Previous studies used Γ -statistics, which assumes that the detected modes varies according to a Poisson distribution between measurements. This is not entirely correct, since the number of modes (and thus: speckles) over the entire fibre endface remains stable, just the number of speckles that is obscured is varying. The number of detectable speckle is constant which puts a constraint on the statistics, the intensity measurement rather follows a so called β -distribution (see Bevington, 1969).

Note: for small ρ^2 the Γ -statistic still remains a good approximation, as the number of speckles transmitted to the detector plane follows closely the Poisson distribution, whereas for $\rho^2 \rightarrow 1$ the number of speckles is limited to the number of total guided modes due to the fibre.

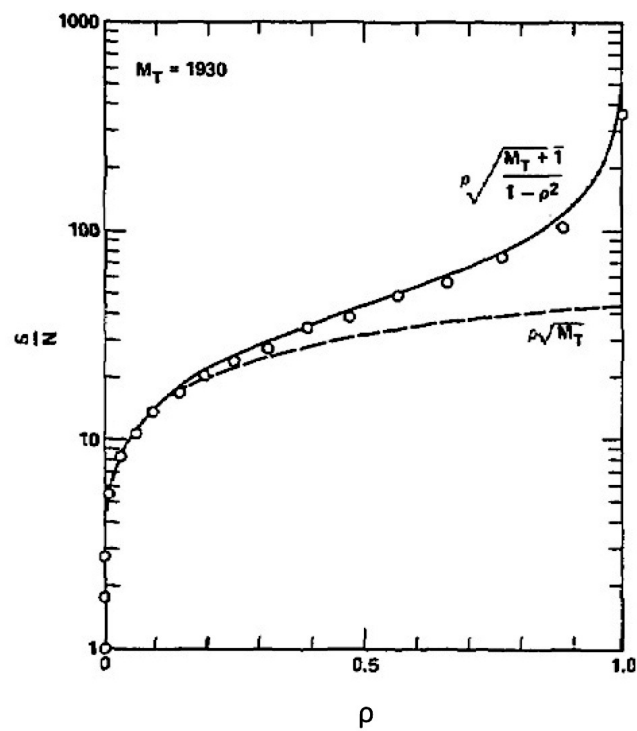


Figure 4.2: Signal to noise ratio as a function of fractional detector area. The dashed curve represents the square root law in the conventional theory. The circles are experimental data. The solid curve represents the prediction of eq. (4.4). M_T is the number of supported modes (Goodman & Rawson, 1981).

$$S/N = \rho \sqrt{\frac{M+1}{1-\rho^2}}, \quad (4.4)$$

dependent on a variable ρ that describes the extend of obscuration:

$$\rho^2 = \frac{A_d}{A_f}, \quad (4.5)$$

with A_d is the area of the detector the fiber end face is imaged onto and A_f fiber cross-sectional core area, M is the number of modes propagating in the fibre.

The theoretical approach by Goodman & Rawson is based on counting the numbers of the degrees of freedom that are associated with the speckle pattern, resulting in a model that becomes singular ($S/N \rightarrow \infty$) for the unobscured case as required. The model prediction is well supported by their experimental results, although for $\rho^2 \rightarrow 1$ other mode filtering processes appear to set in, so that the experimental data are below the theoretical prediction. Note also that the low ρ^2 -regime follows closely the square-root law as derived by Daino et al. (1979).

Astronomical applications predominantly favour high throughput rates as this improves the signal in respect to Poisson noise. Then, the square root law is no longer applicable and it overestimates the modal noise. On the other hand, spectral resolution can often be increased by reducing the slit-width at the spectrograph entrance, but at the expense of increasing modal noise.

4.2.3 Baudrand and Walker: Modal noise as a function of wavelength

In their paper Baudrand & Walker (2001) investigated the signal-to-noise ratio (SNR) as a function of wavelength. As the number of modes should decrease with λ^{-2} , the SNR should increase with λ according to eq. (4.1). Their experimental test apparatus consisted of a multimode fibre fed Cherny-Turner spectrograph. Instead of the expected square-root law, the fibre-related signal-to-noise showed the following dependence:

$$S/N_{mod} = M_\lambda^{0.784}. \quad (4.6)$$

Another interesting result of their investigations is the similarity in modal noise performance at a spectrograph resolution of 3×10^5 for a 7 m and a 70 m long fibre, although the contrast of the speckle pattern (and thus the intensity fluctuation between measurements) should decrease with fibre length.

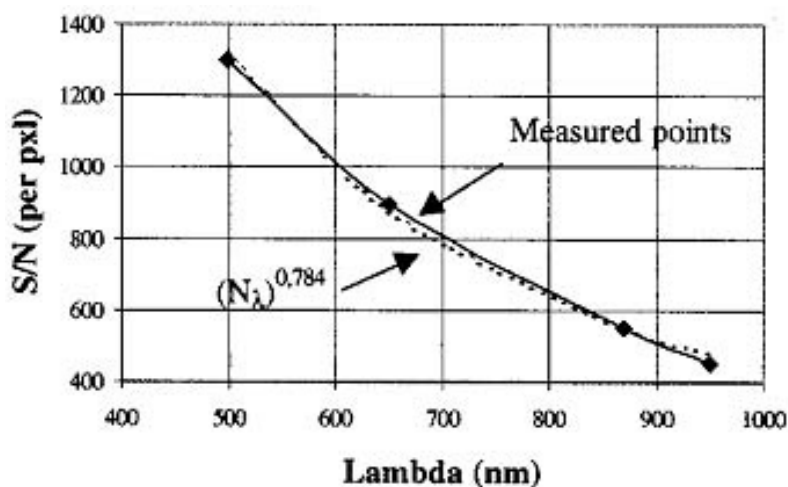


Figure 4.3: Modal noise measurements of a 70 m fibre and exponential fit by Baudrand & Walker

It should be noted that the square-root law was derived using the assumption that the speckle pattern is coherent. The finite bandwidth deployed by the Cherny-Turner spectrograph require the consideration of the visibility factor (see eq. (5.5 and 5.6)). Bandwidth and phase delay between modes depend on the wavelength and thus will influence the visibility.

The above speckle statistical consideration is based on an equal modal power distribution (MPD) in the fibre, i.e. eq. (4.2) assumes that *all* fibre modes that are allowed within Θ are equally excited. It has been found that the MPD depends on the geometry of the input illumination, with the tendency to accumulate preferentially more power in lower order modes (Wood, 1984, Saijonmaa & Halme, 1981 and Papen & Murphy, 1999).

4.3 Coherence investigations

4.3.1 Rawson et al.: Bandwidth

A theoretical paper by Rawson et al. (1980), and later in Moslehi et al. (1983), derived the correlation in the speckle pattern of two frequencies ν and $\nu + \Delta\nu$ at the fibre endface. To keep the calculation simple, the derivations assumed a planar waveguide, which is argued to be a sufficient approximation. The correlation can be expressed as a function of $\Delta\nu$:

$$\rho(\Delta\nu) = [C(y)/y]^2, \quad (4.7)$$

with C being a Fresnel integral;

$$C(y) = \int_0^y dt \cos(\pi t^2/2), \quad (4.8)$$

where y is defined as

$$y = 2L(NA)^2\Delta\nu/cn, \quad (4.9)$$

with L =fibre length, NA =numerical aperture, n =core refractive index and c =light velocity. As a first minimum occurs for $y = 1.74$, the width of the frequency correlation function (FCF) can be estimated by:

$$\Delta\nu \simeq 1.5cn/L(NA)^2. \quad (4.10)$$

This is a measure for the bandwidth at which the speckle contrast reaches a minimum. For a given source with bandwidth $\Delta\nu$ the visibility therefore decreases when the length of the fibre or the coupling angle NA is increased.

4.3.2 Kanada and Aoyama: Modal noise for partially incoherent light

The considerations in section 4.2 only hold true for coherent light. Partial incoherence in association with modal noise is taken into account by Kanada & Aoyama

(1983), dividing the pure speckle statistics expression by the visibility v , yielding;

$$S/N = \frac{1}{v} \left(\frac{S}{R} \right)_{coh}. \quad (4.11)$$

Here, the *visibility* v can be theoretically derived by taking into account the finite bandwidth of the optical source and the phase delay between modes:

$$v = \iint_{-\infty}^{\infty} dt_1 dt_2 Q(t_1) Q(t_2) \Gamma(t_1 - t_2).$$

The function $Q(t)$ is the fibre-mode density having transmission delay t to the total supported mode number and $\Gamma(t)$ is the autocorrelation function of the optical source. Both, $Q(t)$ as well as $\Gamma(t)$ are assumed to be Gaussian with a FWHM of f_c and f_s , respectively. The analytical result of this convolution integral is:

$$v = [1 + 2(f_s/f_c)^2]^{-1/2}. \quad (4.12)$$

The speckle contrast is reduced when observing light of broad bandwidth (high f_c) or for large mode delay (high f_s), i.e. for long fibres and fast coupled multi-mode fibres. An analytical estimation for v is given by eq. (5.7). Note: Fibre length dependence not observed for lengths of 10^2 , their investigation extends to 10^3 where an effect is observable.

4.3.3 Grupp: Vignetting due to overfilled grating

As Fuhrmann et al. (1997) pointed out, the FOCES spectrograph exhibits a residual noise due to fibre movement while tracking. Thus, Grupp (2003) started a direct investigation of the spectrograph for this additional noise source, where soon it turned out that its occurrence can be explained by a beam vignetting effect when overfilling the grating (transmittance 95%) in conjunction with the telescope tracking. This would cause the speckle pattern at the grating to change, eventually limiting the signal to noise to ≈ 200 .

This reminds us of the result by Goodman and Rawson (eq. (4.4)) where the noise depends on the surface area ratio ρ^2 , taking into account that part of the light is blocked between fibre endface and detector. Grupp uses a semi-analytical approach, taking speckle statistics considerations into account. Unsurprisingly, his approach

leads to a quite similar result, reported earlier by Goodman and Rawson (for $g = \rho^2$):

$$N/S = \frac{1}{\sqrt{M}} \sqrt{\frac{1-g}{g}}, \quad (4.13)$$

where M is again the number of modes supported by the fibre and g is a free parameter.

Eq. (4.13) is consistent with experimental results for longer wavelengths. Only below 500 nm do the experimental results show deviation from theory, presumably due to inaccuracies caused by low signal strength in this range (see fig. 4.4).

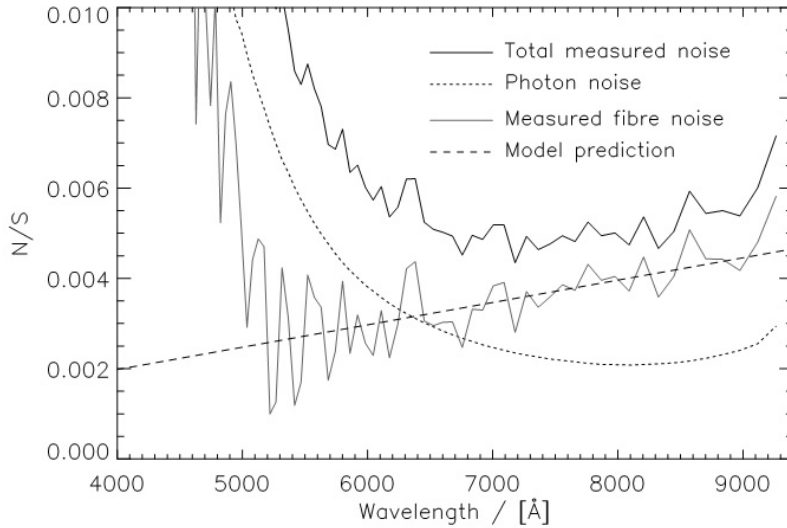


Figure 4.4: Measured and predicted noise (Grupp, 2003)

Following the Baudrand & Walker approach, Grupp tested fibre agitation as a possible cure for modal noise. He could show that with agitation periods smaller than the integration time, the modal noise can be significantly reduced to a level where the photon noise becomes dominant.

4.3.4 Corbett: Mode excitation in optical fibres

In his thesis Corbett (2006) pointed out that there are some discrepancies in the literature. He therefore investigated modal noise in relation to its parameter dependence on input focal ratio, beam truncation (ρ^2 , see section 4.2), wavelength and fibre length.

With regard to the latter parameter, as already reported by Baudrand & Walker, there is no significant length-dependence of modal noise for fiber-lengths between 1

and 45 m implying that the speckle contrast is stable over fibre length and might for instance be explained by a dominating end-effect of the fibre, see Poppett & Allington-Smith (2010). His investigations for coherent light under the application of different slit-widths to obscure the beam showed good agreement with the Goodman and Rawson result (section 4.2.2). He also notes that the limiting signal-to-noise for no beam-obscuration was at the order of $\gtrsim 10^3$ whereas the prediction reaches infinite values at that point (i.e. no modal noise). Since no other aperture was truncating the beam, the mode filtering process must be taking place somewhere else.

The investigation for the case of partially coherent light entails the study of the dependence of slit-width, focal ratio and wavelengths, showing reasonable agreement with the theoretical signal-to-noise prediction, when multiplied by a factor of 90. According to eq. (4.11) this corresponds to a visibility of ~ 0.01 .

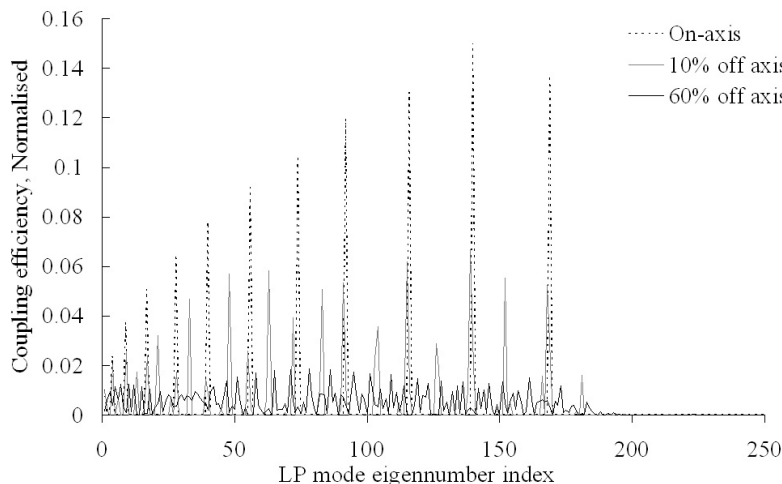


Figure 4.5: The excited modes for Airy coupling. Although the fibre has many more guiding modes, only the first modes are excited.

The power modal distribution displayed in fig. 4.5 shows mode excitation for a beam of $U_{max} = 12.2\pi$, coupling into the fibre for an a) on axis; b) 10% off-axis; c) 60% off-axis beam (in percentage of the fibre core radius.) In this simulation the intensity distribution for the near field is an airy pattern. For case a) the $l = 0$ modes predominantly experience excitation, whereas for more and more asymmetric coupling the power gets distributed among the other modes. The cut-off is by about 180 modes, corresponding to a certain f-ratio with which it is coupled into the fibre. This shows as was stated earlier in section 4.2, the modal power distribution cannot be assumed to be equal among the allowed modes. Also, only a few lower modes of

the fibre are excited depending on the input focal ration. Furthermore, significant variations in coupling strength between different modes can be noted.

To account for the uneven distribution of modes, the investigations in the later chapters are not based on M in eq. (4.2) but rather on an *effective mode number* M_{eff} , which shall take into account that higher order modes that contain less power contribute less to the overall modal-noise statistics. The situation might be more complex, but the above assumption is considered to be a sufficiently accurate approximation for now.

4.3.5 Chen et al.: The two-mode simulation

Chen et al. (2006) observed a periodic pattern with the high resolution échelle spectrograph ACES. Using mode propagation simulation for the case of a sparsely populated fibre, they were able to predict the periodicity of the pattern. The scrutiny of these mechanisms give a good overview about the processes at work:

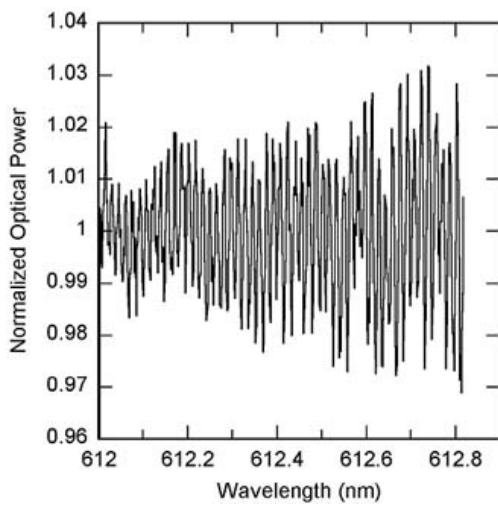
The data in fig. 4.6(a) is the ACES dispersed spectrum of a white light source, which features a periodic intensity pattern. For a more thorough understanding of this periodic pattern, it is useful to identify a speckle as the location of two modes being in phase, thus resulting in a maximum intensity. As different modes possess different propagation constants, a shift in wavelength will result in a different relative phase $\Delta\phi$. At a point where $\Delta\phi = \pi$ both modes extinguish each other. Now, with a whole field of speckles, the varying intensity distribution leads to a variation in detected intensity when a clipping aperture is present. (This mechanism becomes more clear when looking at two modes only (cf. sections 4.3.5 and 4.3.5)).

Experimental details

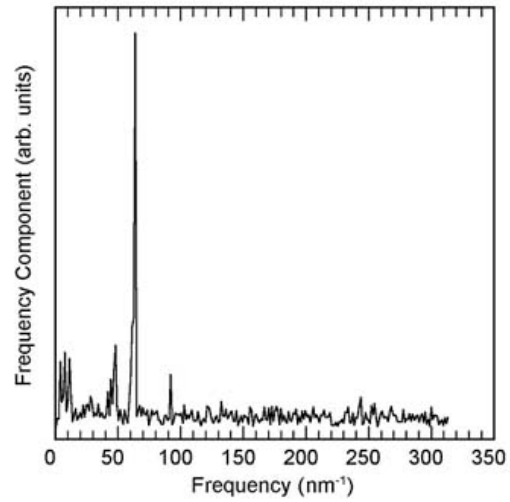
In the case of the ACES fibre-coupled échelle spectrograph it is coupled from the telescope with a IR-single mode fibre which is standard in telecommunications ($8 \mu\text{m}$ core diameter). Since they studied the optical spectrum of a white light source, the core supports very few modes (four at 841 nm, seven at 612 nm and 12 at 465 nm). The intensity variation over wavelength which could be observed had a spectral frequency of 60 nm^{-1} .

Simulation predictions

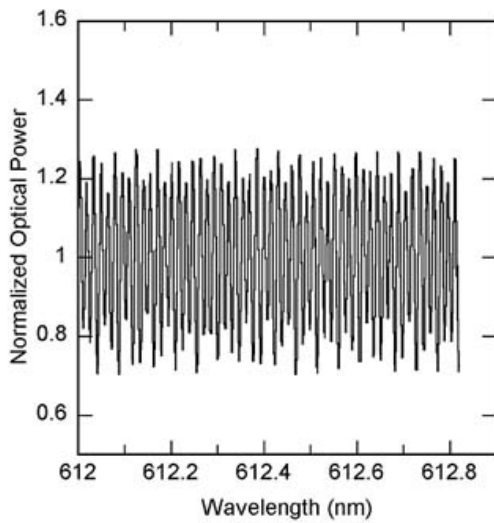
The periodic change with wavelength can be better understood when considering two modes only. Chen et al. simulated the irradiance pattern (see fig. 4.7) for each



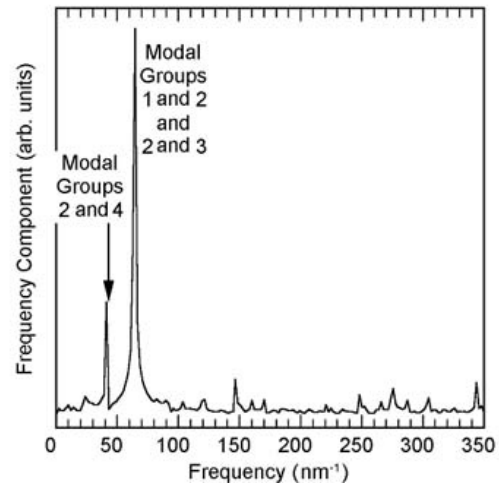
(a) Experimentally recorded spectrum after subtraction of third-order polynomial fit and renormalization.



(b) Frequency components of the experimental data of fig. 4.6(a)

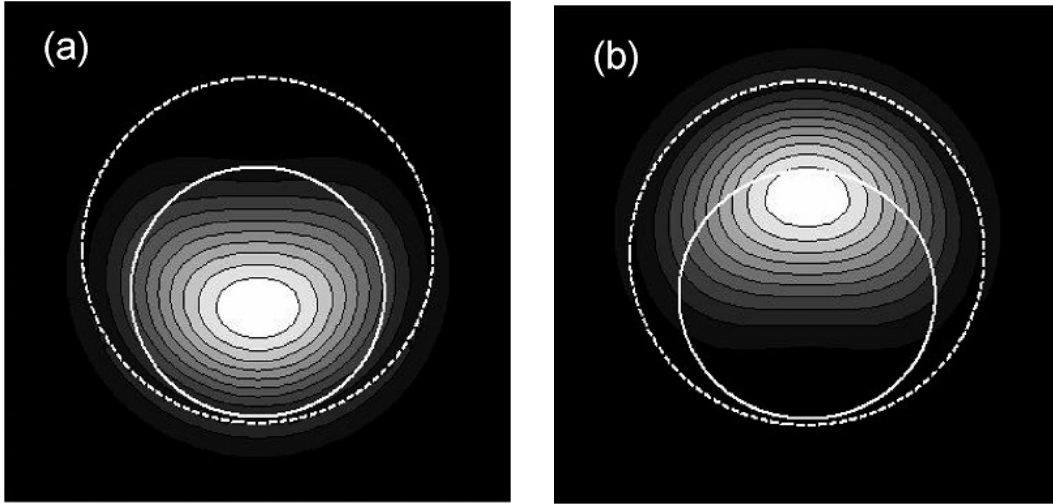


(c) Simulated spectrum



(d) Frequency components for the simulated data of fig. 4.6(c)

Figure 4.6: Comparison of experimental and theoretical data for light transmitted through an optical fibre and resolved via an échelle spectrograph with wavelengths near 612 nm. (by Chen et al., 2006)



(a) Superposition of HE_{11} and TE_{01} mode.

(b) Same as a), but with phase shift of π .

Figure 4.7: Aperture clipping of fibre end-face carrying two modes. When the relative phase between the two modes changes, integrating within the same aperture leads to different results.

wavelength, using two lower order modes, namely the HE_{11} mode (group 1, $l=0$, $m=1$) and TE_{01} mode (group 2, $l=1$, $m=1$), superposing them while taking their different propagation constants into account, using an approximation for weakly guiding fibres ($\Delta = n_{core} - n_{cl} \gtrsim 0$) as done by Gloge (1971):

$$\beta = n_{core}k (1 + \Delta - \Delta(u^2/v^2)) \quad (4.14)$$

Deriving the propagation constant like this, requires an exact knowledge of the dispersion relation for both materials - the core and the cladding of the fibre. Sellmeier coefficients up to the third order had been applied to give an approximation for the dispersions in both materials. The intensity measurement was simulated by further restricting with an aperture sized such that the contrast of the periodic pattern becomes highest. The intensity for different wavelengths was recorded, delivering comparable results to those obtained with the ACES échelle spectrograph (cf. fig. 4.6 and fig. 4.9(a)).

Analytical approach

In order to derive the oscillation period analytically, first consider the phase difference between the two modes exhibiting propagation constants β_1 and β_2 at the fibre

endface:

$$\Phi_{rel} = [\beta_1(\lambda) - \beta_2(\lambda)]. \quad (4.15)$$

At a nearby wavelength $(\lambda + \delta\lambda)$, the relative phase becomes

$$\Phi_{rel}(\lambda + \delta\lambda) = [\beta_1(\lambda + \delta\lambda) - \beta_2(\lambda + \delta\lambda)]L + \Phi_0,$$

with Φ_0 being the initial relative phase between the two modes. Thus, the relative phase $\Delta\Phi_{rel}$ shift becomes

$$\Delta\Phi_{rel} = \Phi_{rel}(\lambda + \delta\lambda) - \Phi_{rel}(\lambda) \approx \left(\frac{\partial\beta_1}{\partial\lambda} - \frac{\partial\beta_2}{\partial\lambda} \right) \delta\lambda L.$$

One oscillation period is reached when the phase shift has changed by 2π . That means the oscillation pattern has a period of

$$\delta\lambda_{period} = \frac{2\pi}{\left(\frac{\partial\beta_1}{\partial\lambda} - \frac{\partial\beta_2}{\partial\lambda} \right) L}. \quad (4.16)$$

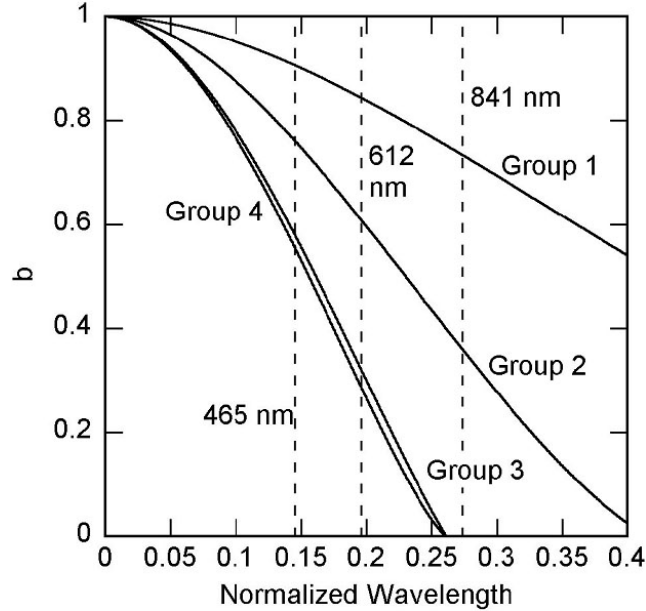


Figure 4.8: Normalized propagation constant versus normalized wavelength (by Chen et al.), the parameter b at the abscissa is defined by eq. (4.17).

Fig. 4.8 shows the normalised propagation constant b vs wavelength. This is defined

by

$$b = 1 - (U^2/V^2) = \left[\frac{\beta^2}{k^2} - n_{core}^2 \right] / (n_{cl}^2 - n_{core}^2), \quad (4.17)$$

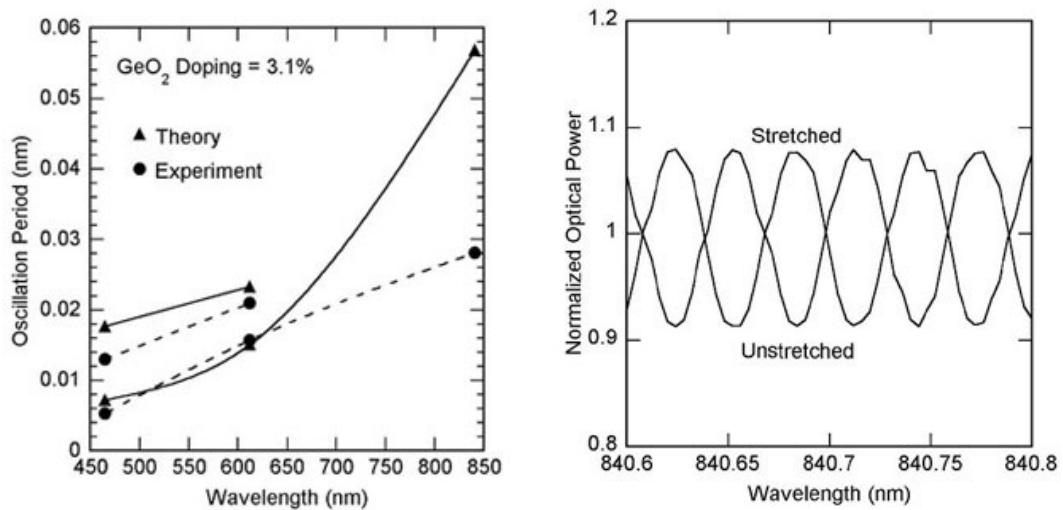
with β the propagation constant in the fibre and k the propagation constant in free space. In the last step a small refractive-index difference was assumed between core and cladding. Mode groups are set of groups with similar U (and thus $\bar{\beta}$). That means that also the derivatives of the propagation constants are only different between the groups; between members of one mode group the values are similar. An analytical derivation of the modal dispersion has been undertaken by Gloge (1971).

Eq. (4.16) suggests that modal noise is dependent on fibre-length, a relation that is only partially confirmed by experiment in a paper by Rawson et al. (1980), i.e. when the fibre is very long. However, for shorter fibres the length-dependence could not be confirmed (section 4.2.3). Therefore, the fibre length dependence of modal noise is probably not solely explicable by the decrease of speckle contrast due to increasing mode delay with increasing fibre-length (cf. section 4.3.1).

Solution for modal noise mitigation

Chen et al. (2006) realized that stretching the fibre during exposure can reduce the effect of modal noise since this shifts the oscillation pattern. Thereby the oscillation pattern has to be shifted by at least half a period to cancel out the oscillation effect (cf. fig. 4.9(b)).

In his paper Chen verified a tool to predict the periodicity of the pattern for the fibres of the ACES spectrograph. Based on the Chen results, mode field simulations and experiments were conducted using the aperture restriction approach, with the aim of predicting modal noise in a given spectrograph application. The simulations turned out to be in good agreement with experimental findings: experimental and theoretical results differ by less than a factor of two. This gives a good estimate for handling modal noise. However, because prior knowledge of the modal dispersion of the fibre is required, the application of this predictive scheme is not straightforward. If the contrast of the periodic pattern also becomes accessible, an expansion of these simulations would enable a quantified prediction of modal noise in few mode fibres. However, describing the multitude of occurring frequencies equivalent to eq. (4.16) becomes more complicated. Moreover, the model suggests fibre length dependence which is inconsistent with findings by Baudrand & Walker (2001) and Corbett (2006), section 4.2. Nevertheless, their experimental results confirm their



(a) Oscillation periods for experimental and simulated data.

(b) Simulated optical spectra for an unstretched fibre and for the fibre stretched by 0.24 mm

Figure 4.9: Oscillation periods and optical spectra (by Chen et al., 2006.)

assumptions, motivating a closer investigation in chapter 5.

4.4 Conclusions

This chapter gives a brief overview of the current status of research on the photometric accuracy imposed by fibre-modal noise. Basic mechanisms that lead to this phenomenon are known: The formation of speckles at the fibre exit, its variation due to stress and the resulting intensity fluctuation due to a mode filtering process (e.g. a restricting aperture). Two aspects are considered to be most relevant for a quantitative estimate of the related photometric noise: (i) the number of guided modes in conjunction with the area ratio of the light transmitted; and (ii) the visibility of the speckle pattern at the detector. Both aspects are only partially understood, and some of the experimental findings disagree with theoretical predictions regarding the length dependence.

In section 4.3.5 the work by Chen et al. was presented. Their experimental findings are in agreement with a two-mode model, suggesting a controlled fibre treatment to reduce the throughput variation over wavelength. In the next chapter an expansion to multimode fibres will therefore be investigated.

Chapter 5

Modal noise theory revised

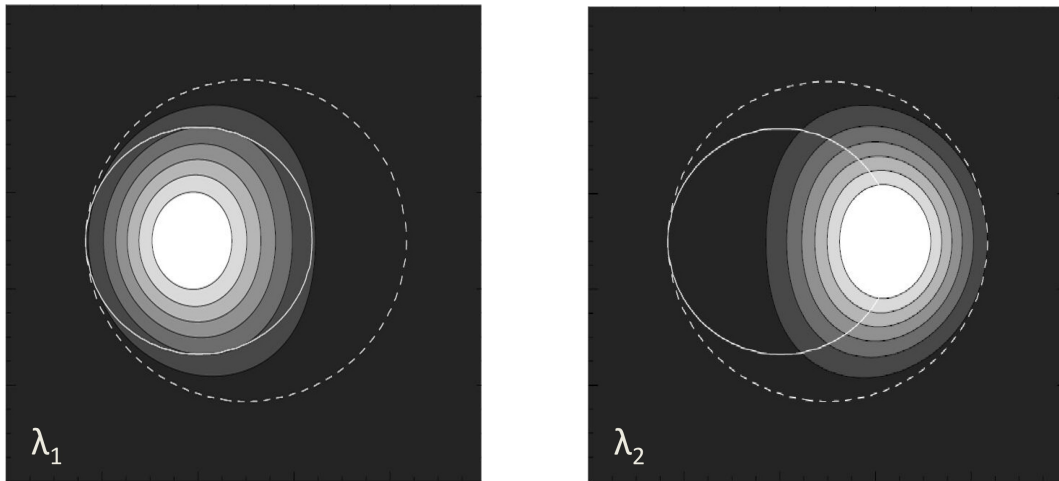
The previous chapter gave an overview of the current state of research concerning photometric uncertainties of fibre modal noise. Although it seems that quite a comprehensive picture can be drawn, published modal noise investigations still show some peculiarities, especially with regard to the noise being virtually independent of fibre length. The mode population and the visibility of the speckle pattern also remain comparatively unexplored. Moreover, it seems that the regime in which the phenomenon has been investigated is not applicable for astrophysical applications, especially where high visibilities and strong aperture clipping ($\gtrsim 30\%$) are more feasible.

For a more thorough understanding of these phenomena, the simulations conducted by Chen et al. will be extended to a larger number of modes. The importance of the visibility parameter is discussed and a method of estimating its value is provided.

5.1 Verification of the the two-mode case

As has already been shown by Chen et al. in section 4.3.5, the throughput variation for two-modes in an optical fibre, can be understood by using the mode propagation model. Simulation results by Chen et al. find support in experiment, as they were able to show that the spectrograph signature was similar to the numerical prediction. This gives hope for applying the numerical method to a larger set of modes, eventually predicting the modal noise in MMFs.

Taking a closer look into modal noise generation in the two-mode case gives a good first impression of the general modal noise phenomenon and its character-



(a) Aperture clipping with maximum throughput.

(b) Aperture clipping, minimum throughput.

Figure 5.1: Irradiance pattern of two modes guided by a fibre whose outer circumference is depicted by the dashed line. In (a) and (b), the phase difference between the two modes differs by π . With an aperture mask (solid line) introduced in the beam path, the transmission efficiency becomes dependent on the phase relation between the two modes (after Chen et al.).

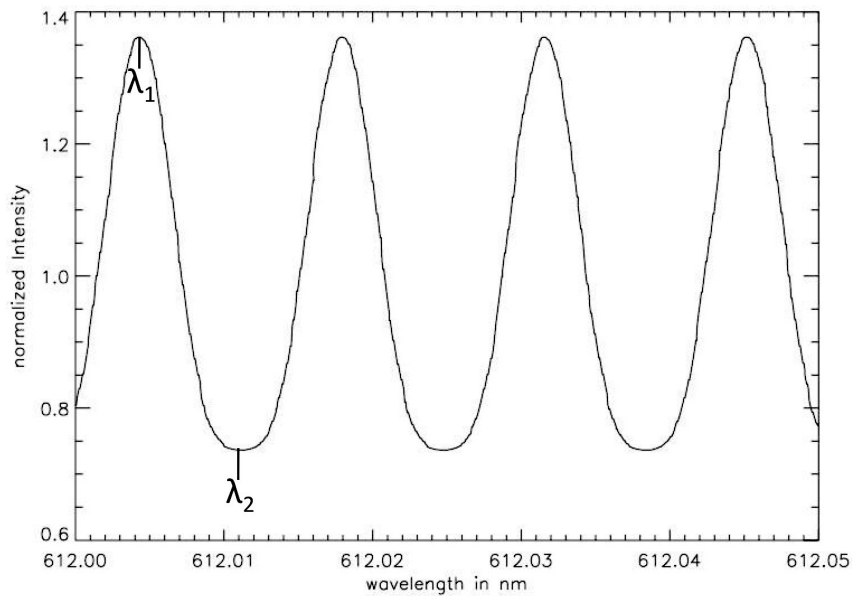


Figure 5.2: Simulations reproducing the Chen et al. result, showing normalized intensity over wavelength. The irradiance pattern combined with the aperture clipped as in fig. 5.1 causes the intensity to vary as the phase relation between the two modes changes with wavelength).

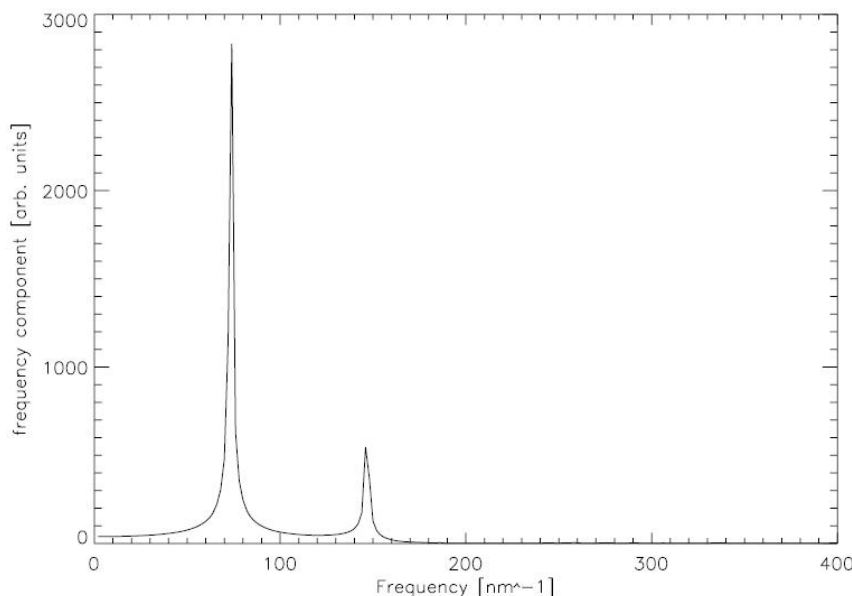


Figure 5.3: Fourier analysis of the data shown in fig. 5.2. The second frequency component is caused by the deviation from the sine function.

istics. When propagating two modes through a standard optical fibre, their relative phase shift causes the corresponding intensity pattern to change. By means of a restricting aperture this results in a variation of the throughput. Thereby, the total power of the irradiance pattern remains unchanged when integrating over the whole fibre core area (dashed line in fig. 5.1). If however, spatial or angular filtering occurs on the way from the fibre end-face to the detector, the variation in the intensity pattern leads to different transmission rates. Fig. 5.1 depicts a circular aperture clipping causing the detected intensity within the aperture to vary from maximum throughput (fig. 5.1(a)) to a minimum throughput (fig. 5.1(b)) due to the inhomogeneous and varying intensity distribution for different phase relations between the modes. Such an aperture clipping can be caused for instance by an overfilling of the grating, or truncating the fibre end surfaces by a narrow slit in order to increase the spectral resolution, also by using under-sized lens apertures.

In a first step the numerical results of the Chen et al. simulation are reproduced. Therefore, similar parameters have been used (see table 5.1), where the numerical aperture ($N.A.$) and the V -parameter are derived using eq. (3.5) and (3.16), $\Delta = (n_c - n_{cl})/n_c$ is the relative refractive index difference. The modal fields and their superposition were calculated in IDL, to then derive the corresponding intensity distribution and integrate over the restrictive aperture in the near field. The irradiance pattern in fig. 5.1 is produced by the superposition

Table 5.1: Input parameters for two-mode simulation.

Parameter	Value
Fibre core diameter	8.3 μm
λ	632.8 nm
$N.A.$	0.12
V	9.9
Fibre length, L	23 m
Refractive index difference, Δ	3.364×10^{-3}
Number of modes	2

of the two modes HE_{11} (group 1: $l=0, m=1$) and TE_{01} (group 2: $l=1, m=1$), see also table 3.2 of section 3.2.4. Investigations that study the influence of the actual size of the aperture were omitted here, the effect will merely be seen in the intensity variation from minimum to maximum. Although this is relevant for deriving the signal-to-noise ratio, the considerations are restricted to the comparability of the Chen et al. result.

The simulation assumed a fixed, random phase relation of the two modes at the fibre entrance. The modes were then propagated through the fibre according to eq. (4.14). Then the throughput was calculated when the near field experiences an obscuration by a circular aperture. The resulting throughput over wavelength is depicted in fig. 5.2. Fig. 5.3 shows the power spectrum of this oscillation, with a dominating frequency of about 70 nm^{-1} . A second frequency component at 150 nm^{-1} is probably due to the deviation from a true harmonic function. This result confirms the findings of Chen (cf. fig. 4.6(a)). Note, that for carrying out the experiment, the U - and V - parameters (compare section 3.2.2) were assumed to be constant over this small wavelength range.

One basic assumption of the modal noise investigations in this thesis is that a statistical evaluation of the intensity pattern over wavelength allows one to predict the variation in throughput when the refractive index is changed due to e.g. fibre stress. The relative phase $\Delta\Phi_{j,k}$ of two modes j and k for any given z -position of the optical fibre is given by

$$\Delta\Phi_{j,k} = (\beta_k - \beta_j)z. \quad (5.1)$$

And thus, with eq. (4.14) at the fibre end-face $z = L$:

$$\Delta\Phi_{j,k} = n_c k \Delta(U_k^2 - U_j^2)L. \quad (5.2)$$

Table 5.2: Input parameters for few-mode simulation.

Parameter	Value
Fibre core diameter	100 μm
λ	632.8 nm
<i>N.A.</i>	0.22
V	109.0
Fibre length, L	20 m
Refractive index difference, Δ	3.364×10^{-3}

This is a product of refractive index difference between core and cladding $\Delta = (n_c^2 - n_{cl}^2)/n_c$, fibre length L , reciprocal wavelength ($k = 2\pi/\lambda$) and a constant that is characteristic for the two modes under consideration, namely $(U_k^2 - U_j^2)$. In order to investigate the throughput modulation due to refractive index change, it is therefore valid to study the throughput variation given a corresponding change in wavelength. However, n_c is inaccessible for a direct measurement, so we would not know by how much the wavelength needs to be changed in order to reproduce the corresponding variation in phase. The assumption being made here is that “enough” oscillations occur during a variation n_c so that the signal to noise ratio converges to the same value.

5.2 Expansion to the few-mode case

As has been shown by Chen et al. in chapter 4 and verified in the previous section; The two-mode simulation gives comparable results to the actual signature of a real spectrograph. This is encouraging for further considerations based on mode simulations, expanding our considerations to a more complex situation where the fibre guides a few modes. The following considerations use similar parameters as in section 5.1, but with a different core size and numerical aperture to allow for higher order modes, the core size of 8.3 μm in the two-mode case was limiting the number of modes to eight and is here expanded to 100 μm . Instead of a circular aperture a slit has been deployed to mock beam obscuration due to a slit-mask at the spectrograph entrance.

The simulation assumes even power distribution between all modes that are excited at $U < 10$. As discussed earlier in section 4.2, this assumption is rather arbitrary as the modal power distribution (*MPD*) depends on how the light is coupled into the fibre, therefore these results should be seen as preliminary. Furthermore, the phase

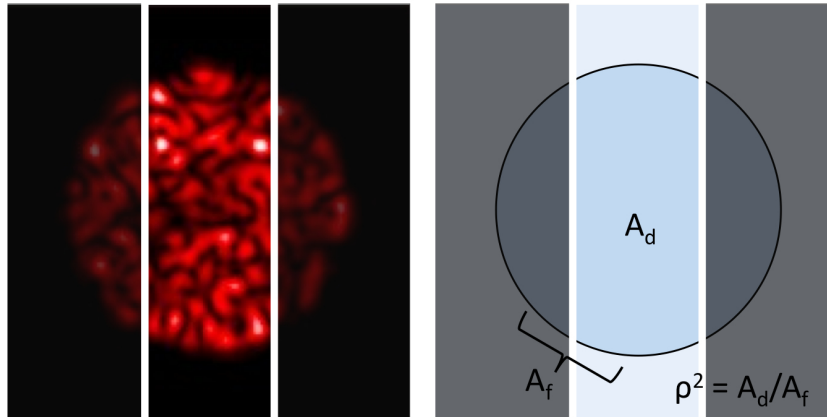


Figure 5.4: Modal noise originates from truncating the beam of an inhomogeneous, time-varying intensity distribution. The essential geometrical variable ρ^2 is defined by two parameters; A_f is the area of the fibre image, whereas A_d is the part of the illuminated area that is detected.

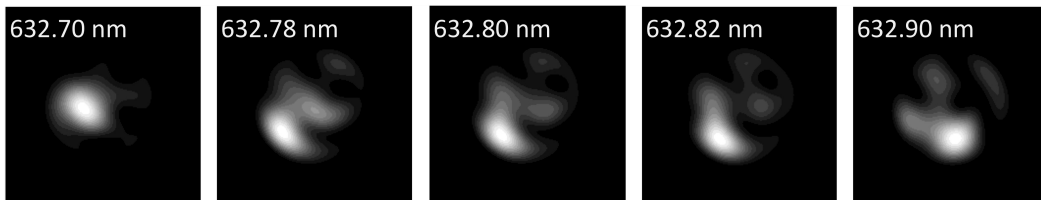


Figure 5.5: Simulated modal pattern upon which fig. 5.6 is based.

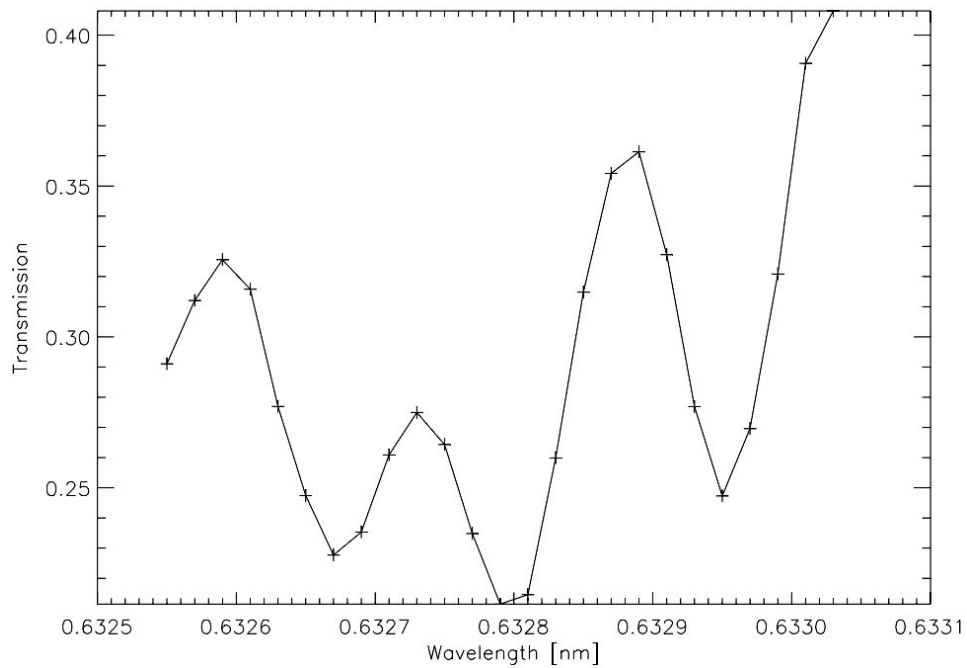


Figure 5.6: Throughput variation for the few mode case.

relation between the modes is fixed at the fibre entrance, the initial values created by a random number generator. The shift in the speckle pattern for successive wavelengths then results from applying eq. (4.15) to calculate the phase relation at the fibre output. Fig. 5.6 shows the intensity variation due to an aperture mask for a 100 μm core-diameter fibre, guiding 10 modes. For the throughput determination the fibre end-face has been truncated as shown in fig. 5.4, with a slit width of 1/10 of the fibre-core diameter.

In section 4.2.1 the work by Daino et al. was presented, stating that the number of guided modes would be equal to the number of speckles – contrary to this the modal pattern in fig. 5.5 does not feature 10 speckles but only four to five at the most, the simulation result might therefore differ from the predicted value. From the intensity variation in fig. 5.6 the SNR can be derived by dividing the mean transmission rate by its standard deviation, yielding

$$SNR_{sim} = \frac{I_{mean}}{\sigma_I} = 5.5,$$

where I_{mean} and $\sigma_I^2 = \frac{1}{N-1} \sum (I_i - I_{mean})^2$ are the mean value and the standard deviation of the data set, respectively. It has to be said that the calculated SNR can vary with the chosen sampling rate and the wavelength regime considered, obtaining values as low as 3.5 and going up to 6.4.

The expected value according to eq. (4.4) is with $M = 10$ and $\rho^2 = 0.93$

$$SNR_{th} = \rho \sqrt{\frac{M+1}{1-\rho^2}} = 8.3.$$

Both values, SNR_{sim} and SNR_{th} are at the same order of magnitude, but with SNR_{sim} slightly lower than the corresponding theoretical prediction. The underlying basic assumption for all predictions here being made is that the throughput variation is Gaussian-distributed. This is not necessarily the case in the few-mode regime when sampling a limited wavelength range with a limited sampling rate. The wavelength range was therefore expanded and sampling refined (up to 100 wavelengths sampled with distance 0.01 nm), but the results did not show any convergence.

Note that the error bars in fig. 5.7 are omitted. This is for two reasons: 1) The time required for performing the simulation is very long; 2) The data in each point

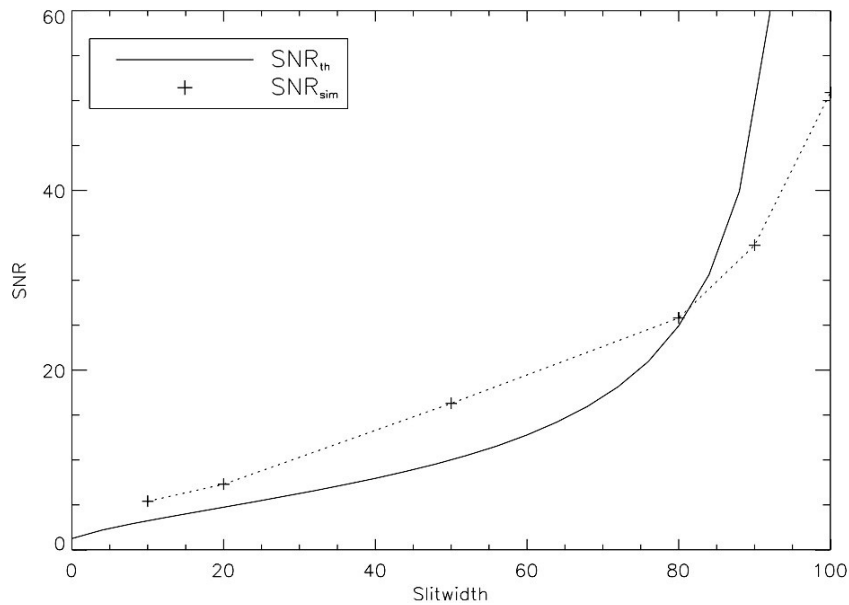


Figure 5.7: The SNR for different slit-widths for a 100 μm fibre (100 μm corresponds to no beam-truncation) and 60 modes, sampled for 60 data points (12 \AA). The theoretical curve is derived using eq. (4.4). The Simulation is well approximated by the theory, although for larger slit-sizes the theory does not take the intensity at the edge of the fibre into account and therefore shows too high SNR .

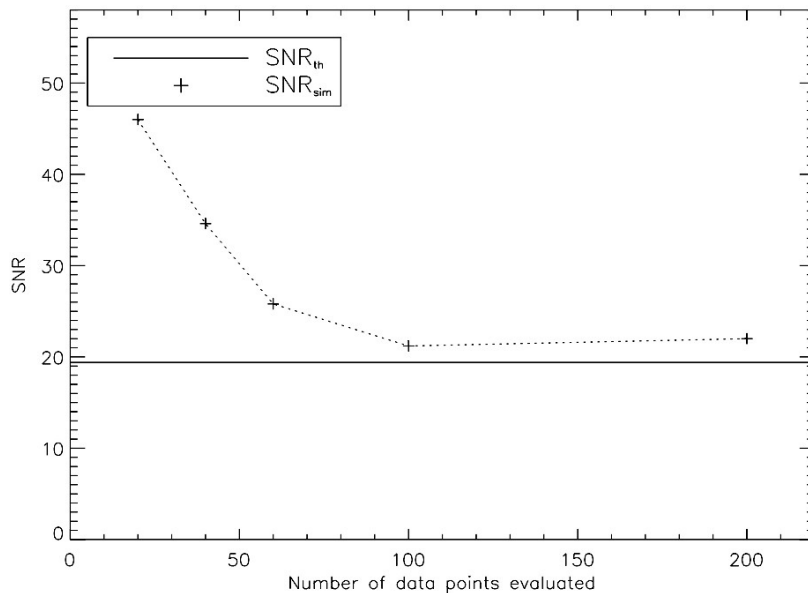


Figure 5.8: Depending on the number of wavelengths sampled, the SNR can take on different values. For the 80 μm slit and 60 modes the theoretical value (eq. (4.4)) is approached after sampling about 100 wavelengths over 20 \AA .

is already derived from multiple speckle patterns, so that it was not expected to obtain any different value for e.g. simulation with different phase relations between each mode.

There are many possible reasons why the SNR for the simulations is higher than the theoretically expected value: It was observed that the SNR_{sim} varies with the spectral sampling rate, as well as with the width of the selected wavelength range. Ideally, the sampling rate and the spectral width would be high enough to converge, but needs to be compromised due to the consideration that the simulation is time consuming. Furthermore, the transmission variation might not be Gaussian distributed, and in addition, a speckle size that is at the order of the slit-width may cause a different functional behaviour than eq. (4.4) suggests, see fig. 5.7. The slit samples the local intensity distribution of one or a few speckles rather than over a large sample of speckles with normally distributed intensity. Furthermore, as can be shown for a strongly periodic pattern, randomly picked intensity values are not Gaussian-distributed: Hence the error-statistic does not apply. This in fact could pose another possible reason why the simulation deviates from the theoretical prediction. However, adding more modes to the investigation should alleviate this problem due to the central limit theorem (see Rice, 1997).

In order to test the latter hypothesis, the influence of the number of excited modes was investigated. In a first step it was tested what sampling is required to obtain stable results. Fig. 5.7 suggests that the SNR_{sim} for 60 modes converged with the theoretical value at a sampling of 100 data points sampled with 0.02 nm. It is expected that for a high number of modes ($\gg 100$) would need yet finer sampling of < 0.02 nm, using excessive computing time and is therefore not pursued here.

To furthermore investigate the hypothesis concerning deviations in the error statistics are caused by the speckle size being at the order of the slit-width, the occurrence of throughput intensities was compared for different slit-widths and mode numbers. Fig. 5.9 displays the results for different slit-widths and different number of modes for 120 data points in the wavelength sample. The Gaussian error statistic can be applied when the scattering of the throughput value around its mean resembles a Gaussian distribution. The goodness of fit to the Gaussian is measured using the reduced χ^2 -test. For a 10 μm slit the intensity distribution follows a Gaussian law, whereas for 80 μm -slit the Gaussian model is not a good fit. Thereby, the number of modes does not seem to have a significant influence. The slit-width on the other hand seems to be very important. For a 80 μm slit the Gaussian distribution is a poor approximation whereas the χ^2 for the 10 μm achieves values around 1.0, as expected for a good model fit.

With increasing number of wavelengths sampled, the simulation result converges

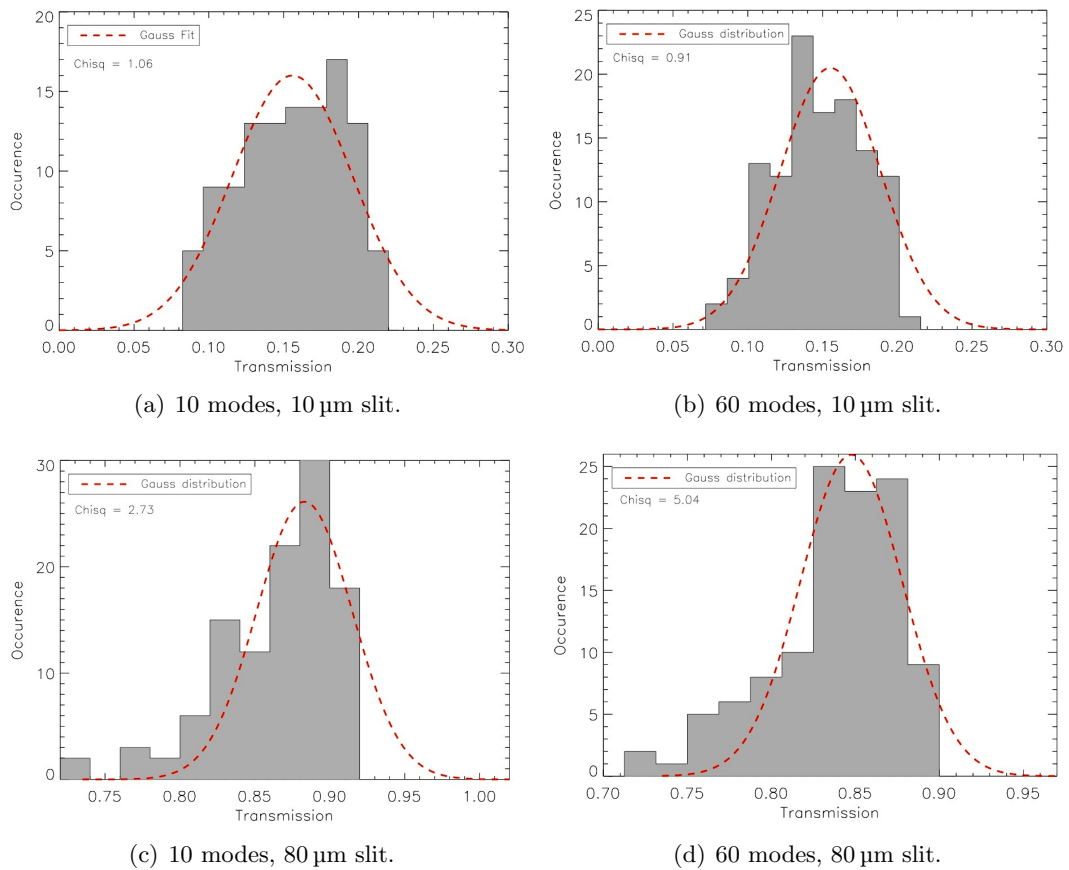


Figure 5.9: Occurrence of throughput intensity for 100textmum fibre, 120 sampled wave-lengths, different numbers of modes and selected slit-widths. For 60 modes and a 10 μm -slit, the distribution is similar to a Gaussian distribution, and the error law applies. The corresponding 10-mode-case does not resemble a Gaussian function. The distributions for the 80 μm slit are Gauss-like, indicating that the error propagation law is a good approximation.

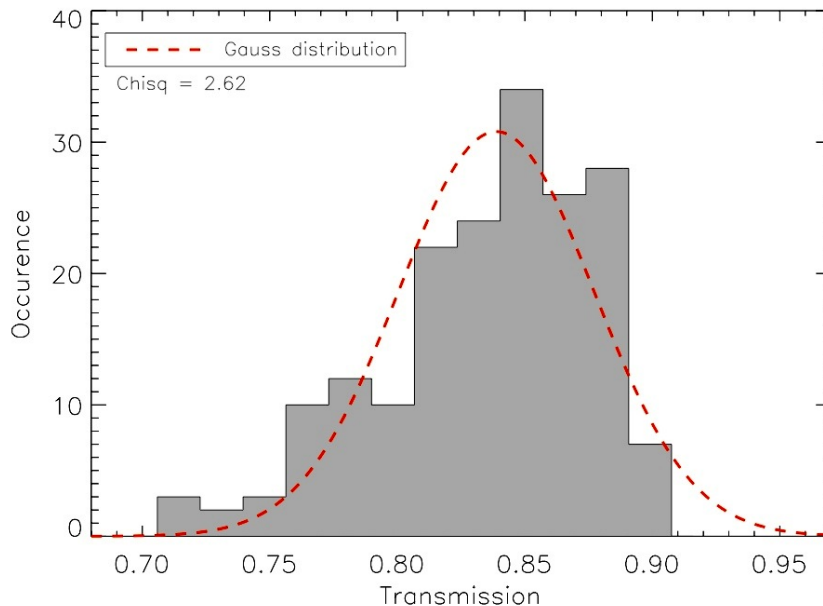


Figure 5.10: Same as fig. 5.9, but 200 data points and 80um slit, 60 modes.

against its theoretical value (fig. 5.8). A comparison between fig. 5.9(d) with fig. 5.10 implies that the Gaussian model is better approached with increased number of points sampled.

At this stage it should be emphasized that the applicability of the Gaussian distribution is essential for the considerations being made above; only then the classic error propagation law can be used (i.e. eq. (4.3) applies) and the error is symmetric around the expected value.

In summary, the modal noise law according to eq. (4.4), (Goodman & Rawson, 1981) for the coherent regime can be reproduced if the slit is narrow enough and the number of sampled data points is high enough. Simulations are very valuable to estimate the effect of few-mode fibres ($\lesssim 20$ modes) on the photometric accuracy, although it has to be noted that the resulting error statistic is no longer Gaussian for strong beam truncation and the error-propagation law (see eq. (4.3)) is not strictly valid. When simulating the noise formation for 60 modes the wavelength range had to be chosen sufficiently large (here 6 \AA) to guarantee the applicability of the error-propagation law.

When the slit width is similar to the fibre core size, the theory predicts infinite SNR. However, due to the intensity being continuous at the edge of the fibre, a small fraction of the signal will be still outside of the limits of the fibre core and thus truncated by the slit. Thus, simulation as well as real spectrograph applications will

always show a certain amount of modal noise.

It should also be noted that the investigations in this chapter so far only considered the fully coherent case. The decreased contrast due to the limited resolving power of the spectrograph is an important factor which has to be taken into account. The following section will therefore focus on the limited coherence that occurs in a fibre-spectrograph.

5.3 Visibility estimation

As could be seen from the previous section, mode simulation can reproduce theoretical results, but meets restrictions as simulations soon grow too complex, especially for fibres guiding a high number of modes. Although valuable conclusions can be drawn for the few-mode case, namely that the error statistic is only valid under certain conditions, currently there is no methodology available that predicts the visibility in the required regime. Before experimentally investigating the modal noise phenomenon, a strategy to estimate the visibility will be provided.

The *SNR* according to Goodman & Rawson (1981) is

$$SNR_{coh} = \rho \sqrt{\frac{M+1}{1-\rho^2}}, \quad (5.3)$$

where the truncation described by ρ^2 does not necessarily need to be generated by a slit at the spectrograph entrance, but also by overfilling the grating or any other spatially filtering process (e.g. inhomogeneous sensitivity of the CCD) at any position along the optical path (e.g. pupil or image plane). The subscript *coh* indicates that the coherent case is considered here. The question of how many modes are excited is not trivial. Although the mode volume M from eq. (3.25) for a given input illumination can be directly calculated (see e.g. Hill et al., 1980) from the fibre core radius a , wave number $k = 2\pi/\lambda$ and angle θ_{in} of the light cone feeding into the fibre

$$M = \frac{1}{2} (ak\theta_{in})^2, \quad (5.4)$$

this is only an upper limit. M very much depends on the fibre-launch geometry (axis-offset, angle), as was asserted by Corbett et al. (2007).

However, these considerations only hold true for coherent light. The speckle contrast is reduced when observing light of broad bandwidth and studying a large set of fibre

modes, as is the case for fast coupled multimode fibres. Then the fibre is populated by a large number of modes, resulting in a broad range of propagation constants. This is taken into account by Kanada & Aoyama (1983), dividing the pure speckle statistics expression by the visibility v , yielding

$$SNR = \frac{1}{v} SNR_{coh}. \quad (5.5)$$

Here v can be theoretically derived by taking into account the finite bandwidth of the optical source (f_c) and the phase delay between modes (considered by the parameter f_s):

$$v_{th} = [1 + 2(f_s/f_c)^2]^{-1/2}. \quad (5.6)$$

The bandwidth f_c can be estimated as follows: Assuming a light cone of focal ratio $F = 1/2\theta$ is coupled into the fibre, the difference in propagation constant between on-axis rays (β_0) and rays coupled with the angle θ (propagation constant β) is given by

$$\Delta\beta = \beta_0 - \beta = \beta_0 - \beta_0 \sqrt{1 - \theta^2/n_c^2} \approx \frac{1}{2} \frac{\theta^2}{n_c^2} \beta_0 = \frac{1}{2} \frac{\theta^2}{n_c^2} \frac{2\pi\nu}{c/n_c},$$

where n_c is the core refractive index, c the speed of light in vacuum and ν is the frequency of the electromagnetic wave. $\beta_0 = 2\pi\nu/(c/n_c)$ has been used.

The time taken for a mode to travel the whole fibre length L is given by $t = \beta L/2\pi\nu$. Accordingly, the time delay between on-axis and off-axis rays (launched at θ) is then $\Delta t = \Delta\beta L/2\pi\nu$. Identifying this time delay with f_c^{-1} yields

$$f_c = \frac{2\pi\nu}{\Delta\beta L} = \frac{2n_c c}{L\theta^2}.$$

An estimation for f_s is derived as follows;

$$f_s = \nu_1 - \nu_2 \approx \frac{\nu_c}{R} = \frac{c}{R\lambda_c},$$

Where ν_c and λ_c are the central frequency and the central wavelength of the spectral

resolution element with width $\Delta\nu = \nu_1 - \nu_2$. Hence,

$$f_s/f_c = \frac{L\theta^2}{2n_cR\lambda}$$

can be substituted in eq. (5.6), yielding

$$v_{th} = \left[1 + 2 \left(\frac{L\theta^2}{2n_cR\lambda} \right)^2 \right]^{-1/2}. \quad (5.7)$$

These are simplified assumptions, because skew rays are not taken into consideration. Thus, this model is not expected to be fully consistent with the experimental results, but they should serve as a preliminary theoretical framework. For instance it was shown by Baudrand & Walker (2001); Corbett (2006), that the *SNR* has no significant dependence on fibre length for $L \leq 100$ m. This is possibly because the fibre does not terminate with a perfect glass-air interface. This so called *end-effect* (Poppett & Allington-Smith, 2010) may lead to a stronger mode mixing and thus less coherence between the modes, which would explain the diminished visibility. In the following, L will therefore be treated as a free parameter. Thus, v remains a function of θ , n_c , R , λ , although the focus will remain here on θ and R only. Investigating the functional relation of n_c does not seem feasible and λ is omitted and should be object of further investigations in a future work-package.

In the limit of low visibilities it applies that $(L\theta^2)/(2n_cR\lambda_c) \gg 1$, so that eq. (5.7) can be approximated by

$$v_{th} \propto \theta^{-2}s^{-1}, \quad (5.8)$$

where R is assumed to be inverse proportional to the slit width s . From the experimental investigations it can be deduced that this approximation is fulfilled for the θ -case and fulfilled at least by trend for s , whereas the full dependence of visibility on the spectrograph resolving power R will remain a subject for further investigations.

A full theoretical picture of the effects involved requires understanding phenomena like intermodal coupling, modal filtering and spatial mode distribution. Therefore, it is necessary that models with the objective of modal noise prediction are grounded in experimental results first.

From eq. (5.5) it can be asserted (and later experimentally verified), that modal noise can be described as the product of two independent parameters; a visibility and a coherent term. Hence, it can be separated into two sub-problems: The coherent

speckle term is well understood taking the geometry of the fibre end-face restricting aperture into account, whereas visibility is mainly dependent on resolving power but also on the slit width. In order to verify this assertion, both values, modal noise and visibility are experimentally investigated in chapter 6.

5.4 Conclusions

This chapter is based on the current state of research as reflected in chapter 4. Following on from the two-mode simulations conducted by Chen et al., their results have been verified numerically and the calculations were extended to the few mode case.

Despite some initial success for simulating throughput variation for strong beam obscuration and fibres guiding only very few modes, proceeding to a larger number of modes (≈ 50) and weak obscuration the variation becomes inconsistent with the assumption of a Gaussian distribution. These results can be probably improved when using a finer sampling and a larger wavelength range, a trend which shows that a full SNR-simulation of multi-mode fibres becomes unfeasible because of the exponentially growing effort that is involved. However, these statistical interrelations need to be proved.

Furthermore, the modal power distribution as well as the visibility of the speckle pattern are parameters that are not sufficiently explored yet, showing the necessity for experimental investigations which will be conducted in the next chapter.

Chapter 6

Experimental investigations on modal noise

In order to attain a predictive model a dual approach has to be pursued that brings the theoretical assumptions of the previous chapter in line with the experiment. Therefore, a test-bench spectrograph was built. With the data obtained it can be shown that the task of modal noise prediction reduces to the prediction of the visibility of the speckle pattern. The functional dependence of the visibility on essential spectrograph parameters well reflects the theoretical assumptions as stated earlier in chapter 4.

This chapter first gives a detailed description of the spectrograph test bench that was used for modal noise and related investigations. Then, the data-analysis steps are presented in order to extract the modal noise and visibility from the raw data. The results are presented and a careful analysis reveals that the coherent part of the SNR -relation can be regarded as trivial. Therefore, further work concentrated on predicting the visibility. Finally, an outline is given describing how the visibility could be predicted by simulations.

6.1 Details of the experimental setup

Fig. 6.1 and fig. 6.2 show the setup used for experimental investigations that are discussed throughout the following chapters. It closely replicates the scheme proposed by Corbett (2006). The fibre-optic test-bench consists of a power stabilized halogen

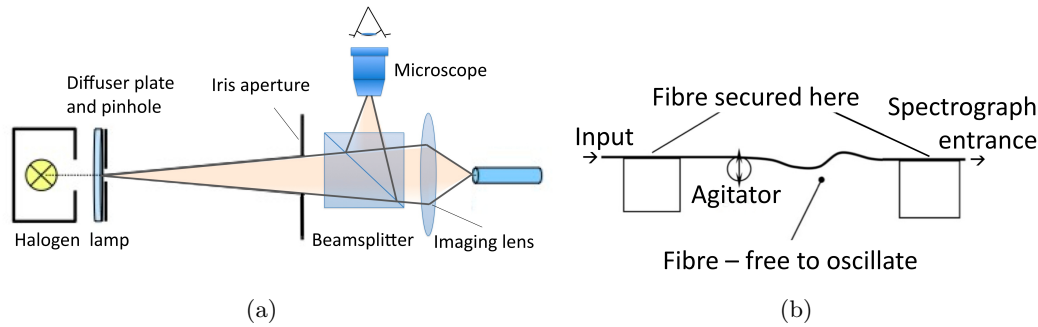


Figure 6.1: (a) Fibre input: The focus position can be controlled with the aid of a microscope in order to obtain optimal fibre illumination; (b) Fibre agitation scheme: The fibre is fixed at two points with a large free length in between. An agitator is used to produce large deflections in this region.

lamp which can be exchanged for a coherent HeNe-laser source, fibre coupling, loud-speaker voice coil for fibre agitation and a spectrograph featuring a blazed grating in Echelle-configuration. The mid to high resolution spectra (up to $R = 100\,000$) were recorded using a commercial astronomical CCD-camera (Atik 314L+).

Fibre input (fig. 6.1(a)); The test fibre is illuminated using a power stabilized halogen lamp behind a diffuser plate and a $500\ \mu\text{m}$ pinhole. The lens system demagnifies the spot to a image size of $80 - 90\ \mu\text{m}$ at the fibre input plane. An iris is used to stop the beam down in order to control the input focal ratio F . Focal ratios $F = 2.6, 3.9, 6.5$ and 13.2 were used, but by default $F = 3.9$ if not stated otherwise. The low focal ratio of 3.9 is intended to mimic astronomical devices where the fibre is fed with a fast beam to minimize focal ratio degradation (FRD, e.g. Ramsey, 1988), an effect causing the output focal ratio F_{out} to be generally smaller than the input focal ratio. Note that the focal ratio notation (F or $f/\#$) is applied here (and widely in optics literature) whereas often the half-angle of the cone of light that enters or exits the fibre $\theta = \arctan(1/2F)$ is used in order to present the functional dependencies more clearly.

Care has been taken that the fibre core is fully illuminated. Choosing a significantly smaller spot-size results in poor radial scrambling (see section 7). This causes a dominant intensity variation in cross-dispersion direction of the spectrum (see fig. 6.6). This pattern is dependent on the position of the input spot, and should therefore be avoided in order to exclude any variability in the spectral pattern during measurements. Hence, a larger spot-size ($\approx 70\%$ of the fibre-size) is chosen which results in a more homogeneous intensity pattern. A microscope is used to view the lateral position and the focus position of the pinhole image on the fibre core.

The beamsplitter is specified as "broadband non-polarizing" by manufacturer's spec-

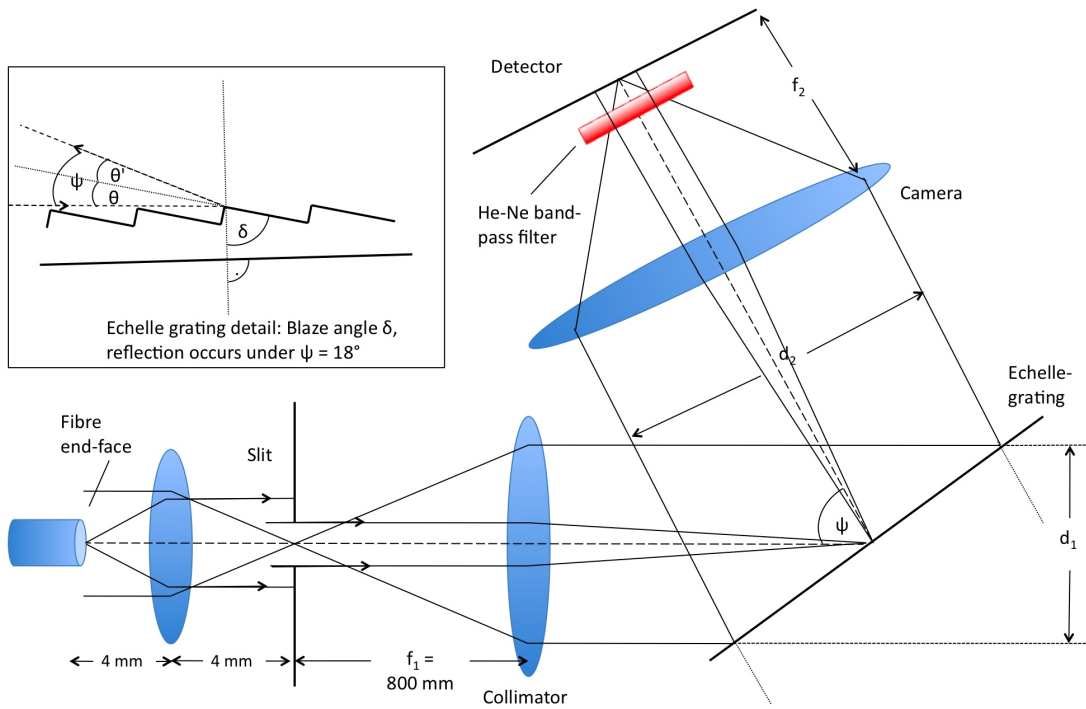


Figure 6.2: Schematic depiction of the Echelle spectrograph used for experimental investigations. The fibre far-field is imaged onto the slit plane which coincides with the spectrograph entrance. High efficiency is achieved by using the Echelle grating in Blaze configuration. Light is filtered through a narrow bandpass filter to avoid spectra overlapping at the CCD. Slit and 4 mm lens are not to scale, grating angle exaggerated. Parameters used in the text: α - incident angle, β - diffraction angle, $\theta = \theta'$ - angle of specular reflection, ψ - angle enclosed by grating reflection, δ - Blaze angle, s slit width, $f_{1,2}$ - collimator and camera focal length, $d_{1,2}$ - beam diameter at collimator/ camera, W - length of the intersection of the grating plane with the beam.

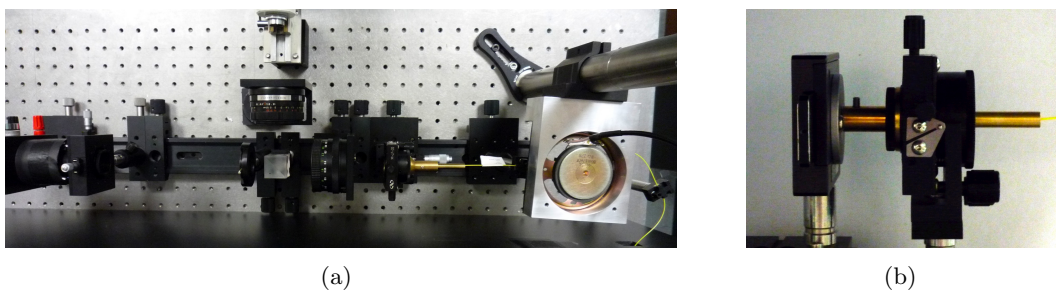


Figure 6.3: Fibre input (a) and slit-unit (b).



Figure 6.4: The spectrograph test-bench used for experimental investigations. For reasons of measurement stability the entire setup is enclosed by a light tight box (the metal frame supporting the structure can be seen on the picture).

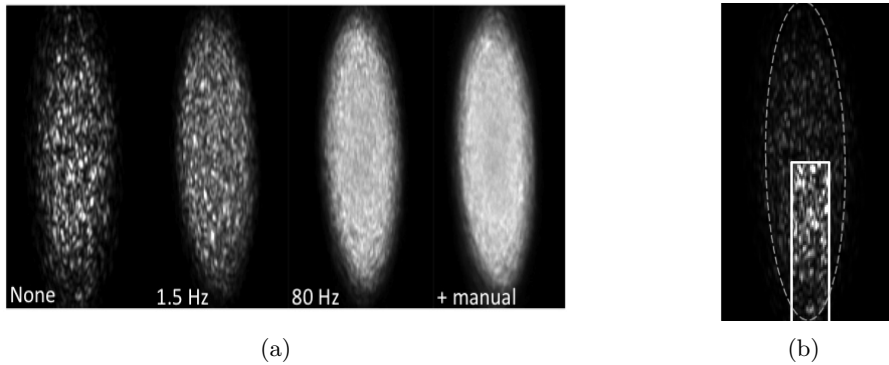


Figure 6.5: (a) Re-imaged at the CCD is the fibre far-field as it occurs at the slit plane at the spectrograph entrance when the fibre-input is illuminated with laser light. Shown are the far-fields (slit removed) at different strengths of fibre-agitation (from left to right): No agitation; agitation 1.5 Hz; agitation 80 Hz; additional manual agitation. Exposure time was 3 s. (b) The fibre (far field) image can be truncated by a slit only as in fig. 5.4 or by additional apertures that truncate the beam in cross-dispersion direction, e.g. when restricting the slit-aperture accordingly (as in section 6.3.1) or when overfilling the dispersive grating.

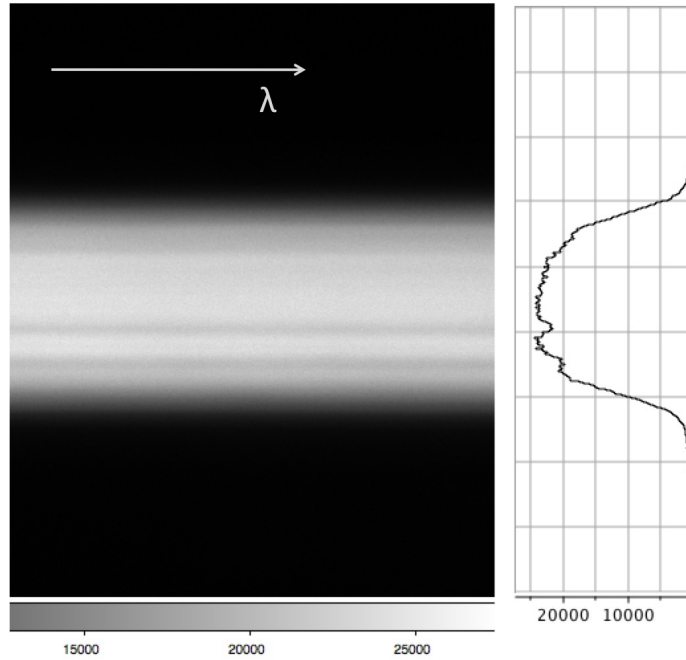


Figure 6.6: Intensity pattern of raw data. The structure that occurs at the detector plane (fibre far-field) is dominated by a variation in cross-dispersion direction which is believed to be caused by incomplete radial scrambling of the input illumination.

ifications. Examining the beam at the fibre launch, it was shown that the beamsplitter is non-polarizing for the wavelength range under investigation. Utilizing a polarizing sheet before the beamsplitter, a polarization signal could not be detected beyond the detector noise, the beamsplitter was thus found to be non-polarizing (less than 10% polarization for unpolarized input light).

Fibre agitation and slit unit (fig. 6.1(b) and fig. 6.2); After the fibre input, the fibre is attached to a loudspeaker allowing the fibre to be agitated (for flat-field image acquisition, see section 6.2.1). The agitation procedure can be understood as applying time-varying stress to the fibre. This causes the refractive index in the fibre to change accordingly, inducing a variation in the speckle pattern at the output. For integration times \gg the period of agitation, the recorded image is a pattern that (ideally) does not contain any modal information.

In order to obtain the most efficient agitation, the fibre is secured at two points where the second is at a larger distance from the point of agitation (see fig. 6.1). This allows the fibre to oscillate around its point of rest at this end. It seems reasonable that a large deflection changes the fibre properties by a larger amount, the distance is adjusted to the frequency at which it produces standing waves. An agitation frequency of 80 Hz (fig. 6.5(a)) can be shown to give the best results (lowest

SNR is measured in the respective exposures), and the modal pattern achieves a low contrast. Operating the agitation device at higher frequencies does not visibly improve the contrast, nor could a significant change in SNR be observed. From laser exposures it appears that additional manual agitation would improve the result, but again no difference for the SNR -value could be measured.

The fibre end-face is placed behind a lens with focal length $f_0 = 4$ mm, imaging the fibre far-field on the slit plane where the slit holder can carry slits of widths 50, 100, 200 or 500 μm , to obtain the spectral resolving powers as documented in table 6.2. Note that placing a slit at that plane causes beam vignetting so that $\rho^2 < 1$, thus inducing modal noise (cf. eq. (5.3)).

The ρ^2 -values are derived from the different slit sizes restricting the beam at the spectrograph entrance (compare fig. 5.4):

$$\rho^2 = \frac{A_d}{A_f} \approx \frac{sD}{(\pi/4)D^2} = \frac{4s}{\pi D} = \frac{4s}{\pi f_0/F_{out}} \quad (6.1)$$

where in the second step the approximation $A_d \approx sD$ has been used. With slit width s , diameter of the far field image D , and $f_0 = 4$ mm (focal length of the lens imaging the fibre far-field onto the spectrograph entrance slit). The input focal ratio is $F_{in} = 3.9$. Due to FRD the corresponding output focal ratio F_{out} is 3.5. With eq. (6.1) the available slit-widths 0.1, 0.2, 0.25 and 0.5 mm thus correspond to $\rho^2 = 0.1, 0.2, 0.25$ and 0.5 , respectively ($\rho^2 = 0.05$ and 0.15 are realized by restricting the 0.1 mm and the 0.2 mm slit in cross-dispersion direction, see fig. 6.5(b)). The other input/output focal ratios are treated similarly.

Table 6.1: Grating specifications and setup dimensions for the different resolving powers used for the experiment.

Grating, Newport (Richardson) Part no. 53-025 -453E

Blaze angle	$\delta = 71.5^\circ$ (R2.9)
Groove density	31.6 mm^{-1}
Enclosed angle	$\psi = 18^\circ$

F_{in}	f_1 [mm]	d_1 [mm]	W [mm]	d_2 [mm]	f_2 [mm]
3.9	800	20	120	122	800
3.9	300	7.5	45	46	400

Echelle spectrograph (fig. 6.2); Image and pupil planes are situated in the focal planes of the imaging lenses, this has the advantage of homogeneous illumination of the grating, minimizing aberrations and allowing for stray light filtering. Using

a lens with focal length $f_1 = 800$ mm ($f_1 = 300$ mm for lower resolution), the fibre end-face is re-imaged onto the Echelle grating. The blazed Echelle grating (Blaze angle $\delta = 71.9$) is used in quasi-Littrow configuration, with angle $\psi = 18^\circ$ between input and output beam. A second lens of focal length $f_2 = 800$ mm ($f_2 = 400$ mm for lower resolution, see table 6.1) images the slit-restricted fibre far field onto the CCD. In order to capture the spectra, an Atik Instruments 314L+ camera was used. A narrow band filter (HeNe, 632.8 ± 3.0 nm) is placed directly in front of the CCD to make sure that spectra of adjacent orders would not overlap. In addition, the slit-unit and spectrograph are placed in a light-tight box to keep the background signal low and air currents to a minimum.

6.1.1 Spectral resolving power

The theoretical resolving power for an échelle spectrograph can be derived as follows. Starting from the grating equation

$$m\rho\lambda = \sin \alpha + \sin \beta; \quad (6.2)$$

the angular and linear dispersion can be derived:

$$\begin{aligned} \frac{d\lambda}{d\beta} &= \frac{\cos \beta}{m\rho} \\ \frac{d\lambda}{dx} &= \frac{\cos \beta}{m\rho f_2}, \end{aligned} \quad (6.3)$$

The parameters are explained in fig. 6.2; α - incident angle, β - diffraction angle, $\theta = \theta'$ - angle of specular reflection, ψ - angle enclosed by grating reflection, δ - Blaze angle, s slit width, $f_{1,2}$ - collimator and camera focal length, $d_{1,2}$ - beam diameter at collimator/ camera, W - length of the intersection of the grating plane with the beam.

If the slit-width s is large enough, the system's resolving power is limited by the slit rather than the diffraction limit due to the ruling density of the grating. Then the spectral resolution is defined by s' the slit width as projected on the detector plane:

$$\delta\lambda = \frac{d\lambda}{dx} s' = \frac{\cos \beta}{m\rho f_2} s' = \frac{\cos \beta}{m\rho f_2} \frac{F_2}{F_1} s = \frac{s}{m\rho F_1 W}, \quad (6.4)$$

where $d\lambda/dx$ is the spectral dispersion, F_1 and F_2 are the focal ratios of collimator and camera, respectively. With $s' = s(F_2/F_1)$ conservation of étendue has been used. $W = d_2/\cos\beta$ is the length of the intersection of the grating plane with the beam; d_2 the size of the camera aperture.

The *resolving power* is then defined as:

$$R = \frac{\lambda}{\delta\lambda} = \frac{m\rho\lambda F_1 W}{s}. \quad (6.5)$$

For a Blazed grating (Blaze angle δ), reflecting under an angle $\psi = 2\theta$ (see fig. 6.2) holds

$$m_B\rho\lambda_B = \sin\alpha + \sin\beta = 2\sin\delta\cos\theta, \quad (6.6)$$

where δ is the Blaze angle and θ the reflection angle towards the specular surface. m_B is the order at which λ_B yields the most efficient reflection. Furthermore, from $F_1W = f_1W/D_1 = f_1/\cos\alpha$ and $\alpha = \delta + \theta$:

$$R = \frac{2f_1\sin\delta\cos\theta}{s\cos(\delta + \theta)}. \quad (6.7)$$

This is about an order of magnitude lower than the limiting resolving power of the grating ($R_{lim} = m\rho W = 370\,000$). The spectral resolving power according to eq. (6.7) is 91 000 for the 100 μm slit. However, it assumes that all optics are perfectly aligned, so that the values as stated in table 6.1 are achieved, which is not necessarily the case as collimator and camera lens have been positioned to minimize astigmatism of the image at the CCD-plane. Moreover, the beam transmitted via lenses and reflected at the grating experiences an increase in étendue, which is not considered in eq. (6.7) either. Therefore the spectral resolving power is directly measured by determining the spectral dispersion (fig. 6.8) and the spectral width of the instrument point spread function (PSF), using a quasi-monochromatic source. The exposure in fig. 6.7 has been taken using the He-Ne-laser (632.8 nm) and a slit of width $s = 100\ \mu\text{m}$ at the slit plane; the cross-section of the intensity has been fitted to a Gaussian function (IDL GAUSSFIT function) in order to obtain the full-width of half maximum (FWHM) of the spectral line in units of the CCD pixel. The result for the spectral bandwidth ($e^{-1/2}$ -value) is (1.657 ± 0.025) pixel or FWHM = (4.59 ± 0.07) pixel.

The spectral dispersion can be derived from the distance between the two spectral lines of the Sodium doublet. Fig. 6.8 shows that these lines of spectral distance 5.924 Å NIST (2011) are physically separated by (490 ± 0.5) pixels, i.e. the spectral

Table 6.2: Slit width s , Resolving power R , and pixel per resolution element p for the two cases of different focal length. R for the 100 μm -slit was experimentally determined, whereas for the other slit-widths the values are scaled according to eq. (6.7).

s [μm]	R	p	R	p
50	245 000	2.3	92 000	2.7
100*	122 500	4.6	46 000	5.5
200	61 000	9.2	23 000	11.0
500	24 500	23.0	9 200	27.4
	$f_1 = 800 \text{ mm}$		$f_1 = 300 \text{ mm}$	

dispersion amounts to 1.209 pm per pixel. However, this value still needs correction, since the spectral dispersion for the He-Ne line is required to calculate the resolving power. Since the lines have been analyzed at the same angle β , the dispersion for the He-Ne-line at the corresponding order needs to be derived. From the spectrograph theory one can derive from the angular range β (detector position), the dispersion at the order $m = 94$ for the 633 nm regime and the dispersion for $m = 101$ around 589 nm, which are proportional to $1/m$ according to eq. (6.6). Hence, the 1.209 pm pixel⁻¹ need to be corrected to 1.125 pm pixel⁻¹ as a corresponding doublet at 633 nm would experience less spread due to the lower order. The resolving power of the setup using the 100 μm -slit can thus be obtained:

$$R = \frac{\lambda}{\Delta\lambda} = \frac{632.8 \text{ nm}}{4.59 \text{ pixel} \times 1.209 \text{ pm pixel}^{-1}} = 122\,500 \pm 1\,800. \quad (6.8)$$

This value is slightly higher than the theoretically expected value according to eq. (6.7). The values for the other slits in table 6.2 have been scaled accordingly. Note that for R -values at the diffraction limit (e.g. for 50 μm slit-width) it is expected that eq. (6.8) will overestimate the actual resolving power. The 50 μm -slit has therefore been omitted for modal noise investigations.

Following the same argument, the result in eq. (6.8) might also be higher than the theoretically expected value, in which case the resolving powers for the 200 μm and 500 μm should be derived separately.

For a lower resolution setup, eq. (6.7) scales with f_1 so that for a faster collimator lens $f_1 = 300 \text{ mm}$ instead of 800 mm, lower resolving power values (table 6.2, right) are obtained. The FWHM and sodium line-separation has been measured and found to be consistent with table 6.2.

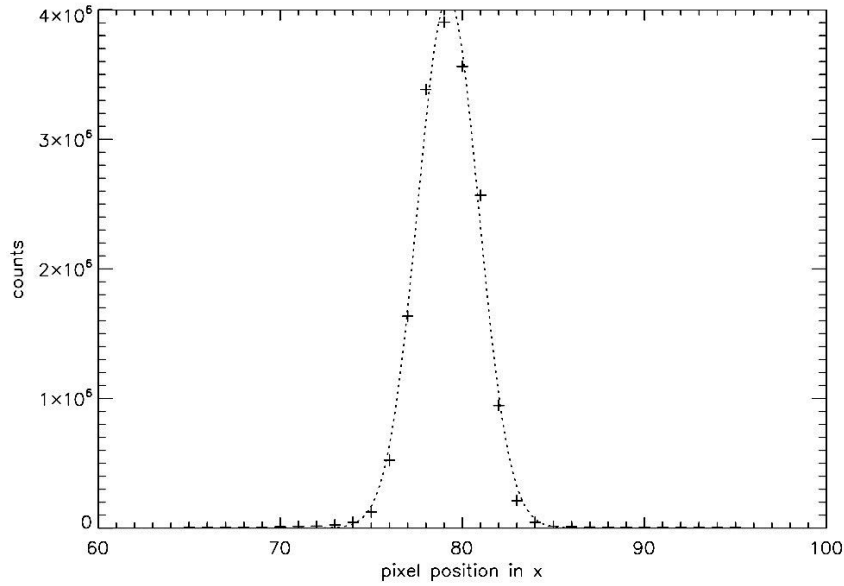


Figure 6.7: Count rates (crosses) for HeNe-laser illumination and corresponding Gaussian fit (dashed line) for the high resolution setup ($f_1=800$ mm). The derived FWHM is (4.59 ± 0.07) pixels.

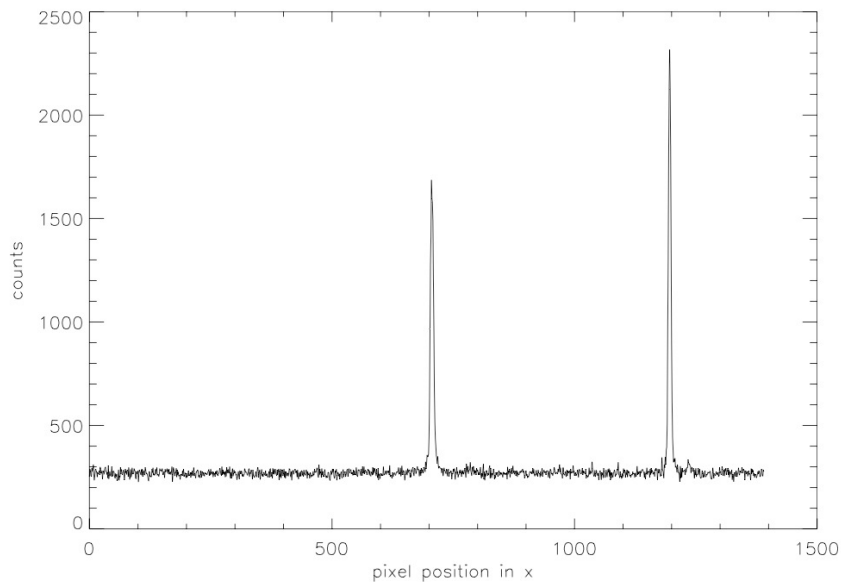


Figure 6.8: Sodium doublet detection to derive spectral dispersion ($f_1 = 800$ mm). The distance in wavelength of these two lines is 5.924 \AA , resulting in a physical distance of 490 pixel, i.e. the spectral dispersion is 1.209 pm per pixel.

6.1.2 Focal Ratio Degradation

As discussed earlier in chapter 3, fibres are étendue non-conserving; the focal ratio at the output is higher than the focal ratio with which is coupled into the fibre, as described by eq. (3.37). In the limit case of $F_{in} = F_{max}$, the focal ratio is not increased, but severe coupling losses occur; the measurement would show a strong photometric instability. The chosen input focal ratio is thus usually a trade-off between coupling-losses and étendue-losses. Often, for a Polymicro FBP fibre of NA = 0.22 (f/2.5), the chosen input focal ratio is around f/3 to f/5, this is why most of the measurements in this thesis are taken with f/3.9.

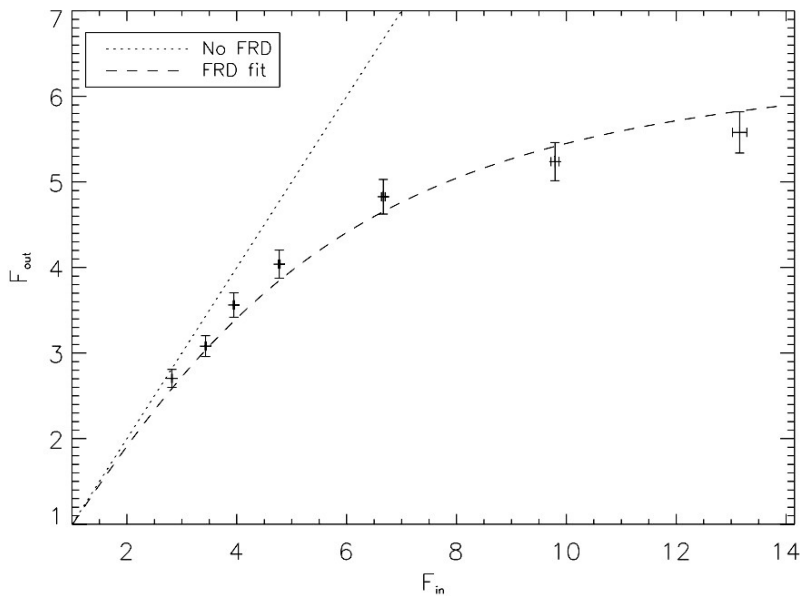


Figure 6.9: Focal ratio degradation: Measurements, ideal fibre (no FRD) and model fit.

Fig. 6.9 shows the fibre response for different input focal ratios for the fibre that has been used in the modal noise and scrambling measurements. The fit to eq. (3.37) is depicted along with the prediction for an ideal (non-FRD) fibre. The first data points fit the prediction for $F_{max} = 6.5$ quite well, whereas the latter two almost show a systematic deviation to lower values from the predicting curve. This is either due to the model being insufficient for the employed high-focal-ratio fibre and thus not following the law in eq. (3.37), or the measurements the alignment of the input beam has a slight tilt towards the optical axis so that the input focal ratio is actually higher than stated (compare fig. 6.10). The output focal ratio is an important factor in order to determine the resulting ρ^2 -parameter.

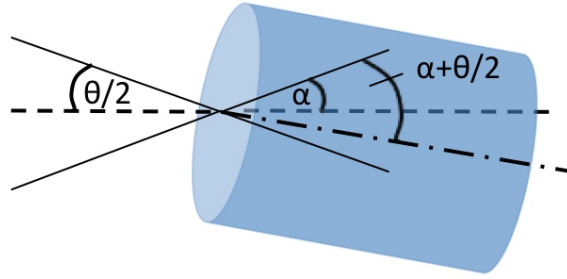


Figure 6.10: Increased focal ratio degradation due to misalignment of the fibre towards the optical axis. Instead of θ the effective coupling angle is $\theta + 2\alpha$.

6.1.3 Influence of polarizing optical components

A fold mirror is used to fit the spectrograph on the limited area of the optical bench. Mirrors and gratings are known to have polarizing characteristics and thus potentially could attenuate a portion of the modes. Therefore the polarization was measured by introducing a polarizing sheet after the slit plane (see fig. 6.2) and found to be lower than 4%. Together with the beam splitter, it can be concluded that the influence of polarizing effects resulting from mirror and grating are marginal and only lead to a small deviation from the non-polarized case. To see this, one can derive the modal noise for light that is partially polarized. In particular, for a circular fibre the number of excited modes is equal in both polarization planes:

$$M_{\parallel} = M_{\perp} = \frac{M}{2}. \quad (6.9)$$

The two speckle patterns for each polarization plane interfere independently and are integrated additively at the detector. Two independent signal-to-noise values can be ascribed to each of these patterns:

$$SNR_{\parallel,\perp} = a \cdot \sqrt{M_{\parallel,\perp}} \quad (6.10)$$

where $a = \rho/(v\sqrt{1-\rho^2})$ is the part independent of the mode number in eq. (5.5). If the intensities of these two polarization planes differ (partial linear polarization) by

$$I_{\parallel} - I_{\perp} = p \cdot I, \quad (6.11)$$

(where p is the polarization degree); the combined SNR results in

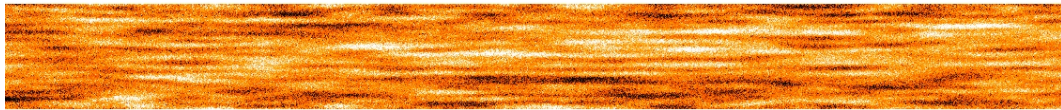
$$\begin{aligned} SNR &= \sqrt{SNR_{\parallel}^2 + (1-p)SNR_{\perp}^2} = \\ &= a\sqrt{(M_{\parallel} + (1-p)M_{\perp})} = a\sqrt{1 - \frac{p}{2}}\sqrt{M}. \end{aligned} \quad (6.12)$$

In the last step eq. (6.9) has been used. For 10 % polarized light, the measured SNR will be reduced by $1 - \sqrt{1 - 0.1/2} \approx 2$ % compared to non-polarized light.

Therefore, the SNR in the following sections are the directly measured values, no polarization correction has been applied. Note that polarizing effects need to be taken into consideration when predicting modal noise effects in highly polarization filtering applications, e.g. when describing modal noise in instruments dedicated for spectro-polarimetry.

6.2 Data analysis

This section first explicates the reduction steps that are necessary to deduce the modal noise value from raw data and then specifies the requirements in exposure time, detailed treatment of the data and properties of the obtained spectra that require critical consideration during the data evaluation process. The same raw data has been used to derive the corresponding visibility-values, which is reported at the end of this section.



(a) Flat fielded spectrum for the unagitated fibre with clearly visible modal structure.



(b) Flat fielded spectrum for the agitated fibre, the photon noise is dominant.

Figure 6.11: The unagitated fibre image clearly reveals a modal structure, which is the origin of modal noise. The agitated fibre image does not show structure, but rather seems to be dominated by white noise.

Fig. 6.11(a) shows the modal pattern that is imparted to the spectra obtained with the setup as described in section 6.1. In order to derive the *SNR*-value that is caused by this structure, a series of carefully conducted reduction steps is required, which are elucidated in the following sections.

6.2.1 Modal noise determination

Each dataset consists of a set of exposures recording the fibre at rest (typically six images) containing the inherent modal noise signature of the bare fibre. These are supplemented by a set of exposures recording the fibre in the agitated state. Additionally, background images of the same exposure time (see section 6.2.2) are recorded.

The *SNR* measurements are conducted at least two or three times in order to ensure the repeatability of the measurement and to estimate the error from their variation, where uncertainties in the measurement and analysis process (see section 6.2.3) are taken into account.

The data analysis involves the following basic reduction steps:

- Background subtraction
- Spectra extraction
- Flat-fielding
- Calculation of standard deviation

The background was subtracted using the corresponding dark-images. For exposure times longer than 10s the images exhibit hot pixels ≥ 3 times the average background signal; typically around five in the entire spectrum, despite the camera being cooled to 0°C. These pixels are identified in the dark-images and removed in all exposures by replacing each with the mean-value of adjacent pixels.

The spectra have been extracted by integrating over a large enough area in the cross-dispersion direction (300 pixel, dashed line fig. 6.12). From fig. 6.13 it can be seen that the *SNR* is then stable, because 1) the fibre far-field for all focal ratios are small enough to fit within this aperture (the critical 20%-value is ≤ 300 pixel for $f/2.6$); and 2) the background noise is negligible. Also, the read-out noise is < 4 ADU (i.e. 1 photo electron) per pixel (manufacturer's specifications) and is therefore neglected. So far it is unclear why the *SNR* decreases after the intensity drops to about



Figure 6.12: The scheme is depicted for which different integration ranges are chosen in order to derive the optimum value for the number of rows to be included for further analysis. All integration ranges are central to the axis.

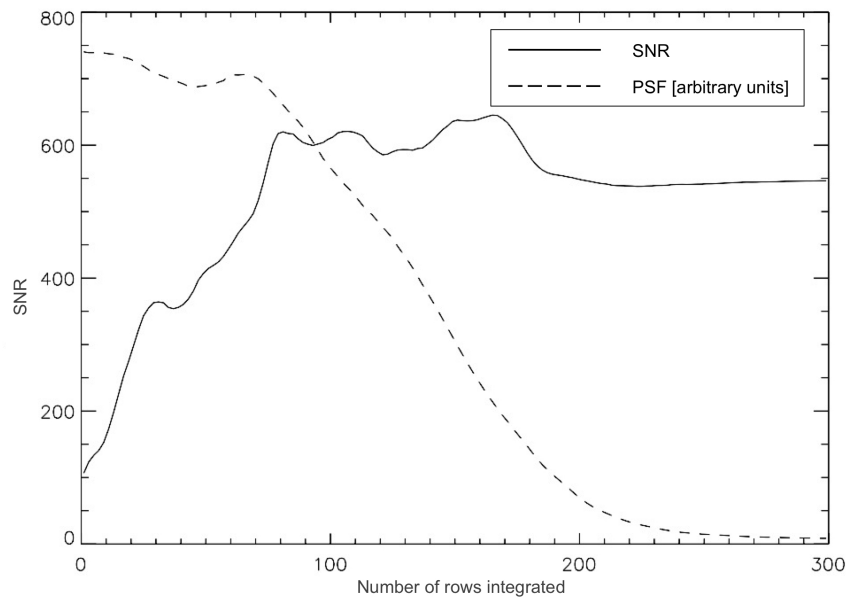


Figure 6.13: The *SNR* has been derived as described in section 6.2.1 where an increasing number of rows are integrated before calculating the *SNR* according to eq. (6.13), compare also fig. 6.12. The *SNR* first increases with larger apertures as predicted by theory (see eq. (5.3)) but decreases after the intensity drops to about 20 % of the central value (here 180 rows) then is stable. Integration ranges of 300 pixel are used for analysis.

20% of the central value (here 180 rows).

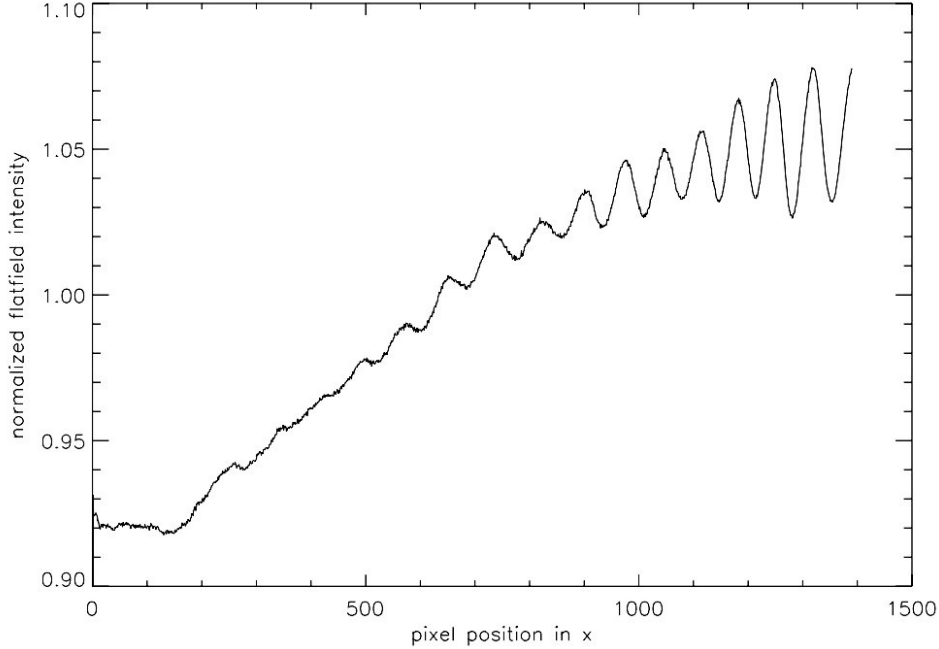


Figure 6.14: Normalized intensity distribution along dispersion direction. Clearly visible is the ripple pattern towards the red end of the spectrum. The ripple pattern supposedly can be traced back to the Fabry Perot effect caused by the bandpass filter used in front of the CCD.

After spectra extraction, the data has been reduced to a one-dimensional array containing intensity information over spectral position (see fig. 6.14). In order to remove any instrumental signature (e.g. beating pattern due to the bandpass-filter, fig. 6.14), the unagitated fibre exposures are flat-fielded against the exposures of the agitated fibre (fig. 6.15). The flat-fielded spectra are binned according to the size of one spectral resolution element (see Table 6.2). In the final step the standard deviation σ_I between the bins is calculated in order to obtain the signal to noise value:

$$SNR = I_{mean}/\sigma_I. \quad (6.13)$$

where

$$\sigma_I = \sqrt{\frac{\sum_i^{N_{bin}} (I_i - I_{mean})^2}{N_{bin} - 1}} \quad (6.14)$$

and I_i are the total intensities in each bin, N_{bin} the number of bins and I_{mean} the mean intensity.

After calculating the modal noise for the unagitated fibre exposures, the same proce-

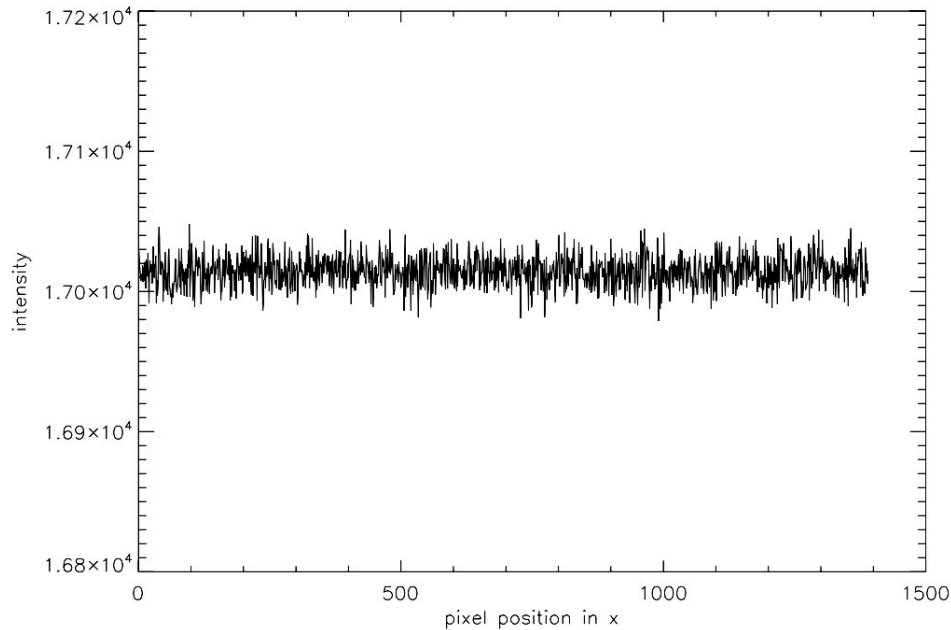


Figure 6.15: A 'flatfielded flatfield'; The flat field was applied on the agitated fibre images, then the intensity distribution is plotted as in fig. 6.14, the dominating photon noise is visible.

ture was applied to an independent set of exposures of the agitated fibre to compare with the theoretical photon noise, which was directly derived from Poisson statistics. This is necessary to monitor the quality of the flat-fielding. With a few exceptions of long integration times, the agitated fibre modal-noise values match the theoretical photon noise, while always achieving significantly higher *SNR*-values than for the unagitated fibre. The remaining *SNR*-difference from the Poisson value is probably due to additional sources of noise (as discussed in section 6.2.2).

6.2.2 Exposure time

Fig. 6.16 depicts how the exposure time was chosen: For increasing exposure times the data was recorded and its *SNR* determined until a maximum value was reached. The configuration (200 μm slit, $f_1 = 300$ mm, input focal ratio $F = 6.5$) was used. For the unagitated fibre the *SNR* is significantly lower than for the agitated fibre and reaches the maximum-value already after 12 s exposure time, obviously to declining after 48 s. The exposure time to acquire modal noise data was chosen to be 36 s (6 frames, 6 s each frame).

Choosing too long exposure times decreases the *SNR* which indicates the occurrence of an additional source of noise. Very long exposure times can thus be critical and lead to a diminished *SNR* that is overestimating the modal noise. In fact, it is

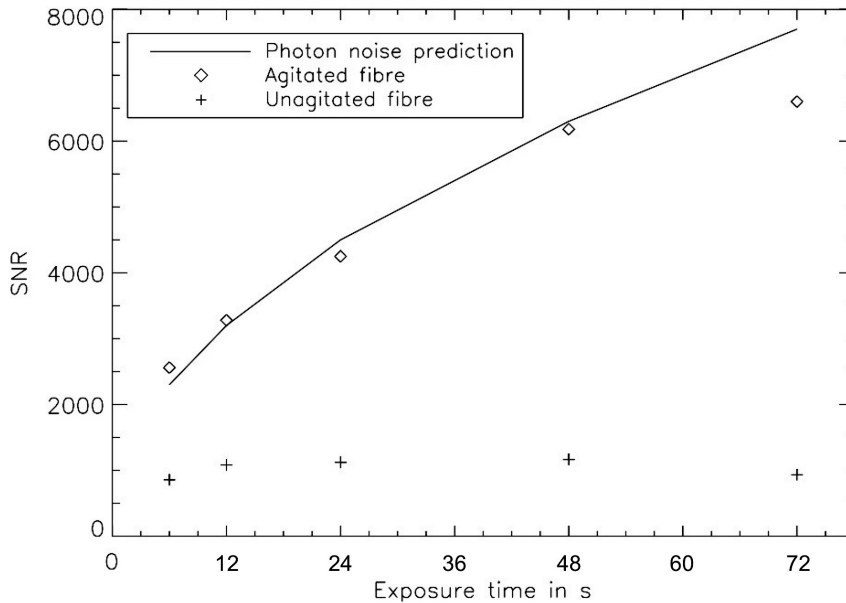


Figure 6.16: Exposure time was increased and for each dataset the modal noise calculated in order to find the point where the limiting signal-to-noise is reached. In this example 6 s was chosen for the exposure time of the image stack, exposure times increase for higher signal-to-noise ratios.

assumed here that the limiting SNR -value is equal to modal noise, although other sources of noise can contribute significantly, especially in the high SNR -regime. Potential sources of noise are Poisson noise (eliminated for long exposures), variations in the light source intensity and colour as well as fluctuations in the speckle pattern during acquisition of the unagitated fibre spectra, which could be caused by air currents (minimized) or shifts in temperature. The error in the SNR of the unagitated fibre images in fig. 6.16 is estimated during the data analysis process and is of the order of 30-40, too small to appear in the graph.

6.2.3 Integration range in dispersion direction

Fig. 6.17 shows the different noise contributions against an increasing number of spectral resolution elements that are included in the analysis for the unagitated, the agitated and the theoretical photon noise prediction per spectral resolution element (depicted here are the noise values rather than the SNR as used throughout the thesis in order to visualize the characteristics of the unagitated fibre more clearly). All noise contributions attain an approximately stable value for a wide enough integration range. The noise resulting from the unagitated fibre is about five times higher than the noise resulting from an agitated fibre, with the major contribution resulting from photon noise.

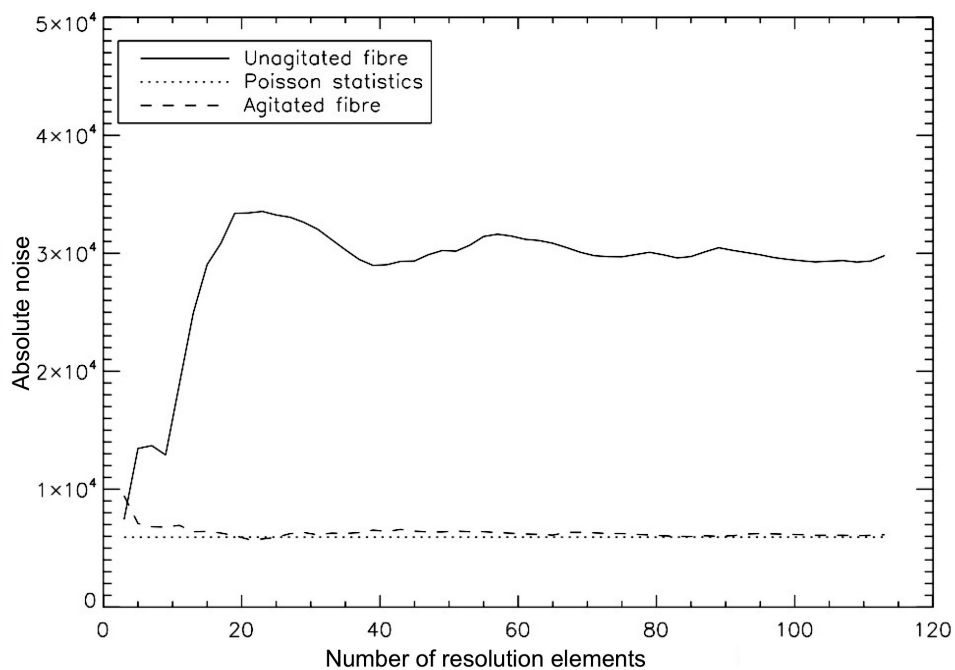


Figure 6.17: Absolute noise contributions for $s = 200 \mu\text{m}$, $f_1=300 \text{ mm}$, $F = 3.9$, first measurement.

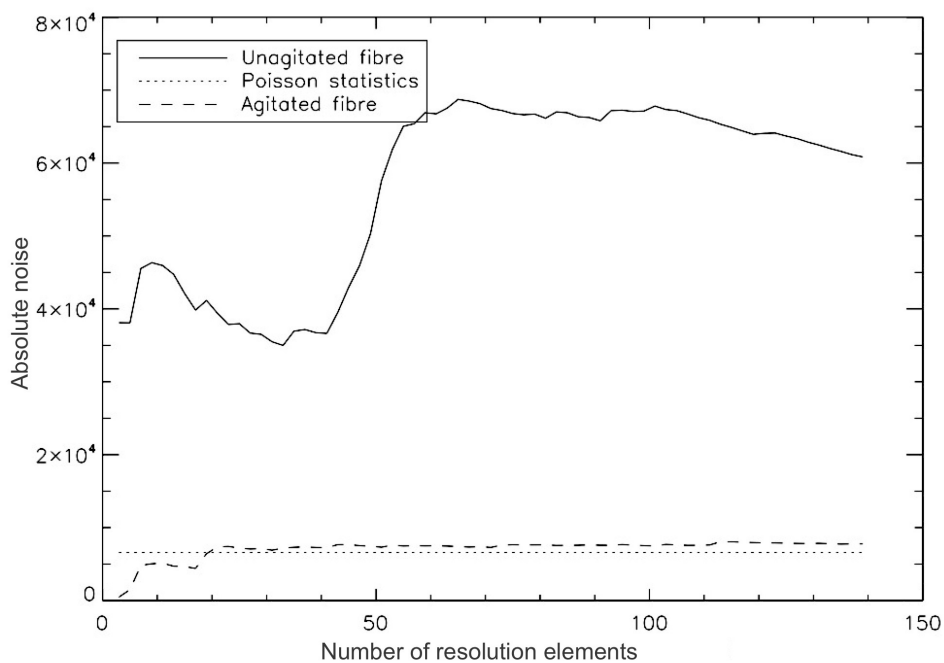


Figure 6.18: Absolute noise contributions for $s = 200 \mu\text{m}$, $f_1=300 \text{ mm}$, $F = 3.9$, second measurement.

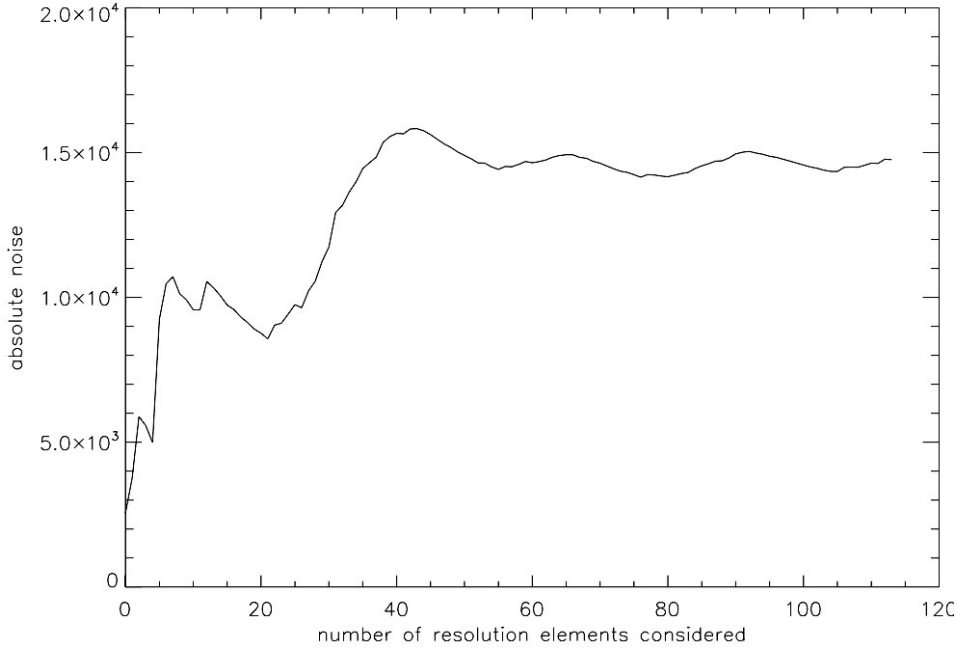


Figure 6.19: Simulation of unagitated fibre noise.

Interestingly, the noise of the unagitated fibre exhibits some oscillatory behavior and gets more stable as the number of the N_{bin} in eq. (6.14) is increased (i.e. more resolution elements are considered in the analysis).

This could be explained by a frequency fraction in the actual data. Simulated data in fig. 6.19 was created modulating a harmonic function and Poisson noise on a 1D-vector (as one would obtain after the spectrum extraction described above). The periodicity and the amplitude of the harmonic function was chosen so that the derived noise dependence shows similar behavior as the original data (see fig 6.19). However, this is just one possible explanation, other sources of noise or instabilities cannot be excluded. Comparing the actual input vector of both – the original and the simulated data, the period in the original data appears to be shorter; but it also shows that there is a multitude of frequency components contributing to the resulting noise pattern in the original data.

The noise in fig. 6.17 seems to be clearly stabilizing around 3×10^4 for the maximum integration range, but it needs to be said that not every set of exposures displays such a clear behaviour and oscillates about a definite mean as in the example above. The actual noise value is calculated using one period of oscillation (i.e. 35 pixels for the example in fig. 6.17), taking its mean value as the actual modal noise value and its standard deviation as error in the measurement. In case of doubt, the data is dismissed and the measurement repeated, or if the signal does not change for

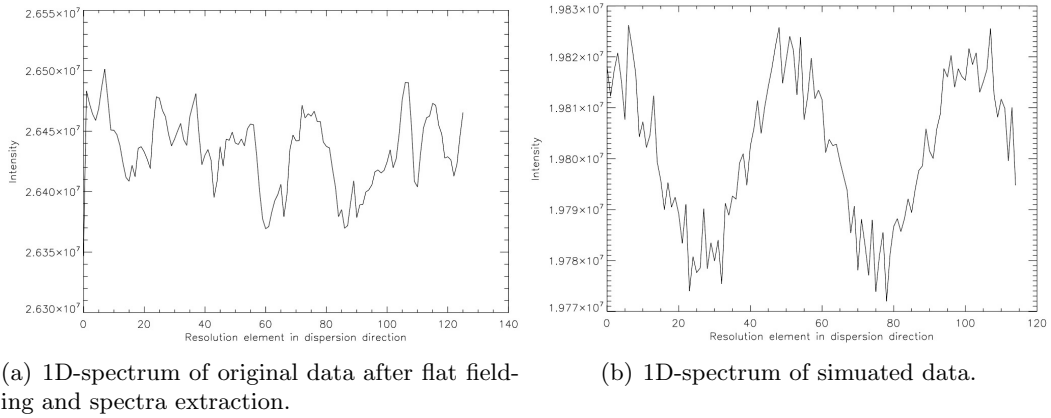


Figure 6.20: Input vectors that lead to the graphs in figs. 6.17 and 6.19 after applying the standard deviation.

the repeated measurement, a very high measurement uncertainty is chosen that encompasses the whole range of values that the noise is adopting (i.e. the absolute noise in fig. 6.18 would be $(5 \pm 1) \times 10^4$).

Usually, the measurement uncertainty is derived from the standard deviation of three (at least two) repeated measurements. However, if the measurement error due to the unclear modal noise behavior (such as oscillating around a mean value) of one single measurement is larger than the standard deviation, the combined modal noise of different data sets is used by weighting according to their error.

6.2.4 Visibility determination

The image in fig. 6.21 has been created by flat-fielding the central core area of the fibre-spectrum before applying the spectral extraction to the data. The pattern clearly shows a modal structure, the origin for modal noise. The visibility in each of these speckle patterns is derived by calculating the contrast between neighboring minima and maxima at six different positions of the spectrum:

$$v_{exp} = \frac{I_{max} - I_{min}}{I_{max} + I_{min}}. \quad (6.15)$$

From these six visibility values the mean value is calculated, their scattering is used to estimate the uncertainty.

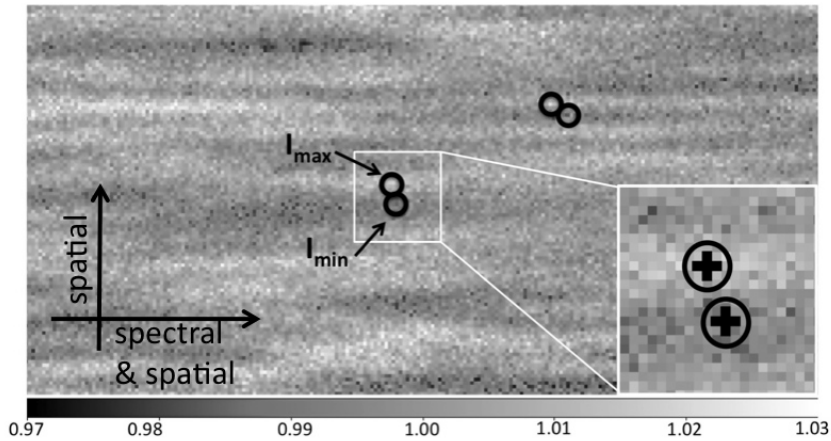


Figure 6.21: Unagitated fibre images are flat-fielded yielding a modal pattern. For visibility determination, adjacent minima and maxima are selected (circles) and the intensity of five pixels added (cross-shaped area) to feed into eq. (6.15). The linear greyscale is normalized to the mean intensity.

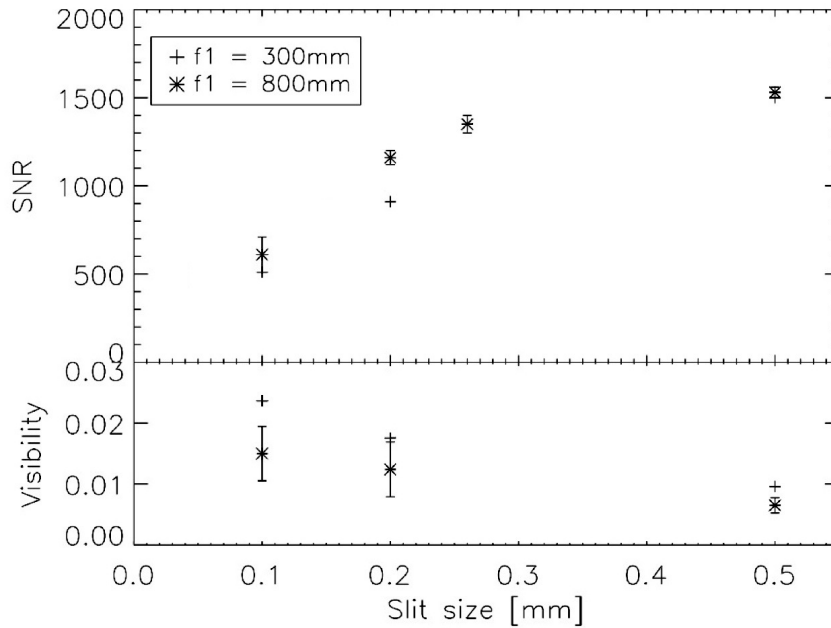


Figure 6.22: Signal to noise and visibility vs slit sizes s .

6.3 Experimental results

Fig. 6.22 and fig. 6.23 show slit size s and input focal ratio θ_{in} vs. signal-to-noise SNR and visibility v , respectively. These values are directly derived as described in section 6.2. For this particular setup, the SNR -values are $\lesssim 10^3$, and visibility $\lesssim 5\%$, typically 1-2%. This is significantly lower than any other data that can be found in the literature (e.g. Kanada & Aoyama, 1983) where light-sources of limited

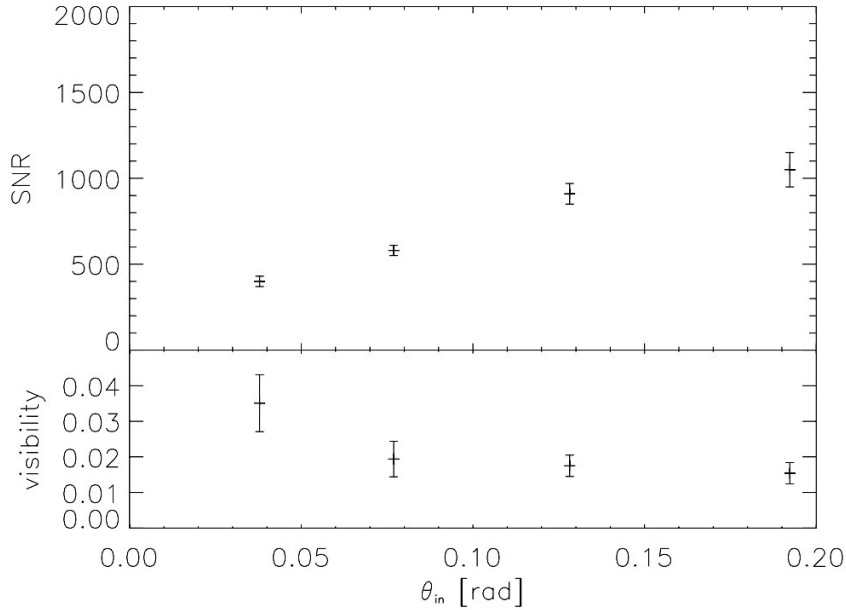


Figure 6.23: Signal to noise and visibility vs input focal ratio θ_{in} .

bandwidths were deployed.

As can be seen, variation of an input parameter (e.g. s or θ_{in}) changes both SNR and v . Eq. (5.5) suggests that SNR is composed of a visibility and a coherent term, therefore determining the direct SNR -dependence is complicated. By separate inspection of these two terms one can measure v , but SNR_{coh} is difficult to measure and not directly ascertainable from the experimental data. However, rather than measuring each of its components separately, the task of determining a concise SNR -model was divided into two steps:

1. *Verifying the coherent model:* One starts out with the assumption that SNR is factorisable. In order to show that this assumption is true, it is sufficient to show that $v \times SNR$ gives the same response as if illuminating the spectrograph with monochromatic light (from eq. (5.5): $SNR_{coh} = v \times SNR$, this is the factorisation).
2. *Determine visibility dependence:* After showing that 1 is fulfilled, the problem of modal noise prediction reduces to the problem of predicting the visibility.

6.3.1 Verifying the coherent model

In the following it will be shown that the experimental results support the proposition that SNR is factorisable, i.e. $SNR = SNR_{coh} \times \frac{1}{v}$ because the product

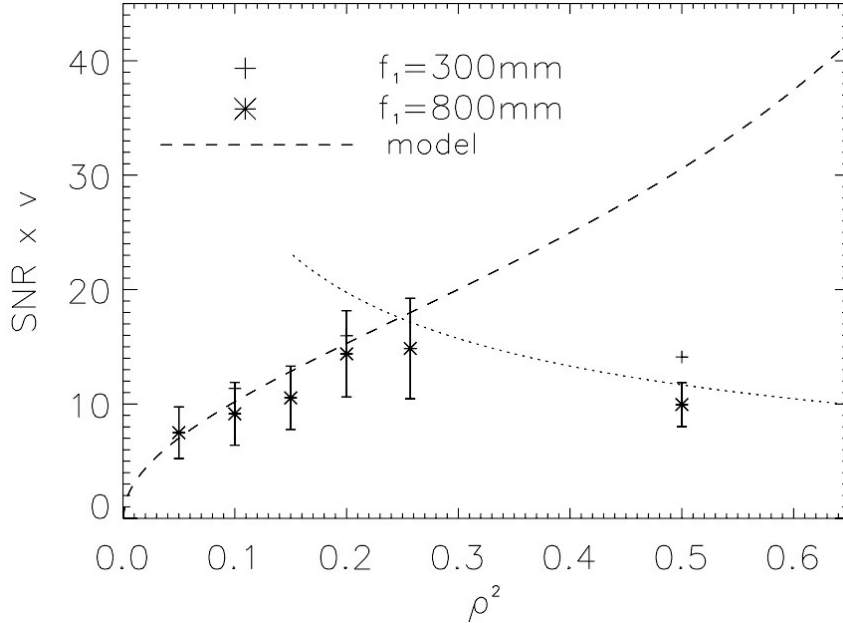


Figure 6.24: Signal-to-noise times visibility vs. ρ^2 for $f_1 = 300$ mm and 800 mm data (error bars are in the same range for both data sets, but for clarity reasons only represented for the $f_1 = 800$ mm-case). The theoretical prediction corresponds to $M = 900$ modes as can be obtained from an independent speckle-count measurement (see fig. 6.25). This is consistent with the six data points at $\rho^2 \leq 0.2$. Deviations occur for $SNR > 1200$ (dotted line) as is the case for $\rho^2 = 0.25$ and 0.5 , for a detailed discussion see text.

$SNR_{coh} = v \times SNR$ follows the the functional dependence as described by eq. (5.3) for (a) ρ^2 and (b) the mode number M .

Fig. 6.24 shows ($v \times SNR$) vs ρ^2 (ρ^2 is a measure for the aperture area that is truncated). The coherent model is supported by the six data points at $\rho^2 \leq 0.2$ of the high resolution ($f_1 = 800$ mm) and the low resolution ($f_1 = 300$ mm) setup. The theoretical prediction assumes a mode volume M of 900 modes. Not included in the theoretical fit are the $\rho^2 = 0.25$ and 0.5 data points as their low value indicates a systematic deviation from the theory. This could be explained by an additional source of noise that becomes effective when approaching high SNR -values (of the order of 1200 and higher, see dotted line in fig. 6.24) and longer exposure times (see also fig. 6.16 where the SNR decreases after reaching a maximum). However, it is not clear what this additional source of noise might be. An investigation with lower SNR -values, higher ρ^2 -values, a higher resolution setup or a test-fibre guiding fewer modes would be required to explore further. The error bars in fig. 6.24 are dominated by the uncertainty in visibility prediction.

To further investigate the additional source of noise, the SNR was measured for the case that no slit was placed at the spectrograph entrance. However, this could not

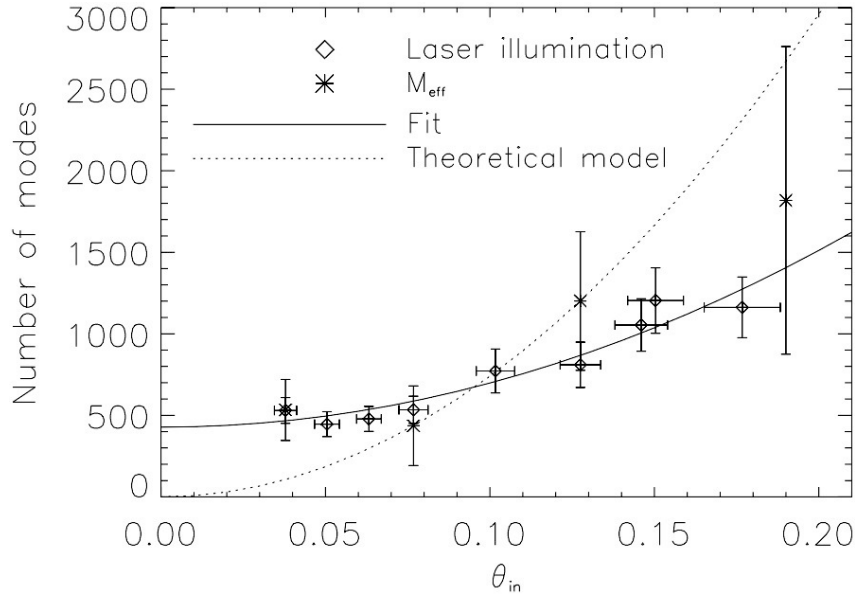


Figure 6.25: Number of guided modes vs. θ_{in} . M_{eff} is derived from modal noise and visibility measurements as in eq. 6.16. The dotted line represents the theoretical fit to $\propto \theta^2$ of the two central values at $\theta_{in} = 0.08$ and 0.13 . Counting speckles under laser illumination, the θ_{in} -dependence obeys the square law (solid line) but with an offset.

fully explain the additional noise that causes the $\rho^2 = 0.5$ data points to deviate from the predicted value. This in turn might indicate that this diminished modal noise arises from the speckle pattern itself possibly being subject to changes over long integration times. A slight decline could be detected for longer integration periods and when using a neutral density filter (20% transmissivity) accordingly. The impact can become very significant, especially in the very sensitive high SNR -regime.

To further support the assumption in 1., i.e. $SNR_{coh} = v \times SNR$, its θ -dependence is investigated. If SNR is factorisable as proposed in eq. (5.5) and if it can be trusted in the ρ^2 -dependence as stated; using eq. (5.3) the value $SNR \times v$ is a measure for the number of modes that are excited in the fibre at the central wavelength:

$$M_{eff} = (SNR \cdot v)^2 \left(\frac{1 - \rho^2}{\rho^2} \right) - 1. \quad (6.16)$$

This is a function of ρ^2 (known value, set by experiment) and the $SNR \times v$ -product. Hence it follows $M_{eff} = M_{eff}(SNR \times v)$, i.e. M_{eff} is a function of the $SNR - v$ -product.

Fig. 6.25 shows the effective number of excited modes M_{eff} vs. angle of the input cone θ_{in} , where the crosses are the M_{eff} -values (see eq. (6.16)) which are derived

from $SNR \times v$ -values. The dashed line is a fit to the experimental data $\propto \theta_{in}^2$ and the diamonds represent the number of modes derived from laser illumination. The fit to the speckle data (solid line) obeys the square law, but has an offset. This implies that there will always be a certain number of modes, irrespective how small the input angle θ_{in} is chosen (\Rightarrow FRD).

Note here that ρ^2 varies with the size of the far field at the output of the fibre, which is subject to the input focal ratio and focal ratio degradation. Moreover, the term *effective* mode number is used here to comply with the fact that the modes are not equally excited. The total number of excited modes is lower than the number of modes that is allowed for the mode volume in eq. (5.4). Depending on the symmetry of the fibre launch, different mode groups are excited.

According to Daino et al. (1980), the number of excited modes is equal to the number of speckles that can be counted when observing the fibre under monochromatic light. The white light source was replaced by a standard He-Ne laser to obtain a high contrast speckle pattern. Here it has to be considered that the laser light is polarized, thus the expected number of speckles is only half compared to the case of unpolarized input light. The number of modes depicted in fig. 6.25 is therefore derived by multiplying the number of counted speckles by two.

The relationship between input focal ratios f/3.9 and f/6.5 ($\theta_{in} = 0.13$ and 0.08) is consistent with the theoretical fit, i.e. the number of excited modes rises with the square of the coupling angle. Nevertheless, the $\theta_{in} = 0.04$ and 0.19 are inconsistent with the theory. However, all M_{eff} -values show consistency with the number of modes as derived from counting the speckles under laser illumination, indicating that the product $SNR \times v$ can indeed be identified with the number of guided modes and thus supports the factorization described in 1.

It is not straightforward to decide whether to base the model prediction on input focal ratio, output focal ratio or a mixture of both, because part of the focal ratio degradation could occur at each of the fibre endfaces (compare length-effect, Poppett & Allington-Smith, 2010), leading to a complex mode-population dependence along the fibre. Modal noise is chosen to be a function of θ_{in} as this seems to fit the coherent model best. For a better grounded statement, the actual mode population in the fibre as a function of the coupling angle needs to be known; Unfortunately, this is hard to determine.

6.3.2 Determining visibility dependence

The goal of this section is to determine the visibility dependence of the spectrograph parameters; input focal ratio and slit-width at the spectrograph entrance. Previ-

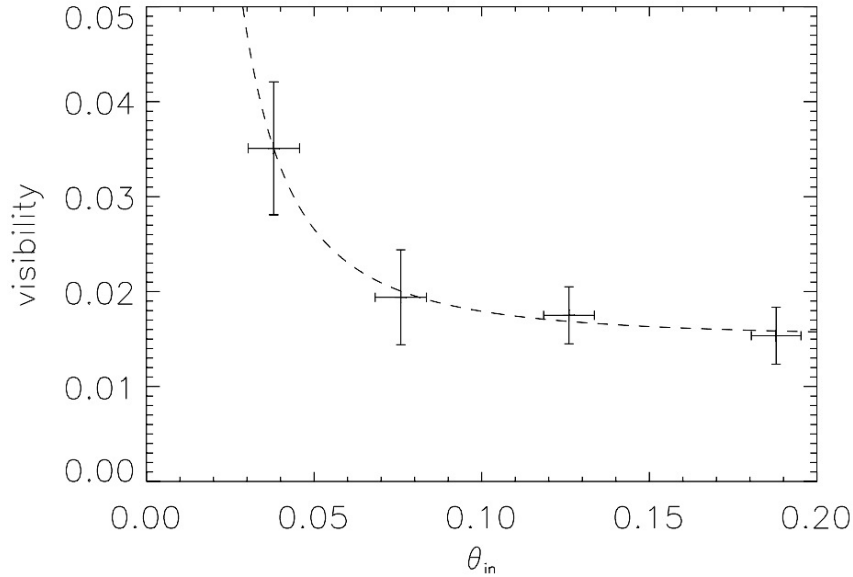


Figure 6.26: Visibility values for different input focal ratios. The experimental values well reflect a θ^{-2} -law (dashed line).

ous considerations have shown that the initial hypothesis holds true; the visibility \times signal-to-noise product is consistent with the coherent model as described in eq. (5.3). Furthermore, the number of excited modes rises with θ^2 (fig. 6.25) as determined from directly counting the number of speckles at the fibre exit (due to the offset being slightly different from the theoretical prediction). Therefore it is concluded that once the visibility is known, the modal noise is determined (see section 6.3.1). A fibre that guides a large number of modes will possess a large range of propagation constants and thus will exhibit a low visibility. Likewise, a wide slit reduces visibility (cf. eq. (5.8)).

The graph in fig. 6.26 shows the visibility as a function of the input focal ratio θ_{in} (same data as used in fig. 6.23 and fig. 6.25). From eq. (5.8) the visibility is expected to follow a θ^{-2} -law, which indeed reflects the experimental data if one accepts an offset of 1.7%. This offset becomes dominant for fast input beams ($\theta > 0.05$ rad). Visibility as a function of slit width is depicted in fig. 6.27. Although eq. (5.8) predicts an s^{-1} -dependence, the experimental values suggest $s^{-0.5}$ -dependence. These first results give a parameterization, which fits in well with the predictions of the simplified model. However, it also shows that the analytical model needs further refinement and may best be understood by simulation based investigations that reflect the complex physical processes when speckle images of adjacent wavelengths interfere at the detector plane.

Counter-intuitively, the supposed higher spectrograph resolving power for $f_1 =$

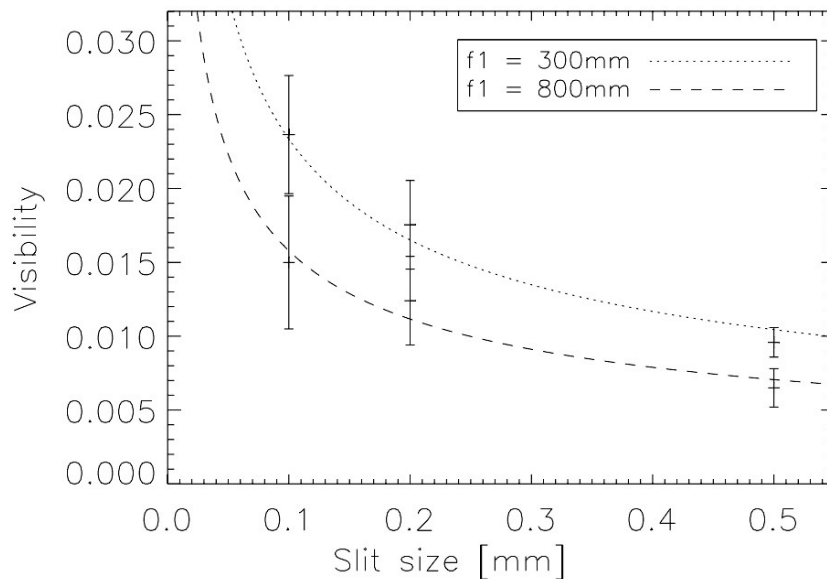


Figure 6.27: Visibility values for different slit widths, compared for two different resolving powers ($f_1 = 300$ mm and 800 mm).

800 mm (= higher coherence) shows lower visibility values than the lower resolving power setup ($f_1 = 300$ mm). It cannot be excluded that this effect is an inherent feature of the way the spectra overlap at the detector. However, it seems more likely that the apparent independence is due to problems in the setup: repeated measurements with re-alignment of the fibre-launch resulted in a *SNR*-degradation of about 15%; also differences in the optical performance of the applied collimator lenses possibly affect the measurement. In order to conclude for a visibility-dependence on spectral resolving power, this point needs clarification.

6.4 Conclusions

Modal noise can be a limiting factor to the photometric accuracy of high resolution spectroscopy applications. This chapter focussed on the spectrograph characteristics such as low visibility, high input focal ratio and intermediate fibre lengths; although due to experimental restrictions, slit-losses could not be kept small. These requirements were found to be so far insufficiently addressed in the literature (chapter 4). Furthermore, it was experimentally verified that the model for modal noise prediction can be separated out into a visibility and a coherent term. Thus, modal noise prediction reduces mainly to predicting the visibility.

A test-bench for experimental investigations was built, with resolving powers in the range of $R = 10\,000 - 200\,000$. Its design and data-analysis are presented. The results support the separation approach, showing that modal noise factorizes as predicted. However, the working range of the spectrograph is limited to a certain SNR , making high ρ^2 and low v inaccessible for this investigation. As the coherent term can be determined from speckle-statistic considerations, it is sufficient to know the visibility for noise prediction. Therefore, further examinations concentrated on predicting the visibility. The functional dependence of the experimentally derived visibility values show partial agreement with the simplified theoretical description given in section 5.3.

Chapter 7

Incomplete scrambling

Due to atmospheric variations and telescope tracking, the angular position of an object varies, causing the signal to shift at the detector plane of the spectrograph by a corresponding amount. For the traditional, non-fibre-based spectrograph these variations can severely limit the instrument stability (e.g. Boisse et al., 2010), whereas fibre-coupled instruments only partially retain spatial and angular information so that differing coupling conditions largely cause the same spectrograph response and thus stabilize the signal, a property that is referred to as *scrambling* in the literature. However, the scrambling is not perfect and the signal at the output of the fibre partially retains information of the fibre input.

The scrambling properties of fibres studied by Avila et al. (2006) are presented in section 7.1.1. His investigations are restricted to the fibre near-field and direct imaging of the fibre on the detector. An expansion of these investigations will be presented here which shows that the effects in the far-field and for spectrally analyzed light are of the same order of magnitude. These findings are potentially explicable by modeling the fibre output intensity using ray-tracing techniques in section 7.2. This concept is still under investigation and only a brief outline is given in order to set this work into context with previous investigations. A last section presents a procedure to obtain the photometric uncertainty due to incomplete scrambling from data acquired using the experimental apparatus described in chapter 6.

7.1 Barycentre instability and scrambling gain

This section describes the investigations conducted by Avila et al. (2006) characterizing the barycentre stability for the near field of standard optical fibres, major findings are summarized. Subsequently, the research is extended to the far-field using data obtained with the same apparatus as used in chapter 6 for the modal noise investigations.

7.1.1 Scrambling gain investigations by Avila et al

HARPS (High Accuracy Radial velocity Planet Searcher), in operation at the 3.6 meter telescope at La Silla since 2003 (Mayor et al., 2003), is one of the first spectrographs dedicated to exo-planetary research, applying the radial velocity method at a very precise level ($\sim 3 \text{ cm s}^{-1}$). Today, HARPS is delivering science data but also used as a test-bed for the new generation of instruments, attempting to push the radial velocity accuracies to a level of the order of few centimeters per second (e.g. ESPRESSO, Wilken et al., 2010), showing the fundamental limitations of the bare (excluding means for improvement) fibre due to incomplete scrambling.

An extensive study on scrambling properties of standard optical fibres was undertaken by Avila et al. (2006) and (2008). Originally, their work was motivated during design-phase of the CODEX instrument, a high resolution Echelle spectrograph dedicated to precision radial velocity measurements, aiming at a few centimeters per second precision. Their study on CODEX concentrated on exploring mitigation strategies to improve the scrambling qualities of the standard optical fibre (FBP, Polymicro), investigating the fibre-image PSF displacement at the detector plane as a function of the star-displacement at the fibre-input. In order to quantify the scrambling performance, a scrambling gain factor G is introduced:

$$G = \frac{d/D}{f/F}, \quad (7.1)$$

where d is the centre-shift of the input illuminating spot, D the fibre core diameter, f the shift of the point spread function (PSF) at the detector plane and F denotes the full-width-of-half-maximum (FWHM) of the PSF (fig. 7.1).

CODEX was intended to achieve radial velocity precisions of a few tens of cm s^{-1} , but as the optical fibre was limited to scrambling gains of ~ 100 -150, mechanisms like mechanical agitation devices and fibre “squeezers” were applied and investigated with the aim to increase the scrambling to 1 000 in order to fit the instrument requirements. Scrambling gains of the order of 600-1 300, in some cases even scram-

bling gains of several thousands were obtained, but with unacceptable throughput losses. The initial scrambling gain for a 100 μm and a 200 μm - fibre reached similar values ($G = 100$). When agitating the fibre with a mobile phone the scrambling was improved for the 200 μm - fibre significantly ($G = 800$) whereas it is unclear why the scrambling gain for the 100 μm fibre was not improved.

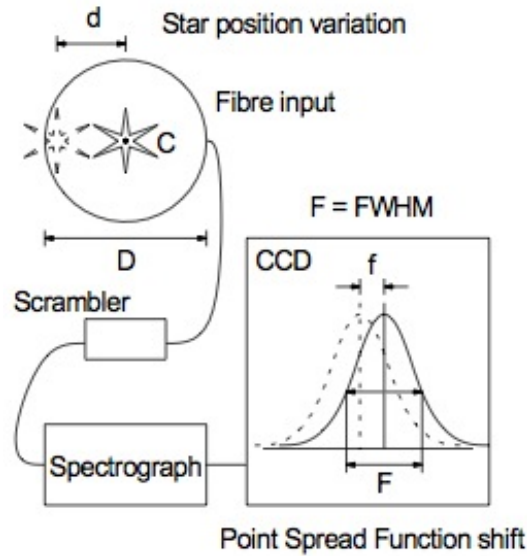


Figure 7.1: The scrambling gain G is defined as the ratio between shift d of the input illumination in units of the fibre core diameter D and the shift f of the barycentre of the resulting intensity pattern at the fibre output in units of the size of the FWHM F (see eq. (7.1)).

7.1.2 Experimental Investigation

Compared with Avila et al., the measurements have been conducted using a full spectrograph setup rather than determining the barycentre shift from directly imaging the fibre onto the detector. On the one hand, the information about the shift in the dispersion direction is lost, but it is assumed that the relative shift is symmetric in x - and y - so that the knowledge about the relative shift in one spatial direction is sufficient. Apart from the greater convenience of re-using the same apparatus as that employed in section 6.2.4, a direct comparison to the barycentre shift due to modal noise can be made.

For the tests, the slit at the spectrograph entrance and the He-Ne laser line filter was removed. The spectral orders now overlap, and thus, the measured de-positioning of the barycentre is no longer due to coherence effects but can be ascribed to effects in broad band due to fibre and alignment properties, showing that the phenomenon of

incomplete scrambling is fundamentally different to modal noise. Furthermore, the pinhole size at the fibre launch has been reduced to 50 μm , such that the spot at the fibre input is only a quarter of the size compared to the modal noise measurements (again, a 100 μm fibre was illuminated). As a result, the spectrum at the detector plane exhibits a visible sub-structure as can be seen in fig. 7.3, which changes as the spot is moved across the core of the fibre end-face. The relative shift of the barycentre of this pattern is determined and used as a measure for the scrambling response of the fibre.

It should be mentioned that the measurements concern the fibre far-field as the existing spectrograph setup of section 6.2.4 allows for studying the far-field only. This is in contrast to the investigations of Avila & Singh who restricted their investigations to the fibre near-field.

According to literature (e.g. Barnes & MacQueen (2010), Bouchy & Connes (1999)), scrambling properties of the fibre far-field are expected to be better than the fibre near-field. So called ‘optical image scrambling devices’ exchange near-field and far-field and thereby improve the scrambling by a factor of 2-10. It is therefore expected to measure a slightly higher scrambling gain than in the fibre near-field. There is, however, no obvious explanation why the near-field scrambling properties should inherently differ from the far-field.

The pinhole image illuminating the fibre-input is moved across the core by $(70 \pm 5)\%$ of the core diameter and the corresponding barycentre shift in cross-dispersion direction is determined. The pinhole image was moved back to its respective position three times, confirming the repeatability of the measurement. A barycentre movement can only be detected in cross-dispersion direction, shifts in the dispersion direction are not visible due to the character of the technique (see also fig. 7.3).

The results are given in table 7.1, with the error denoting the scattering of the single measurements around its mean value. The detected barycentre shift for horizontal input-illumination shift is less than for vertical, implying that there is some memory of the axis along which the pinhole-image is moved. However, on average the image centre is shifted by $0.26 \pm .05\%$ of the fibre far-field image size. Using eq (7.1) this corresponds to a scrambling gain of 270 ± 60 . As an extra check, these values have been compared with the bary-centre shift when changing the illumination from offset to centre and found to be consistent ($G = 210 \pm 20$).

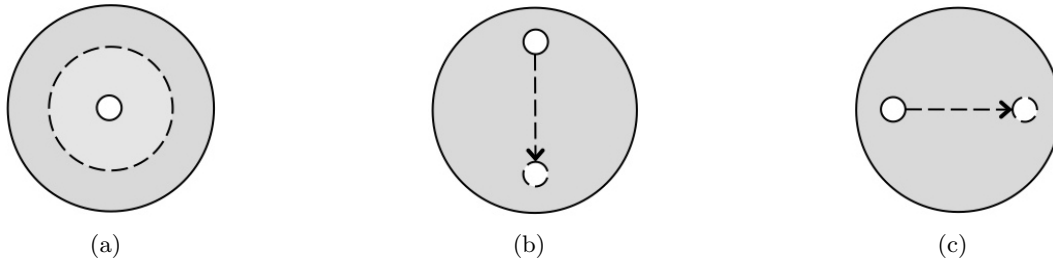


Figure 7.2: Fibre core image at the fibre input: a) Central illumination with 200 μm pinhole for modal noise investigation (dashed line) in comparison with with 50 μm pinhole for scrambling investigation (solid line); b) Shifting the illumination vertically; c) Horizontal variation of input illumination.

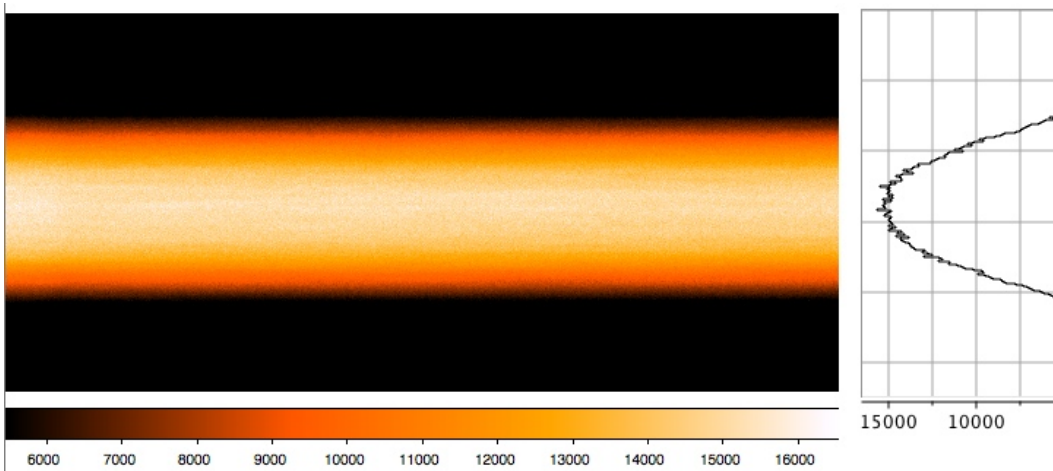
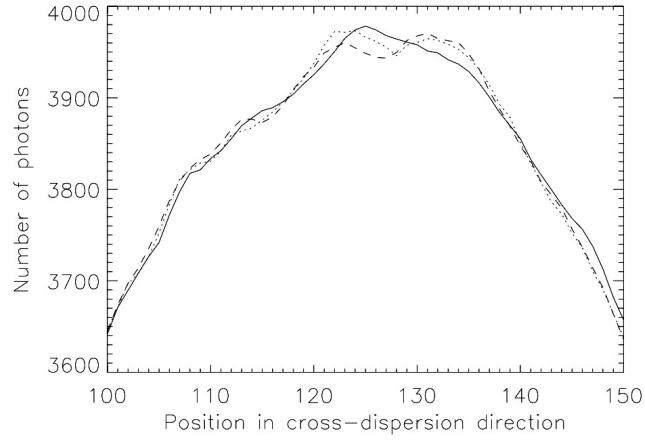


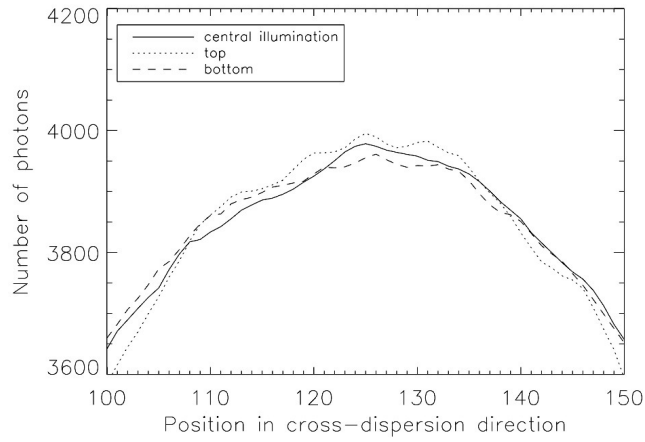
Figure 7.3: Spectrum obtained for scrambling investigations. The pattern that becomes visible as stripes in the dispersion direction can be related to the barycentre shift.

Table 7.1: Barycentre shift at the fibre exit far-field in pixel and fibre core width. Shown are the relative shifts for input illumination spot moved vertically and horizontally along the fibre by 70% (compare fig. 7.2).

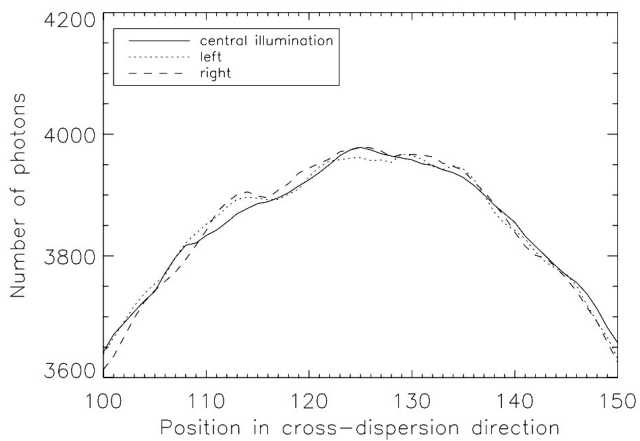
	shift [pixel]	shift [FWHM]
horizontal	0.19 ± 0.04	$(1.9 \pm 0.4) \times 10^{-3}$
vertical	0.32 ± 0.09	$(3.2 \pm 0.9) \times 10^{-3}$
average movement	0.26 ± 0.05	$(2.6 \pm 0.5) \times 10^{-3}$



(a) Central illumination for three independent measurements.



(b) Vertical shift



(c) Horizontal shift

Figure 7.4: Change in cross-section for (a) central illumination. When comparing with (b) vertical- and (c) horizontal- shift, the change in cross-section is similar, although the calculated bary-centre shift is lower for the central illumination.

When examining the different cross-sections (fig. 7.7(e) and fig. 7.7(c)), the pattern at the output changes when the spot is moved across the fibre. But although the pattern does not appear to be repeatable when the spot is moved back to its initial position (fig. 7.7(b)), however, the barycentre shift is repeatable as the scattering of the bary-centre position in table 7.1 suggests.

Recalling section 2.2, eq. (2.8), the scrambling gain measured here corresponds to a repeatability for the radial velocity measurement of

$$\Delta v_r = \frac{c}{R} \frac{1}{G} = 6 \text{ ms}^{-1}$$

when assuming a spectral resolving power of $R = 225\,000$ (spectral resolving power of the ESPRESSO instrument).

Note that the input focal ratio for this investigation was $f/3.9$, although it is to be expected that the scrambling gain rises with faster focal ratio. In fact, Avila et al. (2006) found a difference in scrambling gain between the fibre coupled with $f/3$ and $f/11$ by a factor of two. Also, following the Avila & Singh (2008) investigations, the scrambling gain appears to be largely independent of the fibre core size, although a slight trend for lower scrambling gain towards larger fibre core sizes can be found ($G = 120, 110, 100, 75$ for core sizes 60, 100, 200, 600 μm , respectively).

7.1.3 Conclusions

The experimental investigations of the previous section imply that the barycentre shift due to incomplete scrambling (i.e. that the fibre retains some memory about its input illumination) is a problem independent of spectral modal noise. The scrambling gain for the fibre far-field (definition see section 7.1.1) is $G = 210 \pm 20$; at the same order as the value found by Avila ($G \approx 100$) for the fibre near-field. This value is slightly higher, a result that is consistent with the common observation that image scrambling improves when exchanging near-field with far-field (Bouchy & Connes, 1999).

For future spectrograph designs it would be beneficial to further explore the parameter dependence of scrambling gain, especially with regard to fibre-length. But barycentre position depending on wavelength has been repeatedly reported by collaborators (independent private communications, M. Woche and A. Reiners).

Using the apparatus as for the experimental determination of the barycentre shift, an important question to solve would in how far the scrambling gain improves when

agitating the fibre. As stated in section 6, the pattern in fig. 7.3 does not vanish when the agitator is switched on. Thus, the barycentre non-repeatability would be independent of agitation. This implies that the pattern only marginally contributes to the barycentre shift, a further indication that modal noise and incomplete scrambling are two different phenomena.

7.2 Ray-tracing simulation

Fig. 7.5 shows the result of ray-tracing simulations imaging the near-field of the fibre (simulation conducted using Mathcad, by Allington-Smith). With increasing input angle for a collimated beam, the intensity output exhibits an increasing number of concentric ring-like shapes around the fibre centre. The asymmetry that is displayed by these concentric rings causes the barycentre of this simulated intensity distribution to differ from its geometrical centre. Whether this approach can be applied needs some further experimental verification within a future work-package and is not pursued here.

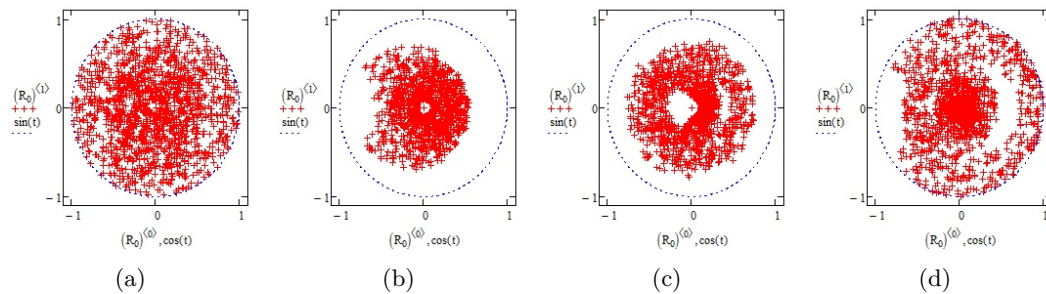


Figure 7.5: Ray tracing for different input angles. Depicted is the far-field of the fibre. 0 deg in the left, increasing angle towards the right (up to 5 deg), showing an increasing number of distinct concentric ring-shapes around the centre. *By Allington-Smith (paper forthcoming)*

The simulation merely produces the concentric ring-pattern for simulations of short fibre ends (a few tens of centimeters). However, as to date there is no fibre-length-dependence for scrambling reported to the author's knowledge and a significant effect due incomplete scrambling has already been reported for 2 m long fibres (Wilken et al., 2010).

7.3 Estimation of Photometric uncertainties

As can be seen from chapters 6 and 7, modal noise and incomplete scrambling can severely restrict the performance of the spectrograph in its photometric and in barycentre accuracy. It has been argued in the previous chapters that these effects are based on independent phenomena as modal noise occurs in coherent light (narrow band effect) whereas incomplete scrambling is an effect that affects the bary-centre of lines in a broad spectral range by the same amount (broad band effect).

It is established in the literature that the inhomogeneous intensity distribution due to modal noise causes photometric instability in conjunction with a truncating aperture (chapter 4). Likewise, an intensity variation due to incomplete scrambling will be induced as the coupling properties of the input light change. Just as modal noise only slightly affects the barycentre, the photometric uncertainty caused by incomplete scrambling is expected to be a second order effect.

This section is intended to outline a possible method to estimate the incomplete scrambling effect by using the data already presented in section 7.1.2.

7.3.1 Experimental investigation

The concept is similar as to the discussion earlier in chapter 6. In fact, the same data can be used to look for a possible spectrograph throughput variation when the input illumination changes.

The parameters are identical to those used in section 7.1.2:

- Fibre core size: 100 μm
- Spotsize on fibre core: $\approx 12 \mu\text{m}$
- Shift in fibre core: 70% of fibre core diameter
- A slit size of 200 μm is used at the slit plane.
- Input focal ratio was $f/3.9$

A raw image as in fig. 7.6 is obtained. The measurements are conducted three times to prove the repeatability of the effect.

The analysis steps are based upon the following assumptions:

1. The modal noise pattern is eliminated when all the spectral orders overlap (the HeNe-filter which is used for the modal noise investigations has been removed), a possible incomplete scrambling signal (independent of modal noise) will therefore manifest in the intensity distribution over the cross section of the spectrum independent of wavelength.

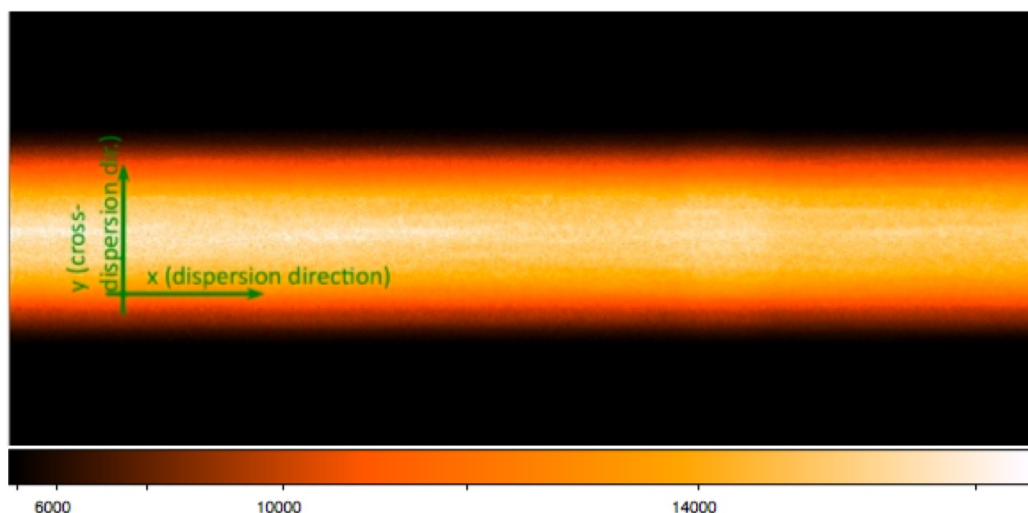


Figure 7.6: Exposure for scrambling tests, central illumination. Exposure time was 6 s. The grey scale is proportional to the square root of intensities in order to enhance the contrast, a modal pattern of low contrast becomes visible.

2. The intensity pattern that leads to the observed uncertainties is repeatable.

Cross-sections for different input illumination is illustrated in fig. 7.7. On first sight it is hardly discernible whether the repeated measurements reproduce the cross section pattern better than a measurement of different input illumination. A rough estimate can be obtained when measuring the maximum deviation between two measurements. This method yields an average deviation of 0.6% for the repeatability of the central illumination, the deviation for the vertical shift is 1.0% and for the horizontal shift 0.5%. This seems evidence that these patterns are non-repeatable. The barycentre calculation in section 7.1.2 evaluates the entire cross-section and is thus a better indicator. The analysis comprises the same set of data and as could be seen from the investigations, the barycentre property is repeatable when moving the input spot to the same position at the fibre end face as compared to the case where the input illumination is changed.

Fig. 7.6 shows an example spectrum where the fibre is illuminated in the centre. Due to the non-linear scale a pattern becomes visible which has been earlier described as ‘modal noise’ pattern (chapter 6). This can be explained when considering that of all the spectra overlapping (HeNe-filter removed), the one spectrum that has the highest efficiency of the blazed grating is dominant over the others and its modal noise pattern is prevalent, although strongly attenuated in contrast due to the random phase relations towards the other spectra. However, in order to derive the scrambling contribution to the photometric uncertainty, it is integrated over the entire width of the spectrum which further decreases any effect of the underlying

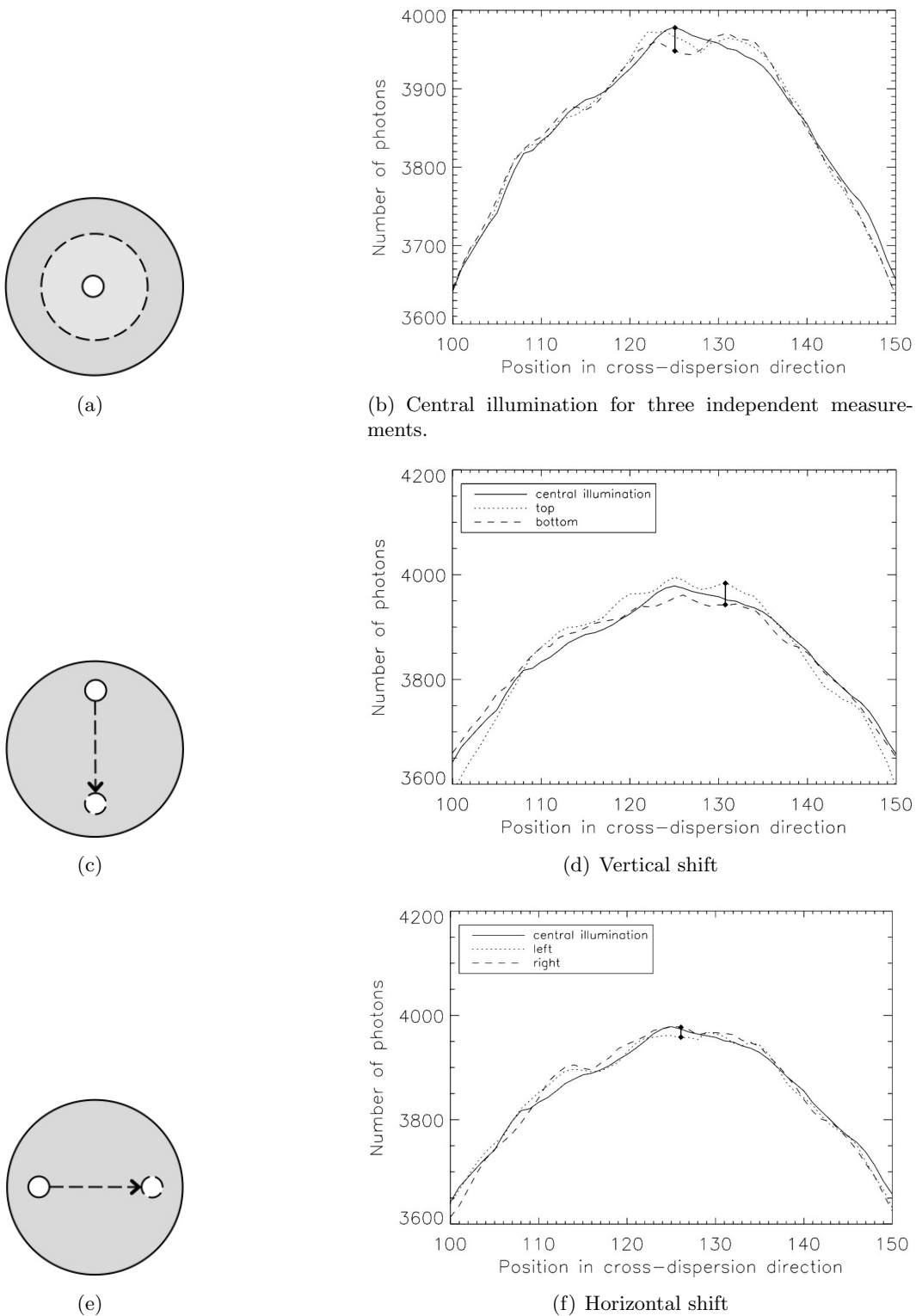


Figure 7.7: (a), (b) - Repeated measurement for central illumination; (c), (d) - Cross sections for different input illumination when shifting the input spot vertically; (e), (f) - Cross sections for shifting the input illumination horizontally.

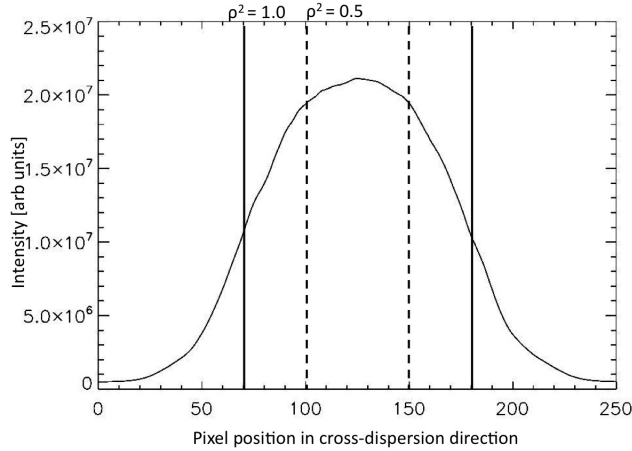


Figure 7.8: Cross-section of fig. 7.6, the solid line is chosen so that it defines the aperture of $\rho^2 = 1$ at the positions of the FWHM, the dashed line refers to $\rho^2 = 0.5$ respectively.

modal noise pattern.

The following analysis steps are proposed to derive the photometric uncertainty:

- Flat fielding with central illumination exposure
- Normalization.
- Measuring the throughput: Integrating over a certain range in y (see fig. 7.8) imitates the application of different sizes of a slit apertures truncating the beam in cross-dispersion direction.
- The ‘noise’ derives from the scattering of three independent throughput measurements from the same input illumination.
- The signal to noise is calculated from noise and mean signal of the exposure.

The first item is supposed to mimic the effect that flat fielding with calibration exposures has on real data. A subsequent weighting with an idealized cross section suppresses the photon noise at the edges of the spectrum. Normalization guarantees that the throughput variation is due to variation in the intensity distribution rather than due to a variation of the intensity of the halogen lamp. Care has to be taken to ensure that the background signal is not the main contribution to the signal variation – on the other hand, the normalization has to include the scattered light at the slopes of the spectrum as well.

In a next step, different slit sizes should be applied. Instead of considering the slit to truncate the beam in x , the beam will be ‘artificially truncated’ in y , the effects are assumed to be symmetric due to the fibre symmetry. The scattering between three independent measurements (from different input illumination) is used to establish

a ‘noise’- signal. This assumes that the position variation of the input illumination is for the real measurement actually an unknown, so that e.g. a guiding instability that causes a shift at the input leads to an intensity variation at the output. An error of the signal to noise can be derived from the scatter of the SNR of the three independent set of measurements.

7.3.2 Discussion

This section proposed a guideline to derive the photometric uncertainties from data already obtained and presented in section 7.1.2. Whether a potential effect of modal noise (cf. fig. 7.6) can be neglected compared to the combined photometric noise of modal-noise and incomplete-scrambling can be estimated taking the results of previous chapters into account. At least an upper limit for signal-to-noise due to incomplete scrambling can be obtained.

7.4 Barycentre repeatability due to modal noise

The previous chapters 4-6 discussed how the inhomogeneous intensity distribution to the speckle pattern at the fibre output give rise to photometric uncertainties and thus aggravating measurements that determine e.g. stellar parameters or star formation characteristics in galaxies (see section 2.3).

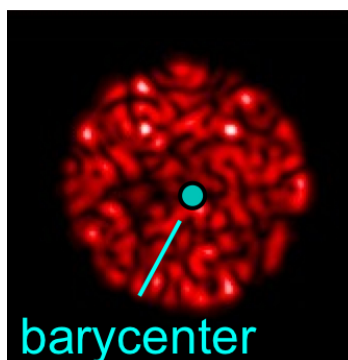


Figure 7.9: The inhomogeneous intensity distribution at the fibre exit (here: fibre endface near-field) causes the barycentre to be different from the geometrical centre. The barycentre is subject to changes with variation in the speckle pattern and thus lowers repeatability of subsequent, comparative measurements of spectral line centres (simulation based on 50 μm core diameter, 50 modes, 632.8 nm).

This chapter so far investigated the barycentre shift due to the inhomogeneous intensity distribution in the broadband. Like incomplete scrambling the asymmetry in

the speckle pattern also causes non-repeatability of the barycentre measurement as depicted in fig. 7.9. This effect has first been acknowledged by Wilken et al. (2010), affecting the determination of radial velocities (e.g. for exo-planet detection) as well as absolute line shift towards a calibrated reference line (e.g. for redshift determination).

This chapter outlines a strategy to obtain a barycentre shift from theoretical considerations. We start with the examinations already taken chapter 5, where it was shown that mode simulations at least to some degree conform with the theoretical predictions for modal noise. This estimation is likewise based on mode propagation simulation which is restricted to few modes only and thus at best will provide an upper limit for the barycentre shift.

7.4.1 Simulation of the barycentre shift

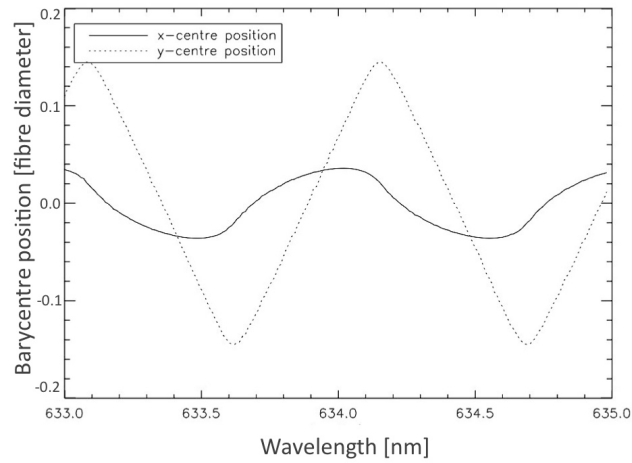
The aim of this section is to derive the barycentre shift from simulated speckle patterns. As earlier in section 5.2, the simulation assumes a symmetric coupling of angles at the input side, on-axis coupling, where the modes are first in phase and complete phase randomization between modes occurs due to the fibre imperfections. From the resulting intensity pattern the barycentre can be calculated.

Fig. 7.4.1 shows the simulated centre variation at the fibre near field for different mode numbers traveling through the fibre. Simulation of electromagnetic field distribution are based on a 50 μm fibre having a numerical aperture of 0.22. The diameter of the fibre core was 50 pixels, so that 1 pixel off centre refers to 1% of the fibre diameter. The length of the period for the two-mode case (fig. 7.10(a)) is determined by the length of the fibre (2here: 0 meters).

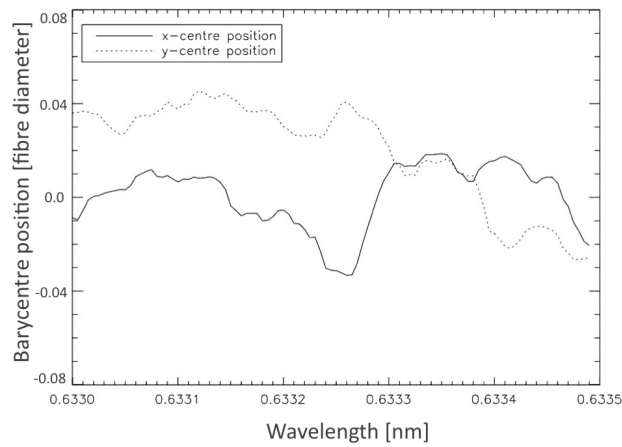
A basic assumption is that the barycentre measurement is a snap shot, i.e. when comparing to the real application the variation of the speckle pattern during the exposure is negligible. From fig. 7.10(a), the x-value of the barycentre oscillates with 4% around the central value, whereas the y-position uncertainty can get as high as 14% (equal to the combined uncertainty).

For seven modes (fig. 7.10(b)) the combined uncertainty goes already down to 4%. This is considerably lower as would be expected since more modes are averaging the asymmetry out.

Taking more and more modes into account to simulate the different speckle pattern, becomes laborious and meets the same problems as already discussed in section 5.2. Nevertheless, this can be taken as an upper limit estimate, assuming a visibility of roughly 2% as was deduced from experimental investigations in chapter 6, the centre variation would be 3×10^{-4} . The achievable radial velocity precision would thus be



(a) 2 modes



(b) f/16 (7 modes)

Figure 7.10: Barycentre shift vs. wavelength for different number of modes coupling into the fibre.

(see eq. (2.5))

$$\Delta v_r = \frac{1}{v} \frac{3 \times 10^{-4}}{R} c = 80 \text{ cm s}^{-1}, \quad (7.2)$$

comparable with the 30 cm s^{-1} result obtained by Wilken et al. He employed a fibre of core size $300 \mu\text{m}$, 514.9 nm central wavelength illumination. An optical image scrambling device was used, the fibre agitation device switched off. His result indicates that modal noise is not suppressed using additional image scramblers (apart from the fibre) and thus supports the hypothesis that modal noise and incomplete scrambling are two different phenomena.

7.4.2 Barycentre shift prediction

Earlier on, the photometric uncertainty caused by a speckle pattern was investigated. Taking this result, the likelihood to find a certain intensity for a given area in the fibre can be predicted. In the following this result is used as a tool to predict the barycentre variation of this pattern. A successful determination of the barycentre will lead to an analytical model that is capable of predicting the barycentre repeatability for a given mode number and visibility.

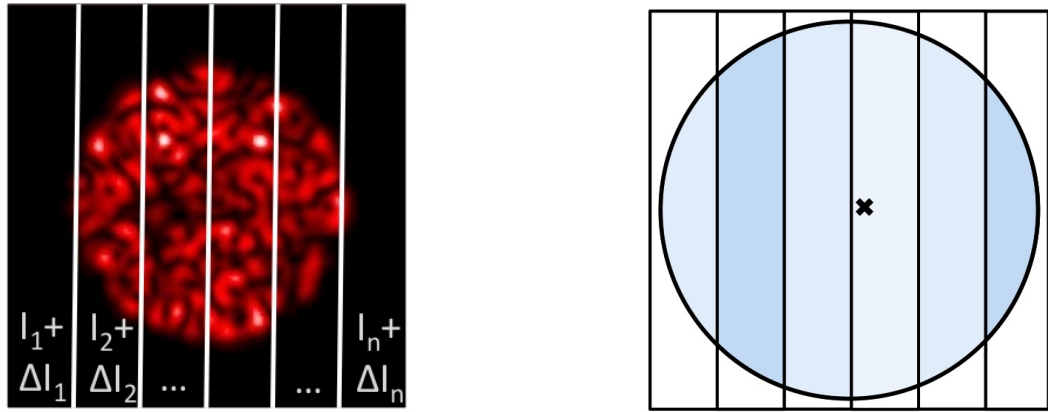
The idea is illustrated in fig. 7.9: The intensity distribution is divided into equal sections, taking into account the uncertainty in intensity in each section as well as each section's mean distance from the centre, the uncertainty of the barycentre Δx_i can be approximated:

$$\Delta x_i = \frac{1}{I_{tot}} \sum_i \Delta I_i x_i, \quad (7.3)$$

with I_{tot} the total intensity, Δ_i the deviation of intensity in section i from its average value, x_i the x position of section i .

This analysis was conducted using a imagined speckle pattern, dividing the fibre in fractions of decreasing size fig. 7.11(a). The variation of the intensity values was realized using a random value from a poisson distribution (fig. 7.12, $\sigma = 1/SNR_{mod}$).

The value for the barycentre converged to zero distance from the fibre geometrical centre. This result is not surprising but it proves the approach to be infeasible. A useful segmentation could be to use the size of an average speckle and divide the image using a honeycomb pattern as in fig. 7.13. Whether this approach gives reliable results needs then to be verified from a barycentre measurement of a real or a simulated speckle pattern.



(a) Each of these fields inhibits a likelihood to measure a certain intensity given by modal noise statistics.

(b) Field segmentation, simulated intensity distribution and barycentre.

Figure 7.11: Schematic representation to calculate an estimate for the barycentre shift: The intensity in each section is determined by modal noise theory (fig. 7.12). The resulting barycentre is calculated from each section's total intensity and the position of its geometrical centre.

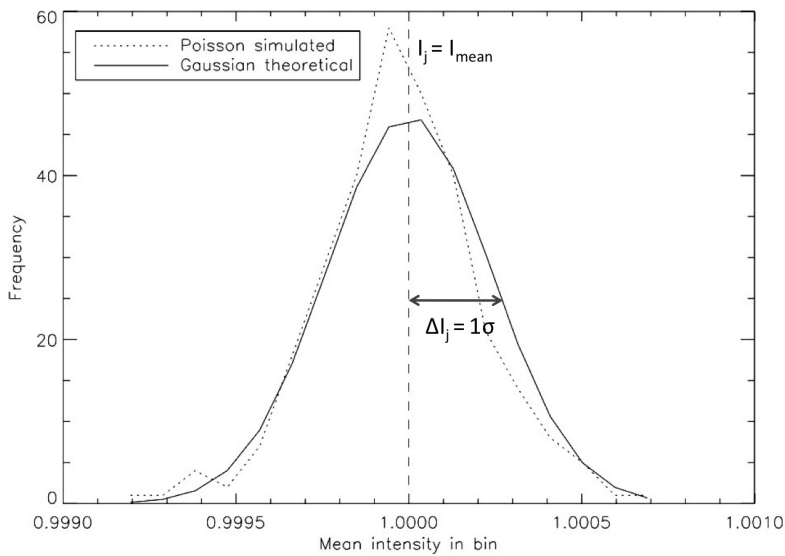


Figure 7.12: The dotted line corresponds to the occurrence of intensities for a division of a simulated speckle pattern as in fig. 7.11(a). Its Gaussian approximation (solid line) has the one sigma standard deviation as given by eq. 5.3. This distribution is used to fill the segments in fig. 7.11(b) with intensities.

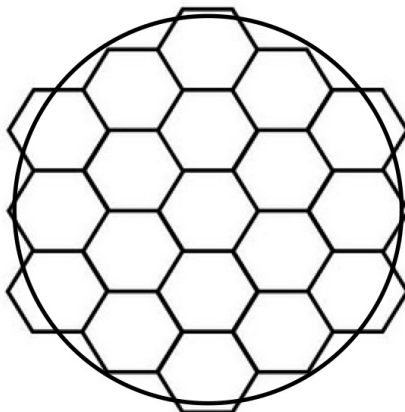


Figure 7.13: Alternative field division using hexagons of the size that corresponds to the average area that is covered by one speckle.

7.4.3 Conclusions

Two methods are presented to determine the barycentre shift due to modal noise. The first method is based on few-mode simulation and already provided an upper limit value for the barycentre shift. This treatment is similar to the mode simulation presented earlier in section 5.2.

This estimate for the barycentre effect shows that a signal degradation due to this effect can in most cases be neglected since incomplete image scrambling is dominating. If, however, the incomplete image scrambling is improved the modal noise contribution can become dominant.

Note that this simulation assumes an equal power distribution for all supported modes, possibly impeding its applicability. A more direct determination of the barycentre shift could be obtained when scrutinizing the raw data as used in chapter 6 to derive the photometric uncertainty due to modal noise. The barycentre in cross-dispersion direction is likely to give a good approximation to the relations in dispersion direction.

The second method is based on the intensity distribution due to the signal-to-noise ratio as described earlier in chapter 5. A refinement of the method potentially delivers an analytical tool for barycentre prediction. However, the validity of this approach needs verification by calculating the barycentre of a real or a simulated speckle pattern.

Chapter 8

Devices inducing measurement uncertainties and mitigation strategies

In section 8.1 some devices are listed that can introduce barycentre shift or photometric uncertainties due to modal noise or incomplete scrambling. The main property in common is that they cause modal or spatial filtering. In section 8.2 the impact of fibre image slicing on these effects is discussed. Section 8.3 then describes and compares a few strategies to ameliorate these effects.

8.1 Spatial and mode filtering processes

Grating and Apertures

Chapters 4-6 thoroughly discussed how a restricting aperture, such as a truncation of the beam at the fibre exit, can induce a variation of the throughput (in wavelength and time) thus affecting the photometric accuracy. As mentioned already by Grupp (2003), some spectrograph designs feature an overfilling of the grating, effectively acting as a restricting aperture leading to beam vignetting. This is usually done to save grating costs while still realizing high spectral resolving powers, thereby the trade-off that is being made is to lose a fraction of the light at the edges of the

incident beam.

Tapering

As a result the focal ratio of light propagating through the fibre decreases (étendue conservation) which is not completely gained back at the expansion of the fibre cross-section. This also causes the acceptance angle of the fibre to be diminished (otherwise higher order modes couple become radiation modes at the tapered fibre section).

Photonic lanterns

These special devices are designed to enable a single multi-mode to multiple single-mode fibre transition (and vice-versa). This is useful for two specific reasons:

1. It furnishes an array of single mode fibres which can be inscribed with fibre-Bragg gratings. These are used to deselect specific wavelengths (in particular sky background emission lines from the atmosphere) to significantly improve the measurement.
2. By re-arranging the small core-size fibres into a linear array, a large fibre circular geometry can be reformatted into a thin slit, for enhancing the spectrograph resolving power.

Work on photonic lanterns has been conducted by Thomson et al. (2011) and Noordegraaf et al. (2009). It has been argued that the number of single mode fibres after the multi-mode single-mode transition should match up with the number of modes guided in the multi-mode fibre. This is to guarantee that the losses for the transition would be minimal. However, losses are reported to be greater than 0.3 dB ($\lesssim 10\%$) by Noordegraaf et al.. Part of the losses could be due to the tapering, but also it is to be questioned whether the degrees of freedom of the random mode excitation can be sufficiently addressed by the strictness of the single-mode channels arrangement. These two aspects suggest that the mode filtering effect can be stronger than for the two devices mentioned previously.

8.2 Fibre image slicing

Fibre image slicing is used to increase the spectral resolving power of an instrument. Instead of using a beam truncating aperture, the image (or the far-field) of the fibre is sliced into thinner fractions and then re-arranged to form a pseudo-slit of smaller width than the original image (see fig. 8.1).

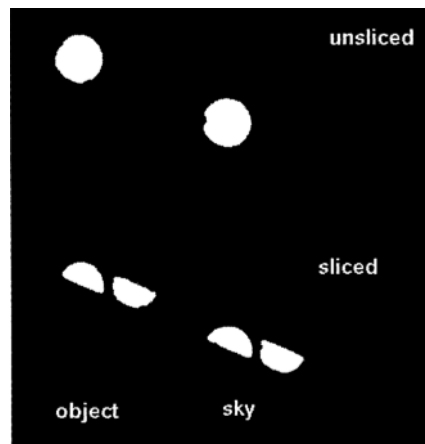


Figure 8.1: Fibre image after slicing by Kaufer (1998).

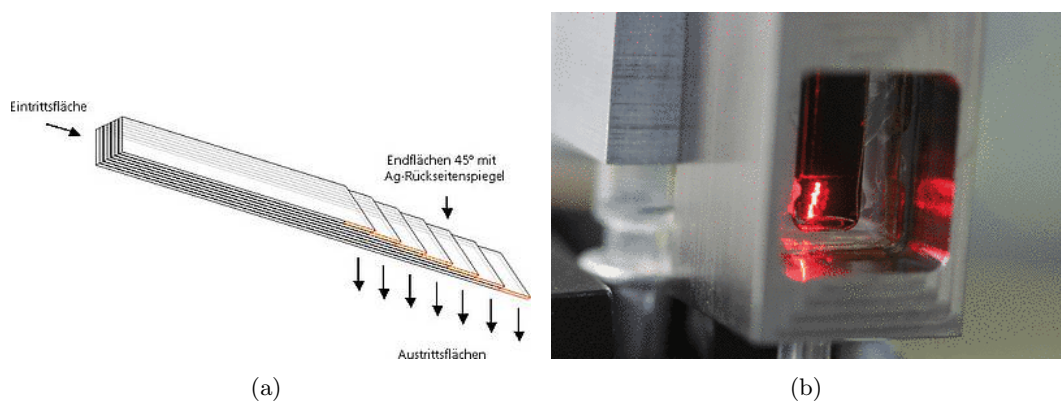


Figure 8.2: Image slicing device for the PEPSI-VLT instrument (source: <http://www.aip.de/pepsi/>).

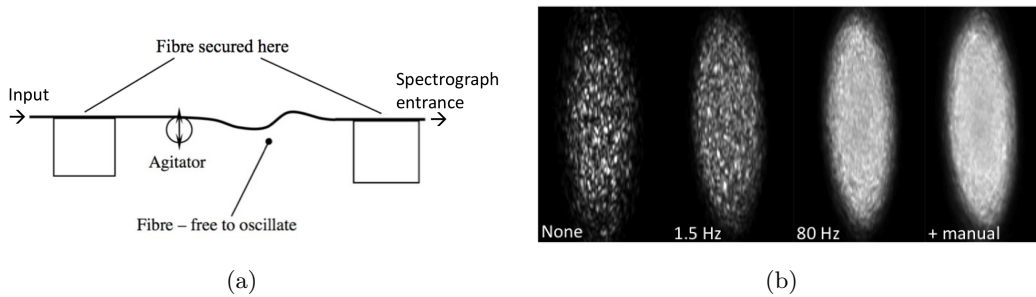


Figure 8.3: a) Fibre agitation device using a commercial loud-speaker, b) the resulting speckle pattern

This is mainly achieved by means of prisms or mirror devices (the PEPSI-VLT case is a typical example, see fig. 8.2).

An induction of photometric uncertainties is not expected, unless a significant amount of light is lost at the edges of each specular surface. In general, a beam slicing approach is beneficial as compared to the beam truncation approach. With regard to barycentre accuracy, the absolute repeatability of radial velocity measurement will be increased. Nevertheless, the enhancement does not inversely scale with the pseudo-slit width as is expected from theory.

Since slicing geometrically reduces the width of the spaxel in the spectral direction, it by necessity must increase the length of the spaxel in the cross-dispersion direction. Thus the slit length will accommodate fewer spatial elements than would be the case with a slit formed from unsliced fibre core images.

8.3 Mitigation strategies

8.3.1 Fibre agitation

The fibre agitation technique (fig. 8.3) has already been discussed in chapter 6 where spectra-images of the fibre subjected to this procedure were being used to obtain the required flat-field exposures. Fig. 8.4 illustrates again the improvements that can be achieved with the agitation device. For the unagitated fibre the SNR does not exceed ≈ 1000 even for long exposure times, whereas the agitated fibre shows SNR improved by a factor of seven. Even this value is still dominated by photon noise however, so the eventual limitation due to modal noise is expected to be significantly higher.

The fibre agitation device presented here in the thesis consisted of a commercially

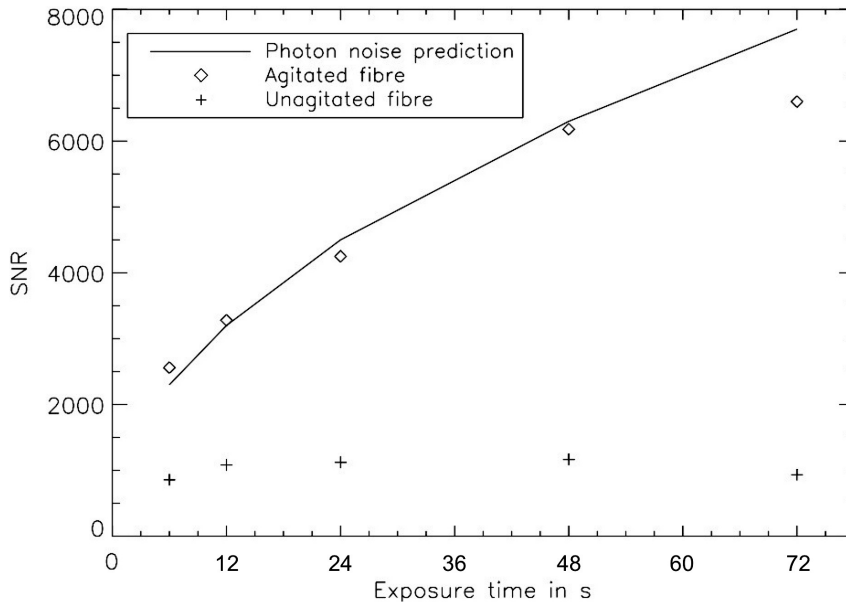


Figure 8.4: An agitating device can improve the signal quality by more than a factor of four (from SNR ≈ 1500 to ≈ 6000 in this particular example). The agitation device was a loudspeaker, figure same as fig. 6.16.

available loudspeaker and two fibre-clamps to fix the fibre at two points (fig. 8.3(a)). Other experimental schemes have been employed, devices as diverse as an electric toothbrush (Corbett, 2006) or a mobile phone (Avila & Singh, 2008). To the author there is no known report on this technique, so that further exploration of this area would be recommendable. For the HARPS instrument a dedicated device has been implemented, improving the signal beyond detection of the photon noise limit (Wilken et al., 2010).

It is believed that the method works because during agitation the fibre core experiences stress, thus inducing a change in refractive index and optical path length. The corresponding relative phase shift causes the speckle pattern to change during detector integration time. As a result, the speckle pattern becomes smoothed out and thus reducing modal noise (fig. 8.3(b)). However, following this argument, modal noise should be reduced for a) longer exposure times and b) higher amplitude and more frequent agitation – but of these expected effects only a slight dependence could be established. More importantly, there does not seem to be an ‘optimal’ agitation frequency or amplitude as long as these values exceed a certain threshold which could well be related to the loudspeaker device not functioning optimally at too extreme parameter regimes. Also a chaotic agitation should further reduce the modal noise signature, hence a study by Grupp et al. investigated the effect of a chaotic pendulum agitation (private communication), but no successful results have yet been published.

The technique improves both incomplete scrambling (G improved by up to a factor of eight, see Avila & Singh (2008)) and modal noise (Corbett, 2006 and this thesis). However, especially in multiplex instruments, agitation of many fibres individually becomes unfeasible. Techniques that can simultaneously address a set of fibres therefore need to be investigated (see sections 8.3.2 and 8.3.4).

8.3.2 Reversion prism

This device promises an improvement for both phenomena – incomplete scrambling and modal noise. Based on superposing two images, the reverted image and its original, the combined image will exhibit a high stability in barycentre. This prism device (see fig. 8.5) has been proposed by G. Murray (paper forthcoming) and currently under investigation at Durham University.

The mode of operation consists of moving the prism in and out of the beam path such that the throughput for the original beam (prism out) is identical to the throughput for the reverted image (prism in), requiring the prism to reside slightly longer in the beam path than out of the beam path. Moreover, the shutter in front of the detector has to be controlled in a way not to permit any light passing on to the detector during prism moving time.

Initial investigations showed the technique could in principle achieve sufficient repeatability of position and time period for the in- and out-states of the prism, but further experimental tests need to be conducted in order to prove the feasibility of the device (from: “Reversion Prism Justification”, technical report, Murray, 2012).

For an accuracy of 30 cm/s, a spectrograph operating at $R = 100\,000$ must be stable to 1 part in 10 000; which defines the repeatability of the prism motion. The absolute position does not matter unless the images are averaged by the detector. For optimal optical performance, light from the fibre needs to be expanded into a collimated beam of ~ 5 mm so the repeatability requirement is ~ 500 nm which is well within the capability of commercial motorised translation stages operating between hard stops. (Even without beam expansion the tolerance required, 10 nm, is still achievable.) Furthermore as noted above, the homogenised barycentre location accuracy can be improved by averaging shorter exposures – as determined by the timescale over which the position of the barycentre changes due to flexure and temperature variations. Thus, by using good translation stages, with ~ 10 nm repeatability, and with an appropriate observational strategy, we should be able to achieve an accuracy

of 1 cm/s.

One major concern is the potential polarizing characteristic of the prism device. Due to reflections within the prism the device might act as a partial polarizing filter. Each polarization state is occupied by a different set of modes. That means if one plane of polarization is attenuated stronger than the other, the resulting speckle pattern at the output of the prism is not the exact reverse of the input pattern. For the fraction of the speckle pattern with barycentre shift Δx that experiences stronger attenuation due the polarization p of the prism, the residual barycentre shift Δx_{sum} amounts to

$$\Delta x_{sum} = \Delta x - (1 - p)\Delta x = p\Delta x.$$

Together with the intensity of the polarization state that is not attenuated due to polarizing effects and thus exhibits perfect barycentre cancellation, the barycentre shift reduces to $p\Delta x/2$. It needs to be said that this Δx is the barycentre shift of the pattern that only contains half the modes and is thus larger than the original barycentre displacement.

Nevertheless, even with if there was a restricted performance to be revealed (tests on-going, fig. 8.6), this technique could prove highly advantageous for multiplex systems as it enables simultaneous addressing of an entire set of fibres. Future instrumentation programs such as FASOT could benefit from these results.

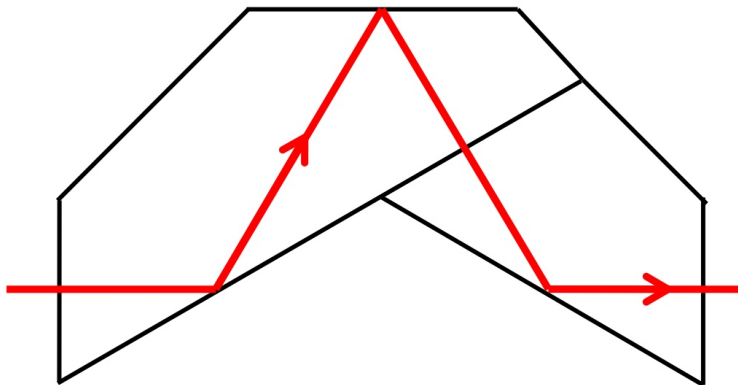


Figure 8.5: Light entering the prism at the left experiences reflection three times. The angular and spatial information is thus reverted. Moving the device in and out of the beam while recording an exposure ensures the barycentre is stable at the common geometrical centre of the original and reverted images.

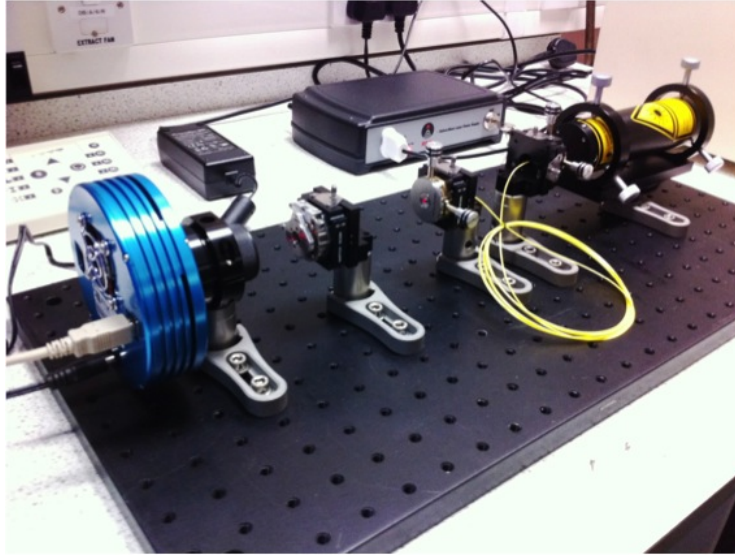


Figure 8.6: Experimental setup for reversion prism tests.

8.3.3 Optical scrambling

This technique, reported by Avila & Singh (2008) can be realised using a single lens (see fig. 8.7) or a double lens. The basic principle is to convert beam angle to spatial domain and vice-versa. This is done in a break between two fibres. The improvement that could be measured was from $G = 270$ to $G = 1100$ for a $60\ \mu\text{m}$ fibre at $f/4$ input focal ratio. The study also investigated mechanical scrambling, which proved largely unfeasible due to the high throughput losses.

A similar device, but with two lenses attached to the fibre end-faces (Barnes & MacQueen, 2010) was tested and showed better throughput performance of 75%, potentially improvable to 85%. The double optical scrambler was also implemented in Durham for use at the SALT HRS instrument (Bramall et al., 2010).

Since this technique does not increase the number of modes, according to eq. (5.3), the modal noise performance is not expected to improve.

8.3.4 Square and octagonal fibres

In a paper by Chazelas et al. (2010), scrambling tests for square and octagonal fibres are presented (see fig. 8.8). Although these novel cross-sections are promising candidates and show reasonable improvement for the near-field scrambling properties, the far-field properties display complicated patterns or these patterns are hidden by a strong FRD caused by the fibre. Note that the current research literature has focused on Ceramoptec experimental fibres only. Durham is in possession of a Mit-

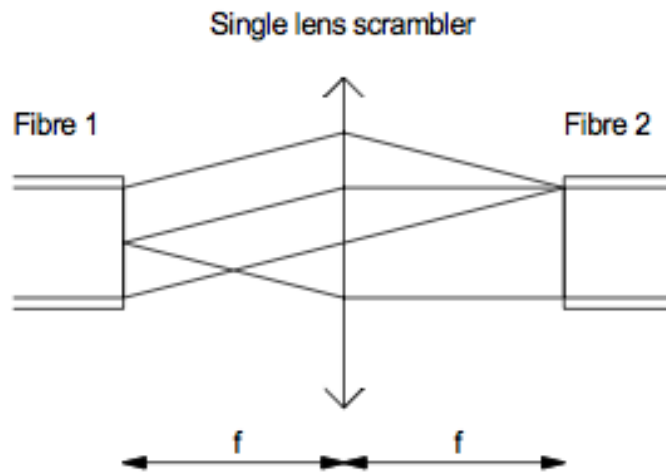


Figure 8.7: Optical scrambler by Avila & Singh (2008), one single lens is used in a 2f-configuration to improve the homogeneity of the fibre output.

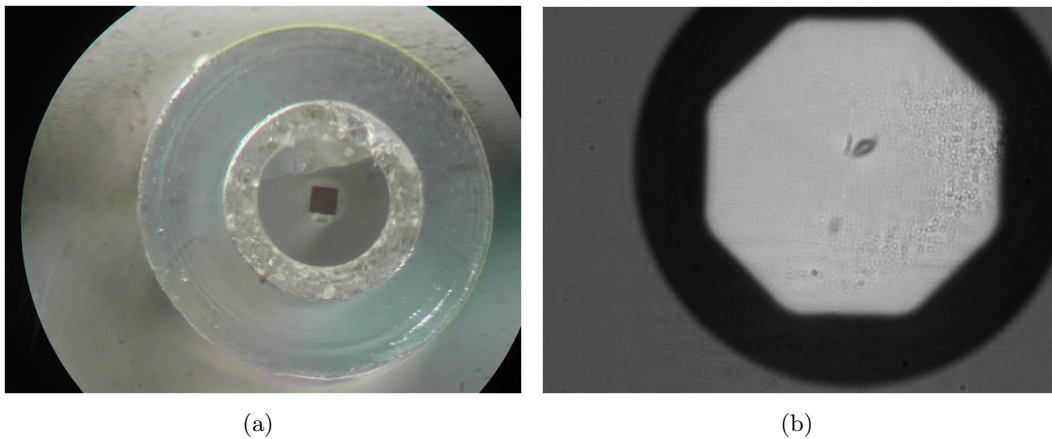


Figure 8.8: Fibre cross-section for a) square and b) octagonal fibre.

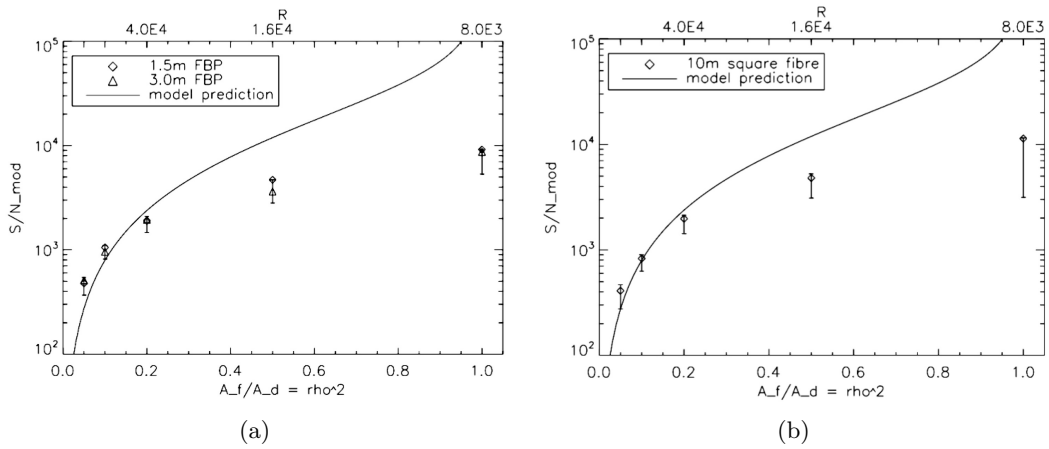


Figure 8.9: Modal noise for a) circular and b) square fibre.

subishi square core fibre, and early indications are that this may have significantly better FRD performance and a more regular far-field. Such results are perhaps not too surprising because the fibre is a commercially available product and as such, has been subject to more rigorous development and testing than the limited-production Ceramoptec product. However, tests on scrambling performance have not been conducted in this thesis. The results of modal noise tests are shown in fig. 8.9.

The results show that there is no significant improvement from the circular to the square fibre. This is not surprising, since the number of modes for a 100 μm square fibre is only little larger than the number of modes for a circular fibre with a core diameter of 100 μm (the number of modes scales with the area of the cross-section). If coupling into a square fibre, the signal would actually be degraded since the FRD is increased due to the coupling process and also due to the change in cross-section itself.

However, the scrambling properties as well as the far-field performance are currently subject to evaluation at Durham University and show promising preliminary results.

8.4 Conclusions

This chapter presents various devices that cause either photometric or barycentre uncertainties (section 8.1) as well as mitigation strategies (section 8.3). Apertures such as slits at the fibre entrance and overfilled grating can introduce modal noise. Tapering and technologies that encompass tapering would act as mode filters as well, although the expected effect is presumed to be insubstantial compared to a strong

beam truncation. The employment of fibre image slicer should have a beneficial effect upon absolute barycentre stability, although they are likely to stick behind their nominal performance of the then high resolution powers that could in theory be achieved with the spectrograph.

To reduce modal noise the fibre agitator is the most popular solution today. However, when it comes to a multiplex solution, techniques are required that are capable of addressing sets of multiple fibres at the same time. To deal with this problem, a new device, the reversion prism, will be more thoroughly tested. Finally, research into optical image scrambler and non-circular fibres are briefly summarized. These are devices particularly aimed at improving fibre image scrambling, however they do not improve modal noise performance.

Chapter 9

Concluding remarks

9.1 Introduction

The aim of this chapter is to emphasize the contribution of the work in this thesis to the current state of research regarding the fibre-induced uncertainties in spectroscopy. Therefore, a brief summary is given in section 9.2, its main results and original contributions are presented in section 9.3, leading to a proposal for a further course of investigation in section 9.4.

9.2 Summary

Optical fibres represent a key-enabling technology in current state-of-the-art astrophysical instrumentation. They display a number of properties that make them invaluable for high accuracy applications. Despite these merits, inherent properties of the fibres set a fundamental constraint to exactly these scientific goals in question. In order to facilitate the realisation of these projects, this thesis is therefore aimed at predicting these limitations by means of theoretical and experimental methods. Finally, a selection of mitigation strategies is proposed.

Part I of this thesis introduces the problem of measurement uncertainties in fibres, each chapter taking a different aspect under consideration.

Chapter 1 explains the role of fibres in astronomical instrumentation, outlining the central theme of this thesis: The optical fibre represents a key-technology to meet the

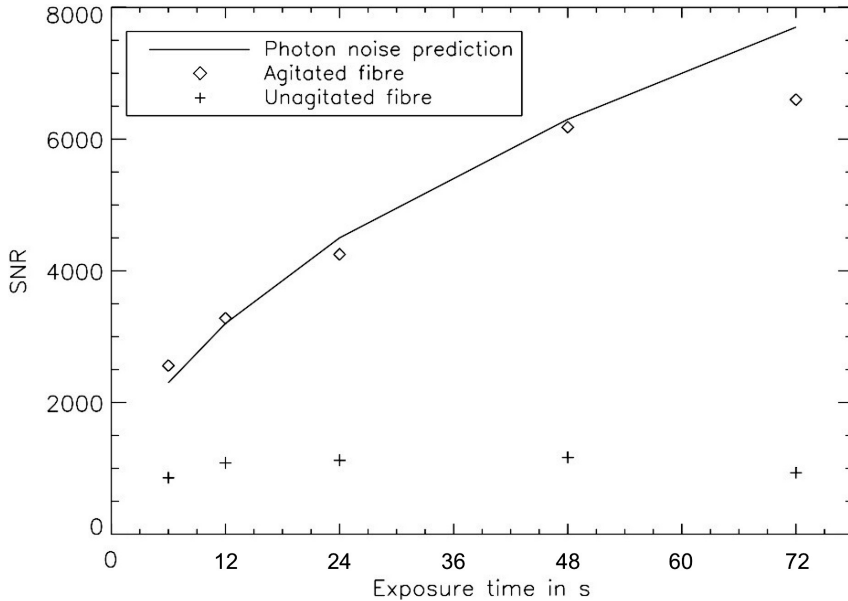


Figure 9.1: Signal-to-noise vs exposure time for the unagitated and agitated fibre, compared with the theoretical photon noise (same as fig. 6.16). This demonstrates the magnitude of signal degradation due to modal noise for high signal-to-noise ratios and the abatement using a fibre agitation device.

requirements, facilitating instrument stability and enabling high spectral resolving powers. Advancing to ever higher accuracies in spectral resolving power and photometric noise levels revealed two main problems that accompany the employment of fibres: *modal noise* and *incomplete scrambling*. These two phenomena each affect two crucial observables – the photometric accuracy and the barycentre stability.

In chapter 2 astronomical applications are presented motivating the drive for the high accuracy levels that are crucial for achieving the science goals. These two chief observables, of the fibre signature at the spectrograph are discussed.

Chapter 3 is concerned with the theoretical properties of the standard, circular step-index fibre and introduces notations, underlying mechanisms and theoretical assumptions that are used throughout this thesis. The impact of restricted photometric accuracy on polarimetry is also discussed.

Chapters 4 to 6 of this thesis focus on the uncertainties associated with modal noise, i.e. the properties that become apparent when operating the fibre in the coherent regime. Fig. 9.1 (see section 6.2.2) exemplifies the relevance of modal noise and mitigation strategies for astronomical applications.

Starting out with chapter 4 the current state of research is presented, with chapter 5 summarizing the findings and undertaking mode simulations in order to find a predictive model for modal noise in terms of the inhomogeneous intensity distribu-

tion at the fibre output. Due to some disagreement between theory and experiment it is concluded that further, more thorough experimental investigations are necessary with the focus on the parameter regime typical for astrophysical applications. The experimental setup, conduct of the experiment and the results are presented in chapter 6. Besides photometric accuracy, the repeatability of the barycentre measurement is affected by the inhomogeneous intensity distribution at the fibre output as well. In section 7.4 an estimation involving mode propagation simulation reveals that the effect on the barycentre measurement is probably negligible compared to the incomplete scrambling discussed in chapter 7.

Incomplete scrambling (chapter 7) is an inherent fibre property that occurs for incoherent light. It is caused by an inhomogeneous intensity pattern at the fibre output in response to an asymmetric input illumination. This causes the barycentre to shift and can also be the source of photometric uncertainties (dealt with in section 7.3). For applications of high signal levels the Fourier-transform-spectroscopy can give a stability advantage (Hunten, 1968 and Kostiuk et al., 1988), but at the expense of the advantages of spatial resolution attained by integral-field-spectroscopy and photon-collecting efficiency of multi-object-spectroscopy.

Chapter 8 puts forward mitigation strategies and mentions processes and new technologies that potentially trigger these unwanted measurement uncertainties.

This study has set out a predictive model to establish the measurement uncertainties occurring in fibre-coupled spectrographs for astronomical applications. Within the restricted coverage of a thesis, major advances towards this ambitious goal have been attained, which will be the object of section 9.3. These findings naturally stimulate a series of new questions. With outlook on current and future demands on instrument development, in section 9.4 a number of these questions are highlighted in order to motivate further research in these areas, listing further refinements and recommendations to obtain a clearer picture of uncertainties and related problems.

9.3 Original Contributions

As this thesis shows; both coherent and incoherent phenomena introduce uncertainties in the barycentre as well as photometry.

This finding is non-trivial since throughout the existing literature modal noise is used as a synonym for the photometric uncertainty associated to the coherent properties of the fibre, whereas it is referred to as ‘incomplete scrambling’ when considering

the non-repeatability of the barycentre measurement. The latter is predominantly caused by properties which become apparent already in the broad band of the fibre spectral response. This is first mentioned in an investigation by (Wilken et al., 2010, section 3.3) which suggests that although the barycentre measurement is mainly affected by incomplete scrambling, a smaller contribution can be ascribed to modal noise. An investigation of both *modal noise* (chapters 4 - 6) and *incomplete scrambling* (chapter 7) has provided a preliminary estimate of the magnitude of this effect and helps to understand the underlying mechanisms.

A detailed study on the photometric uncertainty as caused by the modal properties of the fibre was conducted (chapter 6). This began with a review of existing literature, leading to a mode simulation approach which shows some agreement with experimental findings. However, its validity and feasibility are to be questioned for a high number of modes. It has also been shown that many mechanisms which give rise to modal noise are not sufficiently well understood yet.

These findings motivated a more thorough experimental investigation, thereby focussing on the parameter regime that has not been addressed in the literature but is more typical for astronomy, i.e. low beam truncation and low visibilities ($< 10\%$). The results confirm that an analytical expression factorizes into a *visibility* and a *speckle statistics term*, where the latter can be understood by applying the theorem found by Goodman & Rawson (1981) which is valid for the perfectly coherent case. The problem of predicting the photometric uncertainties caused by fibre modal noise thus reduces at the one hand to the problem of determining the number of excited modes. On the other hand, the visibility of the speckle pattern needs to be determined as it occurs at the detector plane. A semi-analytical model describing visibility as a function of input focal ratio and slit-width (restricting the beam at the spectrograph input) was established, paving the way for further experimental and analytical investigations. Contrary to expectations this analysis does not show a visibility dependence on the spectrograph resolving power. The number of excited modes is lower than suggested by eq. (3.25), a method to deduce this value experimentally is described in section 6.3.2.

In section 2.4 these experimental investigations have revealed a potential deficiency in a recent instrument project (FASOT), where the science requirements for the polarimetric accuracy demand high signal-to-noise levels. Currently available grating sizes are insufficient, implying that the modal properties require a trade-off between spectral resolving power and polarimetric accuracy to be taken into account.

Motivated by the rapid advancements in exo-planet research, Avila & Singh (2008) investigated the near-field scrambling properties of fibres as applied to high-resolution spectroscopy. The investigations extend this to the far-field case, revealing that the image scrambling improvement due to the (untreated) optical fibre is of the same order of magnitude.

Finally, existing mitigation strategies are presented, together with a new idea; the ‘reversion prism’ which ought to improve the barycentre instability for both effects incomplete scrambling and modal noise. A critical assessment of potential problems of future fibre technology (especially astrophotonics) in conjunction with modal noise is expounded.

9.4 Outlook and future work

The results of this study have shown that it is crucial to understand modal noise, and in particular incomplete scrambling, for the design of state-of-the-art high resolution spectrographs. Fibre-technology represents the most feasible and stable solution as compared to alternative technologies. It thus proves to be an invaluable approach and its limitations can be reduced with a series of mitigation strategies.

The major objective of this thesis was to find a predictive model in order to quantify the uncertainties related to modal noise and incomplete scrambling in standard optical fibres, thus enabling trade-offs to be made that take these effects into account or modifications of the instrument during design phase e.g. to allow for additional space to place components that help reduce these uncertainties. This objective has been partly achieved, with a series of questions left open which are to be discussed in the following section, emphasizing what is believed are the most fruitful aspects given the current direction of astrophysical research.

9.4.1 On-going instrument projects

Multi-object spectrographs in planning such as OPTIMOS-EVE or BigBOSS will operate at predominantly low spectral resolving powers. Although the dependence on resolving power is not sufficiently understood yet, at least the theoretical model predicts a low speckle contrast. Furthermore the expected photon rates are low for the key science projects, so that these instruments are thus unlikely to suffer significantly from fibre modal noise or incomplete scrambling effects.

The Fibre Arrayed Solar Optical Telescope (FASOT), will encounter a large signal to noise ratio at high spectral resolving powers and is thus likely to be limited by modal noise. Furthermore, PEPSI and similar instruments on 8 m-class telescopes that also need to provide high SNR data for bright objects (e.g. massive stars and their chemical composition) are likely to experience signal degradation due to modal noise. For more details and references see chapter 2.

Probably the most striking examples for cutting-edge research which encounter the full severity of these uncertainties concern instruments dedicated to exoplanet research. These spectrographs are using the Doppler radial velocity method for exoplanet detection and are thus limited in accuracy by the non-repeatability of the barycentre measurement. Among these are high-resolution systems like HARPS and ESPRESSO which will enable the detection of Earth-like planets. The evidence from this study suggests that these instruments will be limited by incomplete scrambling, but at the level of accuracy that these instruments are aimed at, a barycentre contribution from modal noise is posing a limiting factor as well.

For the current research activities that appear to predominantly focus on radial velocities or line position, the barycentre stability due to incomplete scrambling as well as modal noise is most important. On the other hand, continuous improvement on systems that concentrate on the detection of the profile and strength of spectral lines is required to study planetary atmospheres (e.g. Fossati et al., 2011). Careful planning of mitigation strategies is necessary to achieve the high photometric accuracies in question. Although a handful of successful mitigation strategies have been found, tested and even proven to deliver substantially improved science data, the majority of these devices are unfeasible for multi-fibre spectrographs due to the enhanced costs and shortage of space in these usually very compact systems. There is, therefore, a definite need for truly original devices that enable application to a multi-channel instrument.

9.4.2 Study on photometric uncertainties

In order to study the photometric uncertainty related to modal noise, an experimental setup was built, exploring the spectrograph response at high focal ratio input, low visibility and weak beam truncation – a parameter regime that is assumed to be the most relevant for astronomical applications but was found to be insufficiently addressed in the existing literature.

The empirical findings of this investigation have confirmed the factorization of modal noise into a coherent and a visibility term. The coherent term seems sufficiently understood by applying speckle statistic laws (Goodman & Rawson, 1981). A value for the visibility can be obtained, e.g. by directly evaluating the speckle pattern at the spectrograph output. From the product of the visibility and the coherent term, the limiting signal-to-noise ratio can then be calculated.

Despite this initial success, a number of caveats need to be noted regarding the present study. Firstly, due to experimental limitations, the high spectral resolving powers and very high signal-to-noise regimes could not be explored effectively. In order to confirm the model prediction for these regimes, a larger grating and a more stable setup are required. Furthermore, this study stresses the importance of the visibility contributing to the photometric uncertainty, but the current theoretical model is not sufficient to describe the observed functional dependence. Most notably, experimental data suggests the visibility to be independent of the spectrograph resolving power and the fibre length, contrary to the theoretical model.

At present a semi-analytical model can be presented at best. The visibility could be described in terms of input focal ratio and slit-width, but these results potentially lose their validity in a different parameter regime. Experimental findings also suggest a mechanism independent of fibre-length, it is therefore recommended to understand these phenomena first before a more complex analytical model is attempted.

A brief outline is given in how far incomplete scrambling can cause photometric uncertainties. Using a similar approach as with the modal noise investigations, the spectrograph setup can be used to measure relative throughput variations by simulating the application of different apertures (described in section 7.3).

9.4.3 Study on incomplete scrambling

The recent developments in astronomical instrumentation focussing on exo-planet research suggest that a strong emphasis lies on the phenomena related to the uncertainty of the barycentre determination. The repeatability of a barycentre measurement is first of all restricted by incomplete scrambling. An experimental test showed that the far-field image scrambling properties of fibres are comparable to the effects observed in the near field. Here, a more thorough study on the response to different input parameters would be desirable, e.g. investigating the scrambling effect for different values of incident angle and off-set from the optical axis. In addition, an in-depth study of the mechanisms, using e.g. ray-propagation to simulate the intensity distribution, could deliver a more secure handling and more profound

understanding of the mechanisms at work.

Today's high-precision spectrographs are already capable of resolving an additional effect to the barycentre shift due to the modal noise contribution, emphasizing the necessity for a valid model for barycentre prediction. Taking the earlier result into account, namely that modal noise is a phenomenon characterized through its factorization into a visibility and a coherent term; it is possible to infer that in an analogous manner the knowledge of visibility solves half the problem. It then remains to be understood how the coherent factor of barycentre variation behaves as a function of the number of excited modes. This again stresses the importance to explore the functional dependence of the visibility term.

9.4.4 Mitigation strategies and further considerations

The current study mainly concentrated on the quantification of measurement uncertainties and only briefly considers mitigation strategies to overcome these effects. It would however be a great advancement for future planning of instruments to establish figures that quantify these improvements. Furthermore, in light of multi-fibre systems, a feasible strategy seems to be a technology like the reversion prism or a fused square fibre output, but these technologies need further experimental exploration in the laboratory as well as on-sky demonstration before claiming these to provide a reliable solution for these instruments.

Finally, an overview and assessment of potentially signal degrading devices is given, covering current devices such as image slicers as well as future and recent, yet unexplored techniques (e.g. fibre-Bragg-gratings) mainly related to the astrophotonic research endeavors. These rather specialised devices have only a limited range of application and are therefore not pursued in detail here. This investigation only intends to highlight potential sources of problems and recommends a more thorough study when required.

References

- Allington-Smith J., 2006, *New Astronomy Review*, 50, p. 244
- Allington-Smith J., Murray G., Content R., Dodsworth G., Davies R., Miller B. W., Jorgensen I., Hook I., Crampton D., Murowinski R., 2002, *The Publications of the Astronomical Society of the Pacific*, 114, p. 892
- Amendola L., Tsujikawa S., 2010, *Dark Energy: Theory and Observations by Luca Amendola and Shinji Tsujikawa*. Cambridge University Press, ISBN: 9780521516006
- Anderson J. P., Habergham S. M., James P. A., 2011, *MNRAS*, 416, p. 567
- Auvergne M., Bodin P., Boissard L., Buey J.-T., Chaintreuil S., Epstein 2009, *Astronomy and Astrophysics*, 506, p. 411
- Avila G., Singh P., 2008, Society of Photo-Optical Instrumentation Engineers (SPIE) Conference Series, 7018, *Optical fiber scrambling and light pipes for high accuracy radial velocities measurements*
- Avila G., Singh P., Albertsen M., 2006 Vol. 6269 of Society of Photo-Optical Instrumentation Engineers (SPIE) Conference Series, *Photometrical scrambling gain and focal ratio degradation in fibers for astronomical instruments*
- Barbosa F. K. B., Storchi-Bergmann T., Cid Fernandes R., Winge C., Schmitt H., 2006, *MNRAS*, 371, p. 170
- Bailes M., Lyne A. G., Shemar S. L., 1991, *Nature*, 352, p. 311
- Barnes S. I., MacQueen P. J., 2010 Vol. 7735 of Society of Photo-Optical Instrumentation Engineers (SPIE) Conference Series, *A high-efficiency fibre double-scrambler prototype*
- Basri G., Borucki W. J., Koch D., 2005, *New Astronomy Reviews*, 49, p. 478

- Baudrand J., Walker G. A. H., 2001, *PASP*, 113, p. 851
- Bekki K., Tsujimoto T., 2011, *MNRAS*, 416, p. L60
- Bevington P. R., 1969, *Data reduction and error analysis for the physical sciences*
New York: McGraw-Hill
- Boisse I., Bouchy F., Chazelas B., Perruchot S., Pepe F., Lovis C., Hebrard G., 2010,
Consequences of spectrograph illumination for the accuracy of radial-velocimetry,
ArXiv e-prints, 2010arXiv1001.0794B
- Bouchy F., Connes P., 1999, *Astronomy and Astrophysics Supplement*, 136, 193
- Bozkurt Z., 2011, *New Astronomy*, 16, p. 412
- Bramall D. G., Sharples R., Tyas L., Schmoll J., Clark P., Luke P., Looker N., Dipper
N. A., Ryan S., Buckley D. A. H., Brink J., Barnes S. I., 2010 Vol. 7735 of Society
of Photo-Optical Instrumentation Engineers (SPIE) Conference Series, *The SALT
HRS spectrograph: final design, instrument capabilities, and operational modes*
- Buck J. A., 1995, *Fundamentals of Optical Fibers*. John Wiley & Sons, Inc
- Carrasco E., Parry I. R., 1994, *MNRAS*, 271, p. 1
- Chazelas B., Pepe F., Wildi F., Bouchy F., Perruchot S., Avila G., 2010 Vol. 7739
of Society of Photo-Optical Instrumentation Engineers (SPIE) Conference Series,
New scramblers for precision radial velocity: square and octagonal fibers
- Chen C.-H., Reynolds R. O., Kost A., 2006, *Applied Optics*, 45, p. 519
- Christie H., Viti S., Williams D. A., Girart J. M., Morata O., 2011, *MNRAS*, 416,
p. 288
- Clampin M., 2011 Vol. 8146 of Society of Photo-Optical Instrumentation Engineers
(SPIE) Conference Series, *Overview of the James Webb Space Telescope observa-
tory*
- Corbett J., Butterley T., Allington-Smith J. R., 2007, *MNRAS*, 378, p. 482
- Corbett J. C. W., 2006, PhD-Thesis, Durham University
- Cristiani S., Avila G., Bonifacio P., Bouchy F., Carswell B., D'Odorico S., D'Odorico
V., Delabre B., 2007, *Nuovo Cimento B Serie*, 122, p. 1165
- Daino B., de Marchis G., Piazzolla S., 1979, *Electronics Letters*, 15, p. 755
- Daino B., de Marchis G., Piazzolla S., 1980, *Journal of Modern Optics*, 27, p. 1151

-
- Dekel A., Silk J., 1986, *Astrophysical Journal*, 303, p. 39
- Epworth R. E., 1979, *Tech. Dig. Top. Mtg. on Opt. Fiber Commun.*, p. 1–106
- Evans C., Morris S., Swinbank M., Cuby J.-G., Lehnert M., Puech M., 2010, *Astronomy and Geophysics*, 51, p. 020000
- Eversberg T., Moffat A. F. J., Debruyne M., Rice J. B., Piskunov N., Bastien P., Wehlau W. H., Chesneau O., 1998, *PASP*, 110, p. 1356
- Faifer F. R., Forte J. C., Norris M. A., Bridges T., Forbes D. A., Zepf S. E., Beasley M., Gebhardt K., Hanes D. A., Sharples R. M., 2011, *MNRAS*, 416, p. 155
- Flagey N., Boulanger F., Noriega-Crespo A., Paladini R., Montmerle T., Carey S. J., Gagné M., Shenoy S., 2011, *A & A*, 531, p. A51
- Fossati L., Ryabchikova T., Shulyak D. V., Haswell C. A., Elmasli A., Pandey C. P., Barnes T. G., Zwintz K., 2011, *MNRAS*, 417, 495
- Fuhrmann K., Pfeiffer M., Frank C., Reetz J., Gehren T., 1997, *Astronomy and Astrophysics*, 323, p. 909
- Gazzano J.-C., de Laverny P., Deleuil M., Recio-Blanco A., Bouchy F., Moutou C., Bijaoui A., Ordenovic C., Gandolfi D., Loeillet B., 2010, *Astronomy and Astrophysics*, 523, A91
- Giannini T., Nisini B., Neufeld D., Yuan Y., Antonucci S., Gusdorf A., 2011, *Astroph. J.*, 738, p. 80
- Gloge D., 1971, *Applied Optics*, 10, p. 2252
- Gonzalez G., 2011, *MNRAS*, 416, p. L80
- Goodman J. W., Rawson E. G., 1981, *Optics Letters*, 6, p. 324
- Grupp F., 2003, *A& A*, 412, p. 897
- Heacox W. D., 1988, in S. C. Barden ed., *Fiber Optics in Astronomy Vol. 3 of Astronomical Society of the Pacific Conference Series, Wavelength-precise slit spectroscopy with optical fiber image scramblers.* p. 204–235
- Hill J. M., Angel J. R. P., Scott J. S., Lindley D., Hintzen P., 1980, *Astrophysical Journal*, 242, L69
- Hill K. O., Tremblay Y., Kawasaki B. S., 1980, *Optics Letters*, 5, p. 270
- Hjelme D. R., Mickelson A. R., 1983, *Applied Optics*, 22, p. 3874

-
- Horne K., 2000, in American Astronomical Society Meeting Abstracts Vol. 33 of Bulletin of the American Astronomical Society, *Simulations of Exo-Planet Transit Searches*. p 128.04
- Hubble E., 1929, Proceedings of the National Academy of Science, 15, p. 168
- Hunten D. M., 1968, Science, 162, 313
- Kanada T., Aoyama K., 1983, Optics Letters, 8, p. 339
- Kaufer A., 1998, in S. Arribas, E. Mediavilla, & F. Watson ed., Fiber Optics in Astronomy III Vol. 152 of Astronomical Society of the Pacific Conference Series, *A Two-Beam Two-Slice Image Slicer for Fiber-Linked Spectrographs*. p. 337
- Keller C. U., Snik F., 2009, in S. V. Berdyugina, K. N. Nagendra, & R. Ramelli ed., Solar Polarization 5: In Honor of Jan Stenflo Vol. 405 of Astronomical Society of the Pacific Conference Series, *Polarimetry from the Ground Up*. p 371
- Kostiuk T., Deming D., Mumma M., 1988, Technical report, Advanced infrared astronomy
- Krabbe A. C., Pastoriza M. G., Winge C., Rodrigues I., Dors O. L., Ferreira D. L., 2011, MNRAS, 416, p. 38
- Leibundgut B., Contardo G., Woudt P., Spyromilio J., 1999, in H. V. Klapdor-Kleingrothaus & L. Baudis ed., Dark matter in Astrophysics and Particle Physics *The high-redshift supernova search-evidence for a positive cosmological constant*. pp 222–+
- Liske J., Grazian A., Vanzella E., Dessauges M., Viel M., Pasquini 2008, MNRAS, 386, p. 1192
- Mayor M., Pepe F., Queloz D., Bouchy F., Rupprecht G., Lo Curto G., Avila G., Benz W., 2003, The Messenger, 114, p. 20
- Mengel S., Eisenhauer F., Tecza M., Thatte N. A., Roehrl C., Bickert K., Schreiber J., 2000 Vol. 4005 of Society of Photo-Optical Instrumentation Engineers (SPIE) Conference Series, *New era of spectroscopy: SINFONI NIR integral field spectroscopy at the diffraction limit of an 8-m telescope*. pp 301–309
- Moslehi B., Goodman J. W., Rawson E. G., 1983, Appl. Opt., 22, p. 995
- Murray G., 2011
- NIST, 2011, *NIST Atomic Spectra Database - Lines Holdings*, http://physics.nist.gov/cgi-bin/ASD/lines_pt.pl
-

-
- Noordegraaf D., Skovgaard P. M., Nielsen M. D., Bland-Hawthorn J., 2009, *Optics Express*, 17, p. 1988
- Papen G. C., Murphy G. M., 1999, *J. Lightwave Technol.*, 17, p. 817
- Perlmutter S., Aldering G., della Valle M., Deustua S., Ellis R. S., Fabbro S., Fruchter A., Goldhaber G., Groom D. E., Hook I. M., Kim A. G., Kim M. Y., Knop R. A., Lidman C., McMahon R. G., Nugent P., Pain R., Panagia N., Pennypacker C. R., Ruiz-Lapuente P., Schaefer B., Walton N., 1998, *Nature*, 391, 51
- Perryman et al., 2005, *Report by the ESA-ESO Working Group on Extra-Solar Planets*, ArXiv Astrophysics e-prints
- Piatti A. E., 2011, *MNRAS*, 416, p. L89
- Poppett C. L., Allington-Smith J. R., 2010, *MNRAS*, 404, p. 1349
- Qu Z. Q., 2011, in J. R. Kuhn, D. M. Harrington, H. Lin, S. V. Berdyugina, J. Trujillo-Bueno, S. L. Keil, & T. Rimmele ed., *Astronomical Society of the Pacific Conference Series Vol. 437 of Astronomical Society of the Pacific Conference Series, A Fiber Arrayed Solar Optical Telescope (FASOT)*. p 423
- Rafikov R. R., 2011, *MNRAS*, 416, p. L55
- Ramsey L. W., 1988, in S. C. Barden ed., *Fiber Optics in Astronomy Vol. 3 of Astronomical Society of the Pacific Conference Series, Focal ratio degradation in optical fibers of astronomical interest*. p. 26–39
- Rawson R. E., Goodman J. W., Norton R. E., 1980, *J. Opt. Soc. Am.*, 70, p. 968
- Rice J. A., 1997, *Mathematical statistics and data analysis, 2nd Edt.* Duxbury Press
- Riess A. G., Filippenko A. V., Challis P., Clocchiatti A., Diercks A., Garnavich P. M., Gilliland R. L., Hogan C. J., Jha S., Kirshner R. P., Leibundgut B., Phillips M. M., Reiss D., Schmidt B. P., Schommer R. A., Smith R. C., Spyromilio J., Stubbs C., Suntzeff N. B., Tonry J., 1998, *Astronomical Journal*, 116, 1009
- Saijonmaa J., Halme S. J., 1981, *Applied Optics*, 20, p. 4302
- Schlegel D., Abdalla F., Abraham T., Ahn C., Allende Prieto C., Annis J., 2011, *The BigBOSS Experiment*, ArXiv e-prints
- Schmidt B. P., Suntzeff N. B., Phillips M. M., Schommer R. A., Clocchiatti A., Kirshner R. P., Garnavich P., Challis P., Leibundgut B., Spyromilio J., Riess

- A. G., Filippenko A. V., Hamuy M., Smith R. C., Hogan C., Stubbs C., Diercks A., Reiss D., Gilliland R., Tonry J., Maza J., Dressler A., Walsh J., Ciardullo R., 1998, *Astrophysical Journal*, 507, 46
- Schuler S. C., Cunha K., Smith V. V., Ghezzi L., King J. R., Deliyannis C. P., Boesgaard A. M., 2011, *Astroph. J. Letters*, 737, p. L32
- Simcoe R. A., 2011, *Astroph. J.*, 738, p. 159
- Snyder A. W., Love J. D., 1983, *Optical Waveguide Theory*. Chapman and Hall Ltd.
- Spanò P., Tosh I., Chemla F., 2010 Vol. 7735 of Society of Photo-Optical Instrumentation Engineers (SPIE) Conference Series, *OPTIMOS-EVE optical design of a very efficient, high-multiplex, large spectral coverage, fiber-fed spectrograph at EELT*
- Thomson R., Birks T., Leon-Saval S., Kar A., Bland-Hawthorn J., 2011, *Optics Express*, 19, p. 5698
- von Paris P., Cabrera J., Godolt M., Grenfell J. L., Hedelt P., Rauer H., Schreier F., Stracke B., 2011, *Spectroscopic characterization of the atmospheres of potentially habitable planets: GL 581 d as a model case study*, ArXiv e-prints
- Weźgowiec M., Vollmer B., Ehle M., Dettmar R.-J., Bomans D. J., Chyży K. T., Urbanik M., Soida M., 2011, *A & A*, 531, p. A44
- Wilken T., Lovis C., Manescau A., Steinmetz T., Pasquini L., Lo Curto G., Hänsch T. W., Holzwarth R., Udem T., 2010, *MNRAS*, p. 55
- Wolszczan A., Frail D. A., 1992, *Nature*, 355, p. 145
- Wood T. H., 1984, *Optics Letters*, 9, p. 102